TOPICS IN GENERAL RELATIVITY THEORY: GRAVITATIONAL-WAVE MEASUREMENTS OF BLACK-HOLE PARAMETERS; GRAVITATIONAL COLLAPSE OF A CYLINDRICAL BODY; AND CLASSICAL-PARTICLE EVOLUTION IN THE PRESENCE OF CLOSED, TIMELIKE CURVES.

Thesis by

Fernando Echeverría

In Partial Fulfillment of the Requirements

for the Degree of

Doctor of Philosophy

California Institute of Technology

Pasadena, California

1993

(Defended August 3, 1992)

Thesis Advisor:

Professor Kip S. Thorne

To my wife and daughter

Acknowledgments

I would like to express my deep gratitude to my advisor, Professor Kip S. Thorne, who welcomed me into his research group and guided and encouraged me throughout my stay at Caltech, as well as during my absence. He is not only a remarkable and bright scientist, but also an excellent teacher and guide, as well as a great human being.

I would also like to thank the two people who accompanied me along this journey and who suffered gladly the necessary sacrifices: my wife Marcela and my daughter Barbara. I love you.

Abstract

In this thesis I present three separate studies on three different topics in General Relativity.

The first study investigates the accuracy with which the mass and angular momentum of a black hole can be determined by measurements of gravitational waves from the hole, using a laser-interferometer gravitational-wave detector. The black hole is assumed to have been strongly perturbed, perhaps by coalescence with a binary companion, and the detector measures the waves produced by its resulting vibration and ring-down. The uncertainties in the measured mass and angular momentum arise from the unavoidable presence of noise in the detector. It is found that the faster the hole rotates, the more accurate the measurements will be, with the uncertainty in the angular momentum decreasing rapidly with increasing rotation speed. It is also found that the errors in the mass and angular momentum are highly correlated.

The second study is an analysis of the gravitational collapse of an infinitely long, cylindrical dust shell. This analysis is expected to be helpful in understanding the behavior during collapse of more realistic, finite-length bodies. It is found that the collapse evolves into a naked singularity in finite time, as measured by a distant observer or by one riding on the shell. Analytical expressions for the variables describing the collapse are found at late times, near the singularity. The picture is completed with a numerical simulation that follows the collapse from the start until very close to the singularity. The singularity is found to be strong, in the sense that an observer riding on the shell will be infinitely stretched in the direction parallel to the symmetry axis, and infinitely compressed in the azimuthal direction. The gravitational waves emitted from the collapse are also analyzed.

The last study focuses on a different kind of phenomenon, namely, the consequences of the existence of closed timelike curves in a spacetime that contains a wormhole. One might expect that the closed timelike curves would cause difficulty for the initial value problem for systems that evolve in such a spacetime: a

system with apparently well-posed initial conditions might have no self-consistent solutions to its evolution equations. We study the simple case of a macroscopic, classical particle with a hard-sphere potential (a "billiard ball"), and we focus attention on initial conditions for which the evolution, if followed naively, is self-inconsistent: the ball enters one mouth of the wormhole and then comes out of the other mouth at an earlier time, then collides with its younger self, preventing itself from ever entering the first mouth . We find, surprisingly, that for all such "dangerous" initial conditions, there are an infinite number of self-consistent evolutionary solutions, involving a glancing collision and any number of wormhole traversals. We also find that for many non-dangerous initial conditions, there also exist an infinity of possible evolutions.

Contents

Chapter 1

Introduction

When Einstein formulated his theory of General Relativity and found that it predicted the existence of gravitational waves, he also found that for any astrophysical situation the waves would be so extraordinarily weak that it seemed unlikely they would ever be detected, much less be of observational importance. However, the advance of technology and the remarkable ingenuity of experimental physicists have created a series of gravity-wave detectors of increasing sensitivity, which make the detection of such waves likely in the next decade.

Weber [1] pioneered the field with the first resonant-bar detectors. These detectors have a very narrow band of high sensitivity, being tuned for a specific frequency. More recently, laser-interferometer-based detectors have been developed. They have the advantage of having a relatively wide frequency band of sensitivity, which makes them more useful as observational instruments [2]. The sensitivity of these interferometric detectors has been continually improving, and large-scale detectors of this type, those of the LIGO and VIRGO projects, are expected to reach the sensitivity range necessary for detection of waves produced by astrophysical sources.

In order to make optimal use of the LIGO/VIRGO measurements, it is important to understand the waveforms produced by the various possible sources. Much work had been done previously on determining waveforms [2, 3], but the prospects for actual detection have motivated many other more detailed analyses and calculations, for a wider class of astronomical sources.

Once we are reasonably confident of the relationship between an astrophysical phenomenon and the gravitational waves it emits, it becomes possible to estimate how well a LIGO-type detector will be able to determine the parameters involved in the phenomenon, and how its precision will depend on the actual values of the parameters.

In Chapter 2 of this thesis I present a study of this type. In it, I focus on the expected waveform emitted by a black hole after it has been strongly perturbed, e.g., by coalescence with a binary companion. That waveform is known to be a

superposition of so-called quasi-normal modes.

These modes are damped sinusoids whose frequencies and damping times have been accurately computed and depend solely on the black hole's mass M and angular momentum $J \equiv M^2 a$. Since we know this dependence, a precise observation of such a waveform would allow us to determine both the mass and the angular momentum of the black hole.

Any such measurement of M and J will be plagued by the detectors' noise. The purpose of Chapter 2 of this thesis is to determine, for the planned LIGO/VIRGO detectors, the errors introduced into the measured values M and J by the noise, and the correlation of those errors. In this analysis I have assumed (with some justification) that the waveform will be dominated by a single quasi-normal mode: the quadrupolar mode that is least strongly damped. I then evaluated the expected errors and correlations introduced by the detectors' noise into the measured values of the mode's frequency and damping time, and from those I inferred the errors and correlation of M and J.

Qualitatively, my results predict that the faster the black hole rotates, the more precise the measured values of M and J will be. I also found that for slowly rotating holes the mass is better determined than the angular momentum, but as the rotation gets faster, the uncertainty in the angular momentum decreases more rapidly, becoming better determined than the mass beyond a rotation parameter of $a \approx 0.8$. (The fastest that any hole can rotate is $a = 1$.) I also found that for all rotational speeds, the errors in M and J are very highly correlated.

Recently Finn [4] has argued that one should use a different method from mine to compute the values of a signal's parameters, and at first Finn's choice of method appeared to give different results from mine. (My method is based on the Wiener optimal filter, with the overall amplitude of the wave factored out of the analysis; Finn advocates a variant of the well-known maximum-likelihood method.)

In an addendum to the published paper that forms the main body of Chapter 2, I analyze Finn's maximum-likelihood method and prove that for my problem,

it is mathematically precisely equivalent to the Wiener method that I used, and it produces identical results.

One of the methods currently being pursued to obtain a better understanding of the waveforms emitted by strongly gravitating objects is numerical simulations on computers. The high nonlinearity of Einstein's equations makes it impossible to obtain even approximate analytical solutions in almost any situation that is not highly symmetric and highly idealized. On the other hand, the exact numerical solution of a realistic problem is enormously complicated and resource-intensive, computationally. Nevertheless, numerical simulations have been advancing rapidly in recent years, especially because of advances in computer technology, thereby making it possible to attack previously unsolvable problems.

Axially symmetric (2+1-dimensional) numerical simulations have been applied, in recent years, to the study of the gravitational collapse of bodies with shapes different from the analytically tractable, spherical case; see, e.g., [6, 7]. By these simulations it is possible to study not only the gravitational waves that are emitted, but also the way the collapse itself evolves, whether and under what conditions an event horizon forms, and whether the collapse evolves toward a singularity or is halted eventually by the physical properties of the collapsing matter, such as pressure and angular momentum.

Although these 2+1-dimensional numerical simulations are advancing very rapidly (and 3+1-dimensional simulations are now being initiated), they still are far from giving a complete understanding of the above issues in gravitational collapse. In the quest for deeper understanding, there is a need for studies of simpler physical models that can give insight to guide the 2+1- and 3+1-dimensional simulations.

In Chapter 3, I present a study of this kind, in which the gravitational collapse of an infinitely long, cylindrical shell of pressureless matter is analyzed. It has long been known that such a collapse produces a naked singularity [5], but nobody has previously studied the nature of the singularity or the evolution into it or the gravitational waves emitted by the collapse. My model is simple enough that

analytical solutions are obtained for the late stages of the collapse, and then a 1+1-dimensional numerical simulation completes the picture of the evolution from the initial state to the final singularity.

My analysis gives information about the way the collapse evolves and the time required for the complete evolution and how the collapse time depends on the cylinder's mass per unit length. I also confirm the prediction that the collapse produces a naked singularity, which is one of the issues of greatest interest in the 2+1-dimensional simulations of prolate collapse: Will naked singularities also be formed for finite-length, elongated bodies; and if so, what will be their character? Recent results [6, 7] suggest that naked singularities *will* form in the finite-length case when the body is made of dust and has vanishing rotation, and that the singularities extend along the symmetry axis from the body's interior into its vacuum exterior — and most intriguingly, that the singularity in the vacuum exterior *might* causally precede that in the interior or be spacelike with respect to it. This last property, if true, would suggest that the vacuum part of the naked singularity might still occur if the body's dust is given a tiny amount of pressure and rotation. These issues of the existence and nature of the singularity in the vacuum exterior of a finite-length, highly elongated body cannot be probed by my analysis of an idealized, infinite dust cylinder. However, my analysis may give useful insight into the central, matter-endowed region of the finite-length body, the nature of the singularity to be expected in the central region, and the burst of gravitational waves to be expected.

My analysis of the infinite dust cylinder shows that the singularity formed by the collapse is strong, in the sense that an observer riding on the dust shell as it collapses will become infinitely stretched parallel to the symmetry axis, and infinitely compressed azimuthally.

Finally, I have computed the shape of the gravitational waves emitted during the collapse. I found that the gravitational-wave strain rises continuously from zero to a maximum near the moment at which the unknown effects that are due

to the singularity formation dominate. The waves' stretch and squeeze are in the opposite direction to those of the singularity: The waves would stretch a detector along the azimuthal direction and squeeze it parallel to the symmetry axis.

The theory of General Relativity is enormously rich; in addition to the extraordinary solutions represented by black holes and spacetime singularities, it permits solutions that pose a series of questions about causality. Such is the case of classical, Lorentzian wormholes [9], which are solutions that connect separate regions of spacetime through a short throat.

It has been shown [10, 11] that according to *classical* general relativity theory, if traversable wormholes can exist, then generically they will produce closed, timelike curves, e.g., by one wormhole mouth moving relative to the other and thereby creating a "time difference" between them. (By a time difference is meant the property that if one travels through the wormhole, one emerges from the second mouth at a time that is different from one's entry into the first mouth, as measured in any relevant, external reference frame.) Once such a time difference has grown large enough to give rise to closed, timelike curves, the evolution of any system that encounters those curves will depend not only on events in the system's past, but also on some events in its future. This would, in principle, allow the type of science-fiction, time-travel paradoxes in which an observer travels into the past and prevents himself from entering the wormhole (perhaps by killing his younger self). Such paradoxes, of course, would mean that the initial-value problem might not be well posed, since there would seem to be no self-consistent solutions to the system's evolutionary equations.

Several researchers have studied this problem in recent years [12, 13], and surprisingly, we have all found that at least within the realm of classical physics, for every system that has been analyzed, there are always self-consistent solutions in the presence of closed, timelike curves. (Of course, the systems that have been analyzed are all very simple.)

Chapter 4 of this thesis presents the results of one of these studies, which I

have carried out in collaboration with Kip Thorne and Gunnar Klinkhammer. [1] In this study we examine the case of a simple and well-defined system, that of a "billiard ball" (a macroscopic body with a hard-sphere potential) that moves and self-collides in a spacetime that is flat except for a wormhole. The wormhole's two spherical mouths are connected by an infinitesimally long throat, and are at rest relative to each other and have a fixed time difference.

It is easy to conceive of an initial "dangerous" trajectory for the ball, in which it enters one mouth and comes out from the other mouth earlier, only to knock its younger self off its original trajectory, thereby preventing its younger self from entering the wormhole in the first place. This is an evolutionary problem with well-posed initial conditions, which at first sign seems to have no self-consistent, evolutionary solutions.

In our investigation we find that dangerous initial data of this sort are peculiar, not because they give rise to *no* self-consistent, evolutionary solutions, but rather because they actually give rise to an infinity of solutions. Each of the self-consistent solutions involves glancing collisions that only slightly deflect the ball's trajectory, and the solution can involve any number of wormhole traversals. Not only do the dangerous initial conditions give rise to an infinite number of evolutionary solutions; so do a wide variety of nondangerous initial conditions.

Research by others [14] shows that when one quantizes the billiard ball via a sum-over-histories technique and then takes the semiclassical (WKB) limit, the evolution becomes well behaved in a probabilistic sense: There is a definite and computable quantum-mechanical probability for the billiard ball to follow each of the classically allowed evolutionary solutions (trajectories), and the joint probability to follow two such solutions in the same experiment is zero. This is pleasing. Not so pleasing is the fact that the resulting quantum-mechanical evolution is

[1] My own contributions to this study were the following: the key ideas underlying the structure of the self-consistent solutions, as spelled out in Sec. II.B; the demonstration, in Appendix B, that in general there are two classes of small-deflection solutions (depicted in Fig. 3); and the demonstration that all dangerous initial trajectories have at least one or two self-consistent solutions (Sec. IV and Appendix B).

typically nonunitary. [15]

Although the laws of physics seem to accommodate themselves to closed, timelike curves moderately easily (aside from the issue of nonunitarity, which seems not to be deadly), it now seems somewhat likely, though not certain, that diverging vacuum fluctuations of quantum fields will prevent closed, timelike curves from ever forming. [16]

Bibliography

[1] J. Weber, Phys. Rev. **117**, 307 (1960).

[2] K. S. Thorne *Gravitational Radiation: A New Window onto the Universe* (Cambridge Univ. Press, Cambridge, in press).

[3] *Sources of Gravitational Radiation*, edited by L. Smarr (Cambridge Univ. Press, Cambridge, 1979).

[4] L. S. Finn, paper in preparation (1992).

[5] K. S. Thorne in *Magic Without Magic: John Archibald Wheeler*, edited by J. Klauder (Freeman, San Francisco, 1972).

[6] S. L. Shapiro and S. A. Teukolsky, Phys. Rev. Lett. **66**(8), 994 (1991).

[7] S. L. Shapiro and S. A. Teukolsky, Phys. Rev. D **45**(6), 2006 (1992).

[8] T. A. Apostolatos and K. S. Thorne, Phys. Rev. D (submitted).

[9] M. S. Morris and K. S. Thorne, Am. J. Phys. **56**, 395 (1988).

[10] M. S. Morris, K. S. Thorne, and U. Yurtsever, Phys. Rev. Lett. **61**, 1446 (1988).

[11] V. P. Frolov and I. D. Novikov, Phys. Rev. D **42**, 1057 (1990).

[12] J. Friedman, M. S. Morris, I. D. Novikov, F. Echeverria, G. Klinkhammer, K. S. Thorne, and U. Yurtsever, Phys. Rev. D **42**, 1915 (1990).

[13] F. Echeverria, G. Klinkhammer, and K. S. Thorne, Phys. Rev. D **44**, 1077 (1991).

[14] G. Klinkhammer and K. S. Thorne, Phys. Rev. D, in preparation.

[15] D. Politzer, Phys. Rev. D (submitted).

[16] S. W. Hawking, Phys. Rev. D (in press); S.-W. Kim and K. S. Thorne, Phys. Rev. D, **43**, 3929 (1991); V. P. Frolov, Phys. Rev. D **43**, 3878 (1991).

Chapter 2

Gravitational-wave measurements of the mass and angular momentum of a black hole

(Originally appeared in Phys. Rev. D **40**(10), 3194 (1989).)

PHYSICAL REVIEW D VOLUME 40, NUMBER 10 15 NOVEMBER 1989

Gravitational-wave measurements of the mass and angular momentum of a black hole

Fernando Echeverria
Theoretical Astrophysics, California Institute of Technology, Pasadena, California 91125
(Received 27 December 1988)

A deformed black hole produced in a cataclysmic astrophysical event should undergo damped vibrations which emit gravitational radiation. By fitting the observed gravitational waveform $h(t)$ to the waveform predicted for black-hole vibrations, it should be possible to deduce the hole's mass M and dimensionless rotation parameter $a=(c/G)(\text{angular momentum})/M^2$. This paper estimates the accuracy with which M and a can be determined by optimal signal processing of data from laser-interferometer gravitational-wave detectors. It is assumed that the detector noise has a white spectrum and has been made Gaussian by cross correlation of detectors at different sites. Assuming, also, that only the most slowly damped mode (which has spheroidal harmonic indices $l=m=2$) is significantly excited—as probably will be the case for a hole formed by the coalescence of a neutron-star binary or a black-hole binary—it is found that the one-sigma uncertainties in M and a are $\Delta M/M\simeq 2.2\rho^{-1}(1-a)^{0.45}$, $\Delta a\simeq 5.9\rho^{-1}(1-a)^{1.06}$, where $\rho\simeq h_s(\pi f S_h)^{-1/2}(1-a)^{-0.22}$. Here ρ is the amplitude signal-to-noise ratio at the output of the optimal filter, h_s is the wave's amplitude at the beginning of the vibrations, f is the wave's frequency (the angular frequency ω divided by 2π), and S_h is the frequency-independent spectral density of the detectors' noise. These formulas for ΔM and Δa are valid only for $\rho\gtrsim 10$. Corrections to these approximate formulas are given in Table II.

I. INTRODUCTION AND SUMMARY

In 1971 Press showed[1] that black holes can vibrate, and in fact have normal modes of vibration; and in 1974 Teukolsky and Press[2] showed that the gravitational waves emitted by a black hole will always be dominated, after an initial transient period, by a superposition of the outputs of a set of discrete normal (or quasinormal) modes. Since then the vibration frequencies ω of the normal modes and their radiation-reaction-induced damping times τ have been computed as functions of the hole's mass M and dimensionless rotation parameter $a=(c/G)(\text{angular momentum})/M^2$ by Chandrasekhar and Detweiler,[3] Detweiler,[4] Leaver,[5] and others.

In 1977, when Detweiler's[4] calculations revealed that for the most slowly damped mode of a rotating hole the waves' parameters $\{\omega,\tau\}$ are a unique and invertible function of the hole's parameters $\{M,a\}$, the possibility arose of being able to infer a hole's M and a from the waves it emits. This possibility is enhanced whenever, among all the hole's modes, the most slowly damped one is preferentially excited. Detweiler[6] has argued that this will be the case if the hole is rapidly rotating (if a is very near unity). Moreover, it will likely be the case for the most interesting and strongest emitting of all black-hole events: the formation of a deformed hole by the coalescence of a neutron-star binary or a black-hole binary. The reason is that during the coalescence the binary will have a rotating shape corresponding to spheroidal harmonic indices $l=m=2$, and the most slowly damped mode has precisely these indices.[4,5]

Although the idea of determining a hole's M and a from measurements of its gravitational waves has been around since 1977, nobody has yet estimated the accuracy with which this can be done, i.e., the rms errors ΔM and Δa due to the noise in the detectors to be expected in such a determination. This paper is devoted to an estimate of ΔM and Δa and their correlation.

Our estimate will rely on a number of assumptions.

(i) Which normal modes are present in the ringdown waves and in what mixture? Motivated by the above discussion, we shall restrict attention to the case where only the most slowly damped (fundamental), $l=m=2$ mode is present.

(ii) What is the transient waveform that precedes the ringdown? This transient, for a coalescing compact binary system, should consist initially of periodic waves whose frequency increases due to the spiraling orbital motion that brings the two bodies together, and then a burst due to the start of the coalescence itself. We suspect, but have not tried to prove, that ΔM and Δa will be rather insensitive to that transient, provided we express them in terms of the signal-to-noise ratio ρ for the ringdown waves and leave the initial transient out of ρ. Furthermore, the signal-to-noise ratio for the transient waveform may be small in comparison with that of the ringdown: in some model simulations this is true,[7] and for rapidly rotating holes (a near unity) the high Q factor of the ringdown enhances its signal-to-noise ratio. We shall presume for simplicity that there is no transient; and, more specifically, that the waves' waveform is

$$h_{jk}^{\mathrm{TT}}(t)=\begin{cases} e_{jk}\,A e^{-(t-t_s)/\tau_s}\sin\omega_s(t-t_s) & \text{for } t\geq t_s\ , \\ 0 & \text{for } t<t_s\ . \end{cases} \tag{1.1}$$

Here e_{jk} is the polarization tensor, A is the amplitude, ω_s and τ_s are the normal-mode frequency and damping time, and t_s is the waves' arrival time. (The subscript s, stand-

ing for "signal," is used to distinguish this ω_s, τ_s, and t_s from the values ω_0, τ_0, t_0 that are estimated by the experimenters and the values ω_k, τ_k, t_k that the experimenters use in their optimal filters; see Sec. II below.)

(iii) What is the spectral density $S_h(f)$ of the noise in the detector? [For a detailed discussion of $S_h(f)$ see Ref. 8.] The most promising of all gravitational-wave detectors are the multikilometer laser-interferometer detectors (also called "interferometric detectors" or "beam detectors") that are being planned in the United States, Britain, Germany, France, Italy, Japan, and Russia; for a review see Ref. 8. These are broadband detectors; and in the frequency ranges of optimal sensitivity their noise is likely to be white, $S_h(f)$ independent of f. Accordingly, we shall assume white noise. Since black-hole waves have, for the mode we have chosen, a quality factor [4,5]

$$Q_s \equiv \tfrac{1}{2}\omega_s \tau_s \simeq 2(1-a)^{-0.45} \gtrsim 2 , \tag{1.2}$$

the band of frequencies involved in the signal (1.1) is relatively narrow, $\Delta f < f$. This narrowness means that our results should not be very sensitive to the white-noise assumption. *Note*: the signal $h(t)$ which is to be compared with $S_h(f)$ is the projection of h_{jk}^{TT} on the unit vectors l_j and m_k which point along the beam detector's legs,

$$h(t) = \begin{cases} h_s e^{-(t-t_s)/\tau_s} \sin\omega_s(t-t_s) & \text{for } t \geq t_s , \\ 0 \quad \text{for } t < t_s , \end{cases}$$
$$h_s \equiv A e_{jk}(l^j l^k - m^j m^k) ; \tag{1.3}$$

see Ref. 8.

(iv) What are the statistical properties of the detector noise? Individual detectors exhibit some excitations due to local, non-Gaussian noise—e.g., due to sudden strain releases in the wires suspending the detector's mirrors or to inadequately shielded voltage fluctuations in the electric power lines. In order to have any likelihood at all of successful detection of waves it is essential to remove such excitations from the detectors' output data. Fortunately, the non-Gaussian noise comes in short spikes, separated by long intervals of purely Gaussian noise. Those short spikes are uncorrelated between two widely separated detectors and thus are easily removed by cross correlation. Thus we shall assume, in accord with the experimenters' past experience, that the remaining noise is Gaussian.

(v) What method is used to analyze the data? Wiener optimal filtering: more specifically, we shall assume that the data are run through a set of filters, each of which is optimized for detecting a signal of the form (1.3) but with values of the frequency ω_k, damping time τ_k, and arrival time t_k which differ from those of the signal. (The experimenters, of course, do not know in advance what ω_s, τ_s, and t_s are.) The experimenters choose as their best estimates of ω_s, τ_s, and t_s those filter values ω_k, τ_k and t_k which give the output with the largest signal-to-noise ratio. We shall denote these best estimates by ω_0, τ_0, and t_0.

In a large number of different measurements with identical input signals, but with Gaussianly fluctuating noise, this procedure will give different values of ω_0, τ_0, and t_0. These values will be Gaussianly distributed with means ω_s, τ_s, and t_s, if the signal-to-noise ratio is high enough. Correspondingly, the values M_0 and a_0 of the hole's mass and angular-momentum parameter inferred from ω_0 and τ_0 will be Gaussianly distributed, with means M and a, respectively. The bottom-line result of this paper is the Gaussian probability distribution (integrated over start times) for the inferred M_0 and a_0:

$$P(M_0,a_0) = \frac{Ma}{2\pi\Delta M\Delta a(1-C_{Ma}^2)^{1/2}} \exp\left[\frac{-1}{2(1-C_{Ma}^2)}\left\{\frac{(M_0-M)^2}{\Delta M^2} - \frac{2C_{Ma}(M_0-M)(a_0-a)}{\Delta M\Delta a} + \frac{(a_0-a)^2}{\Delta a^2}\right\}\right] . \tag{1.4}$$

The variances ΔM and Δa of the inferred mass M_0 and angular momentum a_0 turn out to be (Sec. IV)

$$\Delta M/M = 2.2\rho^{-1}(1-a)^{0.45} f_M(a) ,$$
$$\Delta a = 5.9\rho^{-1}(1-a)^{1.06} f_a(a) , \tag{1.5a}$$

where f_M and f_a are functions that are nearly equal to unity and are tabulated in Table II, ρ is the amplitude signal-to-noise ratio at the output of the filter, and these formulas are valid only for $\rho \gtrsim 10$. Because the best information about M and a comes from the waves' frequency (their ringdown time is less well determined), the fluctuations of M_0 and a_0 away from the true values, $\delta M \equiv M_0 - M$ and $\delta a \equiv a_0 - a$, are strongly correlated; the correlation coefficient appearing in (1.4) is

$$C_{Ma} = 0.976 f_{Ma}(a) , \tag{1.5b}$$

where f_{Ma} (tabulated in Table II) is very nearly equal to unity throughout the range $0 \leq a \leq 1$.

It is important to note that the signal-to-noise ratio ρ at the output of the filter depends not only on the waves' amplitude h_s and the detector's noise S_h; it also depends on how long the waves last, i.e., on their quality factor Q_s [Eq. (1.2)]:

$$\rho = h_s(\omega_s S_h)^{-1/2} 2Q_s^{3/2}(1+4Q_s^2)^{-1/2}$$
$$= h_s[2/(\omega_s S_h)]^{1/2}(1-a)^{-0.22} f_\rho(a)$$
$$= h_s S_h^{-1/2}(GM/c^3)^{1/2}$$
$$\times 2.26(1-a)^{-0.15} f'_\rho(a) . \tag{1.6}$$

Here $f_{\dot\rho}$ and f'_ρ are correction functions close to unity that are tabulated in Table II. The faster the hole rotates, the larger is its quality factor, and thus for fixed initial wave amplitude h_s, the larger is the signal-to-noise ratio ρ and the better determined are the hole's mass and angu-

lar momentum. The determination improves not only due to the increase in ρ. Expressions (1.5a) also show a direct and larger improvement with increasing a in addition to that produced by ρ. They also show that for slowly rotating holes, $a \lesssim 0.8$, the rotation parameter is less accurately determined than the mass, $\Delta a > \Delta M/M$; but for $a \gtrsim 0.8$ it is better determined, $\Delta a < \Delta M/M$.

The body of this paper, in which these and other results are derived, is organized as follows: Section II outlines, briefly, the theory of optimal filtering of signals that are contaminated by noise. Section III uses that theory to determine, for $\rho \gtrsim 5$, the accuracies $\Delta\omega$, $\Delta\tau$ with which the parameters ω_s, τ_s of the waveform (1.3) can be deduced in the presence of the white, Gaussian noise S_h. Section IV translates those $\Delta\omega$ and $\Delta\tau$ into corresponding accuracies (and Gaussian probability distributions) for the inferred mass M_0 and rotation parameter a_0 of the hole. Finally, Sec. V points the direction toward future, followup research.

II. GENERAL APPROACH

In this section we sketch, briefly, the application of Wiener's theory of optimal filtering to our problem.

The experimenters' initial task is to estimate the signal parameters t_s, ω_s, and τ_s from their experimental data—data consisting of the signal (1.3) corrupted by detector noise.

The simplest variant of the Wiener optimal filter deals with a slightly different task: The parameters t_s, ω_s, and τ_s [and thence the full signal $h(t)$] are presumed known in advance, and it is desired merely to determine whether or not the signal is present. For this task the optimal filter $K(t)$ is the one which, when integrated against the noisy signal, gives the largest integrated signal-to-noise ratio.[9] More specifically, let the uncontaminated signal be $h(t)$ [Eq. (1.3)] and let the noise (a Gaussian random process) be $n(t)$. Then the value obtained as output of the optimal filter is

$$W = \int_{-\infty}^{\infty} K(t)[h(t)+n(t)]dt = S+\nu \ , \tag{2.1}$$

where

$$S = \int_{-\infty}^{\infty} K(t)h(t)dt \ , \quad \nu = \int_{-\infty}^{\infty} K(t)n(t)dt \ , \tag{2.2}$$

and $K(t)$ (the optimal filter) is defined by

$$\tilde{K}(f) \propto \tilde{h}(f)/S_h(f) \ . \tag{2.3}$$

Here the tildes denote Fourier transforms, $S_h(f)$ represents the spectral density of the noise $n(t)$, and the constant of proportionality is arbitrary. Note that, while S is a constant, independent of the moment of detection [because if $h(t)$ is shifted in time $K(t)$ is shifted too], ν, in a given experiment, is just an instance of a random variable, and will be different if detected at a different time or even by another identical detector at the same time, since $n(t)$ is a random process. The filter (2.3) is optimal in that it gives the maximum possible value for the output signal-to-noise ratio S/N, where N is the standard deviation of ν considered as a random variable, i.e., $N \equiv \sigma_\nu$.

In our case, the signal's parameters ω_s, τ_s, t_s, and amplitude are unknown; and thus the experimenters cannot know in advance the exact form for the optimal filter function (2.3). However, since the general shape of $h(t)$ is known, and since the optimal filter gives the maximum signal-to-noise ratio S/N on output for the signal it is tailored to, we can (and shall) assume some arbitrary initial parameters (ω_k, τ_k, t_k) for the filter function and then perform a fine-tuning, changing these parameters in order to maximize the output S/N. The maximum value of S/N will occur when (ω_k, τ_k, t_k) are equal to (ω_s, τ_s, t_s).

This maximization of S/N cannot be accomplished exactly in practice, since at the output of the filter we do not know the output signal S and the output noise ν separately, but only their sum W. The best we can do is take the total output W as an estimate of S, apply the above-described procedure to maximize W/N, and thereby obtain estimates (ω_0, τ_0, t_0) of the exact signal parameters. Obviously, the weaker the noise (the higher S/N), the closer these estimates will be to (ω_s, τ_s, t_s).

In this paper we shall compute the uncertainties in (ω_0, τ_0)—i.e., the amounts by which they are expected to deviate from (ω_s, τ_s). Our computation will be based on the statistical properties of the background noise and the effect of the filtering and optimization processes on those statistical properties and on the total (corrupted) signal. We shall carry out this analysis analytically with appropriate approximations for the weak-noise case (large S/N). The same procedure, implemented numerically, could give details of the uncertainties in ω_s, τ_s for the strong-noise case; but we shall not attempt such calculations.

Once the uncertainties in ω_0, τ_0 are known, these can be (and will be) translated into corresponding uncertainties for the mass and angular momentum of the black hole. This can be readily performed using the known numerical results that relate these two sets of parameters.[5,10] We will also find the correlation between these uncertainties.

III. SIGNAL PARAMETERS

The signal function we will use is the damped sinusoid described by Eq. (1.3), which starts at $t = t_s$. For ease of calculation, we will choose $t_s = 0$, so that the estimate t_0 will be distributed around zero, and $h(t)$ will have the form

$$h(t) = \begin{cases} h_s e^{-t/\tau_s} \sin\omega_s t & \text{if } t \geq 0 \ , \\ 0 & \text{if } t < 0 \ . \end{cases} \tag{3.1}$$

We will follow the process described in Sec. II to obtain the estimates ω_0, τ_0, t_0 for ω_s, τ_s, and $t_s = 0$ and to determine how much uncertainty is introduced in the process.

Now, since we assumed that the detector introduces white noise, its spectral density will be constant: $S_h(f) = S_h$ for all f. Then, according to (2.3) the optimal filter would be proportional to the signal $h(t)$. However, since in practice we do not know the values of ω_s, τ_s, or t_s, we are forced to use, as our filter,

$$K(t)=\begin{cases} e^{-(t-t_k)/\tau_k}\sin\omega_k(t-t_k) & \text{if } t\geq t_k\ , \\ 0 & \text{if } t<t_k\ , \end{cases} \tag{3.2}$$

where ω_k, τ_k, and t_k are the parameters that have arbitrary initial values, and are fine-tuned to maximize W/N.

By inserting Eqs. (3.1) and (3.2) into (2.2), we obtain, for the filtered signal,

$$S=\int_{-\infty}^{\infty}K(t)h(t)dt = \begin{cases} \frac{1}{2}h_s e^{t_k/\tau_k}(I_- - I_+) & \text{if } t_k<0\ , \\ \frac{1}{2}h_s e^{-t_k/\tau_s}(J_- - J_+) & \text{if } t_k\geq 0\ , \end{cases} \tag{3.3}$$

with

$$I_\pm=(\tau\cos\omega_k t_k+\tau^2\omega_\pm\sin\omega_k t_k)/(1+\omega_\pm^2\tau^2)\ , \tag{3.4}$$

$$J_\pm=(\tau\cos\omega_s t_k\mp\tau^2\omega_\pm\sin\omega_s t_k)/(1+\omega_\pm^2\tau^2)\ ,$$

where $\tau\equiv\tau_k\tau_s/(\tau_k+\tau_s)$ and $\omega_\pm\equiv\omega_k\pm\omega_s$.

We will now analyze ν, the output of the filter when the input is $n(t)$. We can look at ν in two very different ways. First, we can consider it as just the real number obtained, added to the useful output S, in one specific experiment. Second, we can view it as the random variable corresponding to the different results that an ensemble of identical detectors would give for the same experiment. We must use the first viewpoint when we try to reproduce the steps that would be followed in the analysis of the data from an actual experiment, e.g., the fine-tuning of parameters by maximization of the output signal-to-noise ratio. We need, however, to use the second point of view when we want to study the statistical variations that are to be expected in actual experiments, given the fact that $n(t)$ is unpredictable.

From (2.2) and (3.2), ν is given by

$$\nu=\int_{-\infty}^{\infty}K(t)n(t)dt = \int_0^{\infty}e^{-t/\tau_k}\sin\omega_k t\, n(t+t_k)dt\ . \tag{3.5}$$

Viewing this ν as a random variable, we see that its distribution is Gaussian, since it is a linear combination of the Gaussian random variables $n(t+t_k)$ (Ref. 11). As an aid in evaluating the variance σ_ν^2 of ν we introduce the random process

$$\mathfrak{N}(t')=\int_{-\infty}^{\infty}K(t-t')n(t)dt\ , \tag{3.6}$$

so that $\nu=\mathfrak{N}(0)$. The spectral density of this $\mathfrak{N}(t')$ will then be[12]

$$S_{\mathfrak{N}}(f)=|\tilde{K}(f)|^2S_h(f)=S_h|\tilde{K}(f)|^2\ . \tag{3.7}$$

Consequently, the variance of the random process $\mathfrak{N}(t')$ will be

$$\sigma_{\mathfrak{N}}^2=\int_0^{\infty}S_{\mathfrak{N}}(f)df=S_h\int_0^{\infty}|\tilde{K}(f)|^2df = (S_h/2)\int_{-\infty}^{\infty}|\tilde{K}(f)|^2df = (S_h/2)\int_{-\infty}^{\infty}K^2(t)dt\ , \tag{3.8}$$

where the first equality follows from the definition of spectral density,[13] and the last one from Parseval's theorem. However, the random variable $\nu=\mathfrak{N}(0)$ is just the value of the random process $\mathfrak{N}$ at one specific time, so their variances are the same: $\sigma_\nu^2=\sigma_{\mathfrak{N}}^2$. Hence,

$$N^2\equiv\sigma_\nu^2=\langle\nu^2\rangle=(S_h/2)\int_{-\infty}^{\infty}K^2(t)dt = (S_h/8)\omega_k^2\tau_k^3/(1+\omega_k^2\tau_k^2)\ . \tag{3.9}$$

We now want to perform the maximization of our "best estimate" of the signal-to-noise ratio, $W/N=(S+\nu)/N$. It is impossible to do this analytically to obtain an expression for the optimal values of ω_k, τ_k, and t_k since the expressions (3.3) and (3.9) are not simple enough. If, however, we restrict ourselves to the case in which the noise is sufficiently low, i.e., S/N is big enough, we can assume that the optimal values for the filter parameters will be relatively close to the exact signal parameters. In this case we can write

$$\omega_k=\omega_s(1+\varepsilon)\ ,\quad \tau_k=\tau_s(1+\eta)\ , \quad t_k=\zeta/\omega_s\ , \tag{3.10}$$

where we need only consider values of ε, η, and ζ much smaller than 1. We can then show that, in this approximation, we get the simple expression

$$S/N=\rho(1-\alpha_1\varepsilon^2-\alpha_2\eta^2-\alpha_3\zeta^2 +\beta_1\varepsilon\eta+\beta_2\varepsilon\zeta+\beta_3\eta\zeta)\ , \tag{3.11}$$

where the coefficients can be expressed in terms of the quantities

$$Q_s\equiv\tfrac{1}{2}\omega_s\tau_s\ , \quad q_s\equiv 2Q_s(1+4Q_s^2)^{-1/2}=\omega_s\tau_s(1+\omega_s^2\tau_s^2)^{-1/2}\ , \tag{3.12}$$

which are dependent only on the product of the signal's frequency and damping time, and not on each separately. The parameter Q_s is the resonance factor or quality factor for the damped wave. Note that q_s can only take values between 0 and 1, but for the values of ω_s and τ_s corresponding to the fundamental normal mode with $l=m=2$ of Kerr black holes, Q_s ranges from about 2 to ∞ [see Eq. (4.3)], so q_s is always very close to unity. In terms of these parameters the coefficients in (3.11) are

$$\begin{aligned} \rho&=q_s h_s(\tau_s/2S_h)^{1/2}\ , \\ \alpha_1&=\tfrac{1}{2}q_s^4-\tfrac{1}{4}q_s^2+Q_s^2\ , \\ \alpha_2&=\tfrac{1}{2}q_s^4-\tfrac{3}{4}q_s^2+\tfrac{3}{8}\ , \\ \alpha_3&=\tfrac{1}{2}q_s^{-2}\ , \\ \beta_1&=-\,q_s^4+q_s^2\ , \\ \beta_2&=Q_s\ , \\ \beta_3&=-\tfrac{1}{4}Q_s^{-1}\ . \end{aligned} \tag{3.13}$$

We can do something similar with the noise contribution to W/N: we can construct a series expansion for ν in powers of ε, η, and ζ and keep the leading terms. In order to do this, we note that from (3.5) and (3.10) the filter function depends not only on t, but also on ε, η, and ζ; i.e., it can be expressed as $K(\varepsilon,\eta,\zeta,t)$. Therefore, it can be expanded in powers of ε, η, and ζ. Keeping terms up to first order, we get

$$K(\varepsilon,\eta,\zeta,t)=\begin{cases} f_0(t)+f_1(t)\varepsilon+f_2(t)\eta+f_3(t)\zeta & \text{if } t\geq 0\ , \\ 0 \text{ if } t<0\ , \end{cases} \tag{3.14}$$

where

$$\begin{aligned} f_0(t)&=e^{-t/\tau_s}\sin\omega_s t\ , \\ f_1(t)&=\omega_s t e^{-t/\tau_s}\cos\omega_s t\ , \\ f_2(t)&=(t/\tau_s)e^{-t/\tau_s}\sin\omega_s t\ , \\ f_3(t)&=e^{-t/\tau_s}(\tfrac{1}{2}Q_s^{-1}\sin\omega_s t-\cos\omega_s t)\ . \end{aligned} \tag{3.15}$$

Therefore, the expansion for ν is

$$\nu=\nu_0+\nu_1\varepsilon+\nu_2\eta+\nu_3\zeta\ , \tag{3.16}$$

where

$$\nu_i=\int_0^\infty f_i(t)n(t)dt \quad \text{for } i=0,\ldots,3 \tag{3.17}$$

can be viewed as four Gaussian random variables independent of the filter. Next, taking into account the dependence of N on ε, η, and ζ, we get

$$\nu/N=b(c_0+c_1\varepsilon+c_2\eta+c_3\zeta)\ , \tag{3.18}$$

where

$$\begin{aligned} b&=q_s^{-1}(8/S_h\tau_s)^{1/2}\ , \\ c_0&=\nu_0\ , \quad c_1=\nu_1-(1-q_s^2)\nu_0\ , \\ c_2&=\nu_2-(\tfrac{3}{2}-q_s^2)\nu_0\ , \quad c_3=\nu_3\ . \end{aligned} \tag{3.19}$$

Note that the c_i, like the ν_i, are Gaussian random variables. By adding expressions (3.11) and (3.18) we obtain $W/N=(S+\nu)/N$.

Now, we are ready to maximize $(S+\nu)/N$. The values $(\varepsilon,\eta,\zeta)=(\varepsilon_0,\eta_0,\zeta_0)$ for which

$$\nabla_{\varepsilon,\eta,\zeta}[(S+\nu)/N]=0 \tag{3.20}$$

are our best estimate of $(\varepsilon_s,\eta_s,\zeta_s)$ for a given experiment. By imposing (3.20) with the help of (3.11) and (3.18) we obtain the linear equations

$$\begin{bmatrix} 2\alpha_1 & -\beta_1 & -\beta_2 \\ -\beta_1 & 2\alpha_2 & -\beta_3 \\ -\beta_2 & -\beta_3 & 2\alpha_3 \end{bmatrix}\begin{bmatrix} \varepsilon_0 \\ \eta_0 \\ \zeta_0 \end{bmatrix}=\rho^{-1}b\begin{bmatrix} c_1 \\ c_2 \\ c_3 \end{bmatrix}\ . \tag{3.21}$$

The solution of these linear equations, rewritten using (3.13) and (3.19), is

$$\begin{aligned} \delta\omega_s/\omega_s\equiv\varepsilon_0&=k(d_0\nu_0+d_1\nu_1+d_2\nu_2+d_3\nu_3)\ , \\ \delta\tau_s/\tau_s\equiv\eta_0&=k(e_0\nu_0+e_1\nu_1+e_2\nu_2+e_3\nu_3)\ , \end{aligned} \tag{3.22}$$

with

$$\begin{aligned} d_0&=-(\tfrac{1}{4}+\tfrac{1}{16}Q_s^{-2})q_s^2+(\tfrac{9}{8}+\tfrac{1}{16}Q_s^{-2})-\tfrac{3}{4}q_s^{-2}\ , \\ d_1&=q_s^2-(\tfrac{3}{2}+\tfrac{1}{16}Q_s^{-2})+\tfrac{3}{4}q_s^{-2}\ , \\ d_2&=-q_s^2+\tfrac{3}{4}\ , \\ d_3&=(Q_s+\tfrac{1}{4}Q_s^{-1})q_s^4-(\tfrac{3}{2}Q_s+\tfrac{1}{4}Q_s^{-1})q_s^2+\tfrac{3}{4}Q_s\ , \\ e_0&=-(Q_s^2+\tfrac{1}{4})q_s^2+\tfrac{7}{2}Q_s^2-3Q_s^2q_s^{-2}\ , \\ e_1&=-q_s^2+\tfrac{3}{4}\ , \\ e_2&=q_s^2-(Q_s^2+\tfrac{1}{2})+2Q_s^2q_s^{-2}\ , \\ e_3&=-(Q_s+\tfrac{1}{4}Q_s^{-1})q_s^4+(Q_s+\tfrac{1}{8}Q_s^{-1})q_s^2-\tfrac{1}{2}Q_s\ , \\ k&=4\Delta^{-1}/(h_s q_s^2\tau_s)\ , \end{aligned} \tag{3.22a}$$

where Δ, the determinant of the 3×3 matrix in (3.21), is given by

$$\begin{aligned} \Delta=&-(Q_s^2+\tfrac{1}{2}+\tfrac{1}{16}Q_s^{-2})q_s^4 \\ &+(\tfrac{7}{2}Q_s^2+1+\tfrac{1}{32}Q_s^{-2})q_s^2 \\ &-(\tfrac{15}{4}Q_s^2+\tfrac{1}{2})+\tfrac{3}{2}Q_s^2q_s^{-2}\ . \end{aligned} \tag{3.22b}$$

Analogous expressions can be obtained for ζ_0, but we do not give them, since in this paper we are not interested in the accuracy of the start time. (Our only reason for including $\zeta=\omega_s t_k$ in the analysis was to take account of its impact on the accuracy of read-out of ω_s and τ_s.)

We should notice that ε_0 and η_0 will, in general, be correlated, since they are ultimately dependent on the same random process $n(t)$. Furthermore, since this process is Gaussian and the dependencies are linear, they will have a joint normal distribution, with probability density

$$f(\varepsilon_0,\eta_0)=\frac{1}{2\pi\sigma_{\varepsilon_0}\sigma_{\eta_0}(1-r_{\varepsilon_0\eta_0}^2)^{1/2}}\exp\left[-\frac{1}{2(1-r_{\varepsilon_0\eta_0}^2)}\left(\frac{\varepsilon_0^2}{\sigma_{\varepsilon_0}^2}-\frac{2r_{\varepsilon_0\eta_0}\varepsilon_0\eta_0}{\sigma_{\varepsilon_0}\sigma_{\eta_0}}+\frac{\eta_0^2}{\sigma_{\eta_0}^2}\right)\right]\ , \tag{3.23}$$

where $r_{\varepsilon_0\eta_0}$ is their *correlation coefficient*, and σ_{ε_0} and σ_{η_0} are the standard deviations of ε_0 and η_0, respectively (after integrating over the other variable). Once we have computed σ_{ε_0}, σ_{η_0}, and $r_{\varepsilon_0\eta_0}$ we will know from (3.23) all the statistical properties of ε_0 and η_0.

In order to compute σ_{ε_0}, σ_{η_0}, and $r_{\varepsilon_0\eta_0}$, we must express ε_0 and η_0 as linear combinations of the values of $n(t)$ [i.e., as integrals over $n(t)$]. By combining equations (3.17) and (3.22) we obtain the explicit expressions

$$\varepsilon_0=\int_0^\infty g(t)n(t)\,,\qquad \eta_0=\int_0^\infty h(t)n(t)\,,\tag{3.24}$$

where

$$g(t)=k\sum_{i=0}^{3} d_i f_i(t)\,,\qquad h(t)=k\sum_{i=0}^{3} e_i f_i(t)\,.\tag{3.24a}$$

Then by analogy with (3.5) and (3.8) we obtain, for the variances,

$$\begin{aligned}(\Delta\omega_s/\omega_s)^2\equiv\sigma_{\varepsilon_0}^2&=\langle\varepsilon_0^2\rangle\\&=(S_h/2)\int_0^\infty g^2(t)dt\\&=(k^2S_h/2)\sum_{i,j=0}^{3} d_i d_j I_{ij}\,,\\(\Delta\tau_s/\tau_s)^2\equiv\sigma_{\eta_0}^2&=\langle\eta_0^2\rangle\\&=(S_h/2)\int_0^\infty h^2(t)dt\\&=(k^2S_h/2)\sum_{i,j=0}^{3} e_i e_j I_{ij}\,,\end{aligned}\tag{3.25}$$

where

$$I_{ij}\equiv\int_0^\infty f_i(t)f_j(t)dt\,.\tag{3.26}$$

Here we have defined the "typical fractional errors" $\Delta\omega_s/\omega_s$ and $\Delta\tau_s/\tau_s$ in the signal parameters to be their standard deviations. [These standard deviations should not be confused with the actual—but unknown—fractional errors $\delta\omega_s/\omega_s\equiv(\omega_0-\omega_s)/\omega_s$ and $\delta\tau_s/\tau_s=(\tau_0-\tau_s)/\tau_s$.] Explicit calculation of the integrals I_{ij} yields

$$\begin{aligned}&I_{00}=\tfrac{1}{4}\tau_s q_s^2\,,\\&I_{11}=\tfrac{1}{2}\tau_s Q_s^2(-4q_s^6+9q_s^4-6q_s^2+2)\,,\\&I_{22}=\tfrac{1}{8}\tau_s q_s^2(4q_s^4-9q_s^2+6)\,,\\&I_{33}=\tfrac{1}{4}\tau_s\,,\\&I_{01}=I_{10}=\tfrac{1}{4}\tau_s q_s^2(1-q_s^2)\,,\\&I_{02}=I_{20}=\tfrac{1}{8}\tau_s q_s^2(3-2q_s^2)\,,\\&I_{03}=I_{30}=0\,,\\&I_{12}=I_{21}=\tfrac{1}{2}\tau_s Q_s^2(-4q_s^6+11q_s^4-10q_s^2+3)\,,\\&I_{13}=I_{31}=-\tfrac{1}{4}\tau_s Q_s q_s^2\,,\\&I_{23}=I_{32}=\tfrac{1}{4}\tau_s Q_s(1-q_s^2)\,.\end{aligned}\tag{3.27}$$

To compute the correlation coefficient $r_{\varepsilon_0\eta_0}$ we begin by evaluating

$$\begin{aligned}r_{\varepsilon_0\eta_0}\sigma_{\varepsilon_0}\sigma_{\eta_0}&=\langle\varepsilon_0\eta_0\rangle\\&=\left\langle\int_0^\infty g(t)n(t)dt\int_0^\infty h(t')n(t')dt'\right\rangle\\&=\int_0^\infty dt\int_0^\infty dt' g(t)h(t')\langle n(t)n(t')\rangle\\&=\int_0^\infty dt\int_0^\infty dt' g(t)h(t')(S_h/2)\delta(t-t')\\&=(S_h/2)\int_0^\infty g(t)h(t)dt\,.\end{aligned}\tag{3.28}$$

Here we have used the equality $\langle n(t)n(t')\rangle=(S_h/2)\delta(t-t')$, which follows from the fact that the noise's correlation function $C_n(\tau)\equiv\langle n(t)n(t+\tau)\rangle$ is the cosine transform of its spectral density $S_h(f)$ (Wiener-Khintchine theorem). Next, using (3.24a) and (3.26) in (3.28) we obtain

$$\begin{aligned}\langle\varepsilon_0\eta_0\rangle&=r_{\varepsilon_0\eta_0}\sigma_{\varepsilon_0}\sigma_{\eta_0}\\&=(k^2S_h/2)\sum_{i,j=0}^{3} e_i d_j I_{ij}\,.\end{aligned}\tag{3.29}$$

From (3.25) and (3.29) we can draw the conclusion that the correlation coefficient $r_{\varepsilon_0\eta_0}$ is a function of Q_s only; i.e., it does not depend on the frequency or damping time of the signal separately. Moreover, it does not depend on the noise level that is present in the detector or on the initial amplitude of the signal.

Using the fact that $Q_s>2$ and $q_s\approx1$, we can see that only one or a few of the terms in the sums (3.25) and (3.29) make significant contributions to σ_{ε_0}, σ_{η_0}, and $r_{\varepsilon_0\eta_0}$. By identifying and evaluating the dominant terms, we can find the following analytical expressions for the uncertainties in the signal parameters and their correlation:

$$\begin{aligned}&\Delta\omega_s/\omega_s\equiv\sigma_{\varepsilon_0}=\rho^{-1}Q_s^{-1}f_\omega(Q_s)\,,\\&\Delta\tau_s/\tau_s\equiv\sigma_{\eta_0}=2\rho^{-1}f_\tau(Q_s)\,,\\&C_{\omega_s\tau_s}\equiv\mathrm{Corr}(\delta\omega_s/\omega_s;\delta\tau_s/\tau_s)\\&\qquad\equiv r_{\varepsilon_0\eta_0}=-\tfrac{1}{2}Q_s^{-1}f_{\omega\tau}(Q_s)\,.\end{aligned}\tag{3.30}$$

Here ρ [Eq. (3.13)] is the signal-to-noise ratio, aside from small corrections that are shown in Eq. (3.11); and f_ω, f_τ, $f_{\omega\tau}$ are "correction functions" which depend on the quality factor Q_s and are very close to unity. These correction functions are tabulated in Table I.

These results can be summarized as follows: The fractional uncertainties in the frequency and damping time are inversely proportional to the signal-to-noise-ratio ρ. The uncertainty in the frequency is very nearly inversely proportional to the signal's quality factor, while the uncertainty in the damping time is essentially independent of the quality factor. Finally, the correlation coefficient, which is independent of the signal-to-noise ratio, is nearly inversely proportional to Q_s; and, given the numerical values of Q_s for the fundamental normal mode with

TABLE I. Corrections for the uncertainties and correlation of the signal's frequency and damping time as functions of Q_s. These corrections are defined in Eqs. (3.30).

Q_s	f_ω	f_τ	$f_{\omega\tau}$
2.1	0.9480	1.1021	0.7517
5.0	0.9902	1.0196	0.9513
10.0	0.9975	1.0050	0.9876
15.0	0.9989	1.0022	0.9945
20.0	0.9994	1.0012	0.9969
25.0	0.9996	1.0008	0.9980
30.0	0.9997	1.0006	0.9986
35.0	0.9998	1.0004	0.9990
40.0	0.9998	1.0003	0.9992
45.0	0.9999	1.0002	0.9994
50.0	0.9999	1.0002	0.9995
55.0	0.9999	1.0002	0.9996
60.0	1.0000	1.0001	0.9996
65.0	1.0000	1.0001	0.9997
70.0	1.0000	1.0001	0.9997
75.0	1.0000	1.0001	0.9998
80.0	1.0000	1.0001	0.9998

$l=m=2$ of Kerr black holes, the correlation coefficient turns out to be small for all the range of interest, and absolutely negligible for rapidly rotating holes (high Q_s). This means that the errors in the values of ω_s and τ_s obtained in one specific experiment will be essentially independent of each other.

From these results we can see that the condition $\varepsilon,\eta \ll 1$, on which our analysis relies, is satisfied if and only if

$$\rho \gg 1 . \tag{3.31}$$

By using the results obtained to check the errors in the approximate expansions (3.11) and (3.14) for typical values of ε_0 and η_0, it is found that with $\rho=5$ these are $\lesssim 10\%$ for all Q_s, so the results can be considered valid for $\rho \gtrsim 5$.

Let us now briefly look at the initial amplitude h_s of the signal. We will show how it can be determined from the experiment, and why the lack of knowledge of its precise value does not significantly affect our knowledge of the uncertainties and correlation coefficient of the frequency and damping time.

From the experimental data, we have to take $W=S+\nu$ as our best estimate for S. Then, from this best estimate, using (3.3) and using ω_0, τ_0, t_0 in place of ω_k, τ_k, t_k, we obtain a best estimate of h_s. Because of the presence of ν in $W=S+\nu$ and the deviations of ω_0, τ_0, t_0 from ω_s, τ_s, t_s, this procedure produces fractional errors of order ρ^{-1} in our estimated h_s. Similarly, there are fractional errors of order ρ^{-1} in our estimate W/N for the value of $\rho=S/N$—and these errors produce fractional errors of order ρ^{-1} in our knowledge of the values of $\Delta\omega_s/\omega_s$, $\Delta\tau_s/\tau_s$, and $C_{\omega_s\tau_s}$ [Eqs. (3.30)]. For $\rho \gtrsim 5$ we can regard these errors as negligible.

IV. BLACK-HOLE PARAMETERS

We now describe the final step of our analysis: the translation from the values and uncertainties for the signal parameters ω_s and τ_s into those of the mass M and angular momentum parameter a of the black hole. In order to make this translation, we need the functional relationship between the two pairs of variables (ω_s, τ_s) and (M, a). That relationship has been computed numerically by Leaver[5] using the theory of small perturbations of Kerr black holes. We shall write that relationship in the form[4]

$$\omega_s = f(a)/M , \qquad \tau_s = g(a)M , \tag{4.1}$$

where the functions $f(a)$ and $g(a)$ are plotted in Fig. 3(c) of Leaver (Ref. 5); and we shall write the inverse relation as

$$a=\phi(Q_s) , \qquad M=\psi(Q_s)/\omega_s . \tag{4.2}$$

The functions $\phi(Q_s)$ and $\psi(Q_s)$ can be determined from tables of $f(a)$ and $g(a)$ (obtained by private communication from Leaver, since they are not tabulated in Ref. 5 for the case $l=m=2$).

It is interesting to notice that the angular momentum parameter a depends only on the resonance factor Q_s and, furthermore, that this dependence is monotonic and thus invertible. An analytical expression for the inverse function is

$$\begin{aligned} Q_s &= \tfrac{1}{2}\omega_s\tau_s = f(a)g(a) \\ &= 2(1-a)^{-0.45} f_Q(a) , \end{aligned} \tag{4.3}$$

where the approximate expression is corrected by f_Q, which is close to unity, and is tabulated in Table II. For the sake of completeness we also give an analytical expression for the function $f(a)$, which determines the frequency ω_s:

$$f(a)=[1-0.63(1-a)^{0.3}]f_f(a) , \tag{4.4}$$

where the correction is also given in Table II.

We now want to know how the uncertainties in the signal parameters are translated into the corresponding uncertainties of the hole's parameters. In order to determine this we replace ω_s and τ_s in (4.2) with the values ω_0 and τ_0 obtained by the procedure described in Sec. III, thus obtaining approximate values a_0 and M_0 (the experimenter's best estimates) for the hole's angular momentum parameter a and mass M. These can be written as

$$a_0 = a+\xi , \qquad M_0 = M(1+\mu) , \tag{4.5}$$

where ξ and μ are the errors the experimenter makes. Then, using expressions (3.10) and the approximations $\varepsilon_0, \eta_0 \ll 1$, we obtain linearized expressions for these errors:

$$\begin{aligned} \xi &= \delta a = A\varepsilon_0 + B\eta_0 , \\ \mu &= \delta M/M = C\varepsilon_0 + D\eta_0 , \end{aligned} \tag{4.6}$$

with A, B, C and D given by

$$\begin{aligned} A &= B = Q_s\phi'(Q_s) , \\ D &= C+1 = Q_s\psi'(Q_s)/\psi(Q_s) . \end{aligned} \tag{4.7}$$

TABLE II. Corrections for quality factor, signal-to-noise ratio, and hole's mass and angular momentum parameter as functions of a. These corrections are defined in Eqs. (4.3), (4.4), (4.10), (4.11), and (4.15).

a	f_Q	f_f	f_a	f_M	f_{Ma}	f_ρ	f'_a	f'_M	f'_ρ
0.0001	1.0501	1.0100	1.0237	0.9417	1.0000	0.9969	1.0044	0.9239	1.0192
0.1000	1.0402	0.9934	1.0165	0.9541	1.0000	0.9947	1.0097	0.9478	1.0067
0.2000	1.0297	0.9789	1.0094	0.9685	1.0000	0.9922	1.0162	0.9750	0.9933
0.3000	1.0182	0.9668	1.0026	0.9846	1.0001	0.9895	1.0242	1.0058	0.9789
0.4000	1.0057	0.9572	0.9954	1.0025	1.0001	0.9864	1.0332	1.0406	0.9634
0.5000	0.9918	0.9505	0.9870	1.0215	1.0002	0.9828	1.0429	1.0794	0.9464
0.6000	0.9763	0.9475	0.9762	1.0409	1.0001	0.9786	1.0521	1.1219	0.9278
0.7000	0.9587	0.9494	0.9605	1.0589	0.9997	0.9739	1.0585	1.1670	0.9074
0.8000	0.9389	0.9587	0.9442	1.0724	0.9990	0.9688	1.0666	1.2114	0.8853
0.9000	0.9184	0.9815	0.9233	1.0764	0.9977	0.9649	1.0679	1.2450	0.8646
0.9200	0.9149	0.9891	0.9215	1.0755	0.9973	0.9650	1.0689	1.2475	0.8621
0.9400	0.9124	0.9983	0.9171	1.0722	0.9969	0.9659	1.0644	1.2445	0.8616
0.9600	0.9121	1.0099	0.9036	1.0636	0.9963	0.9685	1.0441	1.2289	0.8655
0.9800	0.9187	1.0252	0.9246	1.0512	0.9959	0.9763	1.0468	1.1902	0.8832
0.9850	0.9236	1.0297	0.9285	1.0427	0.9958	0.9806	1.0383	1.1661	0.8942
0.9900	0.9326	1.0346	0.9408	1.0307	0.9956	0.9876	1.0304	1.1289	0.9131
0.9950	0.9523	1.0392	0.9695	1.0083	0.9955	1.0018	1.0169	1.0577	0.9533

Given the shapes of the functions $\phi(Q_s)$ and $\psi(Q_s)$, it is found empirically that the linear expansion (4.6) is a good approximation as long as the condition $\epsilon_0, \eta_0 \ll 1$ holds. More precisely: using σ_{ϵ_0}, σ_{η_0} from (3.30) as typical values for ϵ_0, η_0, it turns out that the differences between the exact ξ and μ [defined by (4.5)] and their approximate values [defined by (4.6)] are $\lesssim 30\%$ for $\rho \gtrsim 10$. So we will consider the results obtained below to be valid only for $\rho \gtrsim 10$.

Finally, we need to determine the probability distribution of ξ and μ. Since ϵ_0 and η_0 have a joint Gaussian probability distribution, ξ and μ, which are the linear combinations (4.6) of ϵ_0 and η_0, also have a joint Gaussian distribution[11] with variances and correlation given by

$$\sigma_\xi^2 = A^2\sigma_{\epsilon_0}^2 + B^2\sigma_{\eta_0}^2 + 2AB r_{\epsilon_0\eta_0}\sigma_{\epsilon_0}\sigma_{\eta_0} ,$$
$$\sigma_\mu^2 = C^2\sigma_{\epsilon_0}^2 + D^2\sigma_{\eta_0}^2 + 2CD r_{\epsilon_0\eta_0}\sigma_{\epsilon_0}\sigma_{\eta_0} , \tag{4.8}$$
$$r_{\xi\mu}\sigma_\xi\sigma_\mu = AC\sigma_{\epsilon_0}^2 + BD\sigma_{\eta_0}^2 + (AD+BC) r_{\epsilon_0\eta_0}\sigma_{\epsilon_0}\sigma_{\eta_0} .$$

Correspondingly, the typical errors in the estimated black-hole mass M and angular momentum parameter a, and the correlation of those errors, have the general form

$$\Delta a \equiv \sigma_\xi = \rho^{-1}F(Q_s) = \rho^{-1}\hat{F}(a) ,$$
$$\Delta M/M \equiv \sigma_\mu = \rho^{-1}G(Q_s) = \rho^{-1}\hat{G}(a) , \tag{4.9}$$
$$C_{Ma} \equiv \mathrm{Corr}(\delta a ; \delta M/M)$$
$$\equiv r_{\xi\mu} = H(Q_s) = \hat{H}(a) ,$$

where the functions F, G, H and $\hat{F}$, $\hat{G}$, $\hat{H}$ are computable from Eqs. (3.30), (4.2), (4.7), (4.8), and Leaver's numerical results for $\phi(Q_s)$ and $\psi(Q_s)$. It is important to note that both the uncertainties Δa and $\Delta M/M$ are inversely proportional to the output signal-to-noise ratio ρ, and that their correlation depends only on a, and not on M. The author has evaluated the functions $\hat{F}$, $\hat{G}$, and $\hat{H}$ by the above prescription. The numerical results can be expressed in the form

$$\Delta M/M = 2.2\rho^{-1}(1-a)^{0.45} f_M(a) , \tag{4.10a}$$
$$\Delta a = 5.9\rho^{-1}(1-a)^{1.06} f_a(a) , \tag{4.10b}$$
$$C_{Ma} = 0.976 f_{Ma}(a) , \tag{4.10c}$$

where f_M, f_a, and f_{Ma} are corrections that are close to unity and are given in Table II.

Expression (4.10b) shows that, for a given ρ, the uncertainty in the angular momentum parameter a decreases in a nearly linear way as a increases, vanishing for $a = 1$. If we now take into consideration the multiplicative factor, it turns out that to get a reasonable precision in an estimate of a black hole's angular momentum, the hole would have to rotate very rapidly, or else we would need a very high signal-to-noise ratio.

By contrast with a, the fractional error $\Delta M/M$ in the mass does not decrease so rapidly with increasing rotation of the black hole. However, the multiplicative factor in (4.10a) is small enough that $\Delta M/M$ can be small for all the range of a (including the Schwarzschild case, $a = 0$) with just a moderate signal-to-noise ratio ($\rho \gtrsim 10$). There is a crossover at $a \simeq 0.8$; above the crossover $\Delta a < \Delta M/M$, i.e., a is better determined than M.

We should note the fact that ρ is not independent of a, since it is defined in terms of τ_s (or ω_s) and Q_s [Eq. (3.13)]. For fixed signal amplitude h_s and detector noise S_h, ρ increases with increasing a as given by

$$\rho = h_s[2/(\omega_s S_h)]^{1/2}(1-a)^{-0.22} f_\rho(a)$$
$$= h_s S_h^{-1/2}(GM/c^3)^{1/2} 2.26(1-a)^{-0.15} f'_\rho(a) , \tag{4.11}$$

where in the last step we replaced ω_s with its dependency on a and M as given by Eq. (4.1), and where f_ρ and f'_ρ are corrections given in Table II.

The correlation between the two uncertainties [Eq. (4.10c)] turns out to be remarkably high: it is essentially independent of the rotation rate and very close to unity. This is due to the fact that δa and $\delta M/M$ are a linear combination of the $\delta\omega_s/\omega_s$ and $\delta\tau_s/\tau_s$ [Eq. (4.6)], and since the damping time is much less well determined than the frequency ($\delta\omega_s/\omega_s \ll \delta\tau_s/\tau_s$), the uncertainties in the mass and angular momentum are produced almost entirely by the uncertainty in the damping time. Thus, the errors δa and $\delta M/M$ must be highly correlated. This high correlation means that if the error is big (or small) in one of the parameters a or M, it is highly likely that the error in the other is also big (or small) and of the same sign.

We can quantify this statement a little better by studying the pair of uncorrelated variables

$$z_{\pm} \equiv \frac{\xi}{\sigma_\xi} \pm \frac{\mu}{\sigma_\mu} = \frac{\delta a}{\Delta a} \pm \frac{\delta M}{\Delta M} , \tag{4.12}$$

which are linear combinations of $\delta a \equiv \xi$ and $\delta M/M \equiv \mu$. Using the analog of Eq. (4.8), it can be shown that the correlation of z_+ and z_- vanishes and that their standard deviations are given by

$$\sigma_{z_\pm} = \sqrt{2(1 \pm r_{\xi\mu})} . \tag{4.13}$$

We see that, as we should have expected, one of these variables, z_+, is very poorly determined relative to the other, since its standard deviation is nearly equal to 2 for all a, while the other, z_-, is very well determined, since its standard deviation is very small, $\sigma_{z_-} \simeq 0.22$ independent of a. This means that we can expect to have

$$|\delta a/\Delta a - \delta M/\Delta M| \lesssim 0.22 . \tag{4.14}$$

That is, for one specific experiment, the ratio of the actual error δa that we make in our estimate of a to the typical error Δa does not differ from the ratio of the actual error in the mass δM to the typical error ΔM by more than 0.22 typically. Thus, the errors in a and M have almost the same relative magnitude and the same sign. This might be of importance in case there is some independent and more precise determination of either the mass or the angular momentum but not both. Then we could readily obtain an almost equally better estimate of the other parameter with very high certainty.

Finally, we reexpress $\Delta M/M$ and Δa of Eqs. (4.10) in a form that depends solely on the signal's amplitude h_s, the detectors' spectral density of noise S_h, and the hole's M and a. This form is obtained by inserting expression (4.11) for $\rho(M,a,S_h,h_s)$ into (4.10). The result is

$$\Delta M/M = 0.14 \left[\frac{10^{-20}}{h_s}\right] \left[\frac{S_h^{1/2}}{10^{-23}\ \mathrm{Hz}^{-1/2}}\right] \times \left[\frac{10M_\odot}{M}\right] (1-a)^{0.60} f'_M(a) , \tag{4.15a}$$

$$\Delta a = 0.37 \left[\frac{10^{-20}}{h_s}\right] \left[\frac{S_h^{1/2}}{10^{-23}\ \mathrm{Hz}^{-1/2}}\right] \times \left[\frac{10M_\odot}{M}\right] (1-a)^{1.21} f'_a(a) , \tag{4.15b}$$

where f'_M and f'_a are correction functions tabulated in Table II, and where one should keep in mind that the waves' frequency ω_s and damping time τ_s are given in terms of M and a by Eqs. (4.1), (4.3), and (4.4).

V. ISSUES FOR FUTURE RESEARCH

This paper constitutes a first, approximate, study of the problem of extracting black-hole parameters from broad-band gravitational-wave data. Several issues not treated here deserve future study.

This paper's analysis is valid only for rather large signal-to-noise ratios, $\rho \gtrsim 10$. However, most gravitational-wave bursts observed by future Earth-based detectors are likely to have $\rho \simeq 5$ [see Eq. (34) of Ref. 8]. Our analysis could be extended to such bursts (or even smaller ρ's) by using a numerical implementation of our optimal filter algorithm, together with a numerical (Monte Carlo) simulation of the detector noise. This could also be achieved by evaluating exactly the uncertainties in the black hole's mass and angular momentum, instead of using a linear approximation [Eq. (4.6)], since we found that it is this step that introduces the largest errors, reducing the range of validity of the results from $\rho \gtrsim 5$ to $\rho \gtrsim 10$. We should also note that the Monte Carlo approach would be worthwhile in itself, since it would also make it possible to analyze the effect on the accuracy of the estimates due to arbitrary transient waveforms and other changes in our initial assumptions.

In this paper attention was restricted to black-hole events in which only the most slowly damped, $l=m=2$ mode is excited. While many black-hole events should satisfy this restriction (see the abstract and Introduction), others will not. For example, axisymmetric collapse will excite only $m=0$ modes and is likely to excite several such modes significantly.[14] It would be useful to extend this paper's analysis to such multimode situations.

This paper ignored the gravitational-wave transient that precedes the ringdown waves. It would be useful to redo the analysis with waveforms that include the transients. One especially important case would be the gravitational waves from the spiraling orbital motion and the coalescence of a two-hole binary system to form a single, larger hole. In this case the full waveform would consist of a Keplerian, spiraling portion (periodic with increasing frequency) [Eqs. (42) of Ref. 8], followed by a several-cycle coalescence wave, followed by the ringdown wave. Although the precise form of the coalescence wave is not yet known (future supercomputer simulations will tell it to us), a reasonable guess at it could be made for exploratory purposes. It would be interesting to see how much can be learned about the two initial holes and the final hole, in the presence of detector noise, from the combination of the three pieces of the waveform: spiraling, coalescence, and ringdown. Such a study would constitute a marriage and extension of this paper's results and methods, and those of Smith,[15] who has studied the extraction of information from the spiraling portion of the waveform.

ACKNOWLEDGMENTS

I wish to thank Dr. Kip S. Thorne, for suggesting this problem to me and for many suggestions that helped me with the research and in writing this paper. I am also indebted to Dr. E. W. Leaver, who supplied me with his unpublished numerical results on the frequencies and damping times of the fundamental $l=m=2$ mode of Kerr black holes, which were necessary for my calculations. This work was supported in part by the National Science Foundation under Grant No. AST85-14911.

[1]W. H. Press, Astrophys. J. Lett. **170**, L105 (1971).
[2]S. A. Teukolsky and W. H. Press, Astrophys. J. **193**, 443 (1974).
[3]S. Chandrasekhar and S. L. Detweiler, Proc. R. Soc. London **A344**, 441 (1975).
[4]S. L. Detweiler, Astrophys. J. **239**, 292 (1980).
[5]E. W. Leaver, Proc. R. Soc. London **A402**, 285 (1986).
[6]S. L. Detweiler, Proc. R. Soc. London **A352**, 381 (1977).
[7]V. Moncrief, C. T. Cunningham, and R. H. Price, in *Sources of Gravitational Radiation*, edited by L. Smarr (Cambridge University Press, Cambridge, England, 1979).
[8]K. S. Thorne, in *300 Years of Gravitation*, edited by S. W. Hawking and W. Israel (Cambridge University Press, Cambridge, England, 1987), p. 330; K. S. Thorne, *Gravitational Radiation: A New Window onto the Universe* (Cambridge University Press, Cambridge, England, in press).
[9]L. A. Wainstein and V. D. Zubakov, *Extraction of Signals from Noise* (Dover, New York, 1962).
[10]E. W. Leaver (private communication).
[11]A. Papoulis, *Probability, Random Variables, and Stochastic Processes* (McGraw-Hill, New York, 1965), Sec. 7-5.
[12]Papoulis, *Probability, Random Variables, and Stochastic Processes* (Ref. 11), Sec. 10-3.
[13]Papoulis, *Probability, Random Variables, and Stochastic Processes* (Ref. 11), Sec. 10-2.
[14]T. Piran and R. F. Stark, in *Dynamical Spacetimes and Numerical Relativity*, edited by J. M. Centrella (Cambridge University Press, Cambridge, England, 1986).
[15]S. Smith, Phys. Rev. D **36**, 2901 (1987).

Addendum to Chapter 2

Recently Finn [1] has developed a new method for extracting black-hole parameters from the output of a noisy detector, and for estimating the uncertainties in the extracted parameters. This new method is more elegant and straightforward than the Wiener optimal-filter method that I developed in the above paper [2], and at first sight it looks rather different from my method. However, as I shall show in this addendum, Finn's method, although more general, is completely equivalent to mine for this class of problems.

Finn's new method is an adaptation of the method of maximum likelihood for parameter estimation, as described in Ref. [3]. Using Finn's notation it can be stated as follows:

Let $m(\mu^0, t)$ be the uncontaminated signal, where μ^0 is the complete set of unknown signal parameters, of cardinality M. Let $n(t)$ be the noise added to the signal by the detector, and $g(t)$ the noisy signal; i.e., $g(t) = m(\mu^0, t) + n(t)$.

Also, let $m(\mu, t)$ be a signal template, which has the same form expected for the signal, but with arbitrary parameter values μ. Then the estimated parameters $\hat{\mu}$ will be those that minimize the "distance" between the measured (contaminated) signal and the template:

$$\langle g - m, g - m \rangle. \tag{2.1}$$

Here the inner product is defined by Finn as

$$\langle a, b \rangle = \int_{-\infty}^{\infty} \tilde{a}(f) \tilde{b}^*(f) S_n^{-1}(f) df, \tag{2.2}$$

where the tilde denotes Fourier transform, the * denotes complex conjugation, $S_n(f)$ is the spectral density of the noise that contaminates the data, and f is the frequency. In the special case of white noise, the spectral density is a constant; therefore, using Parseval's theorem, the inner product can be expressed as

$$\langle a, b \rangle = S_n^{-1} \int_{-\infty}^{\infty} a(t) b(t) dt. \tag{2.3}$$

I will now prove that this method and the Wiener optimal-filtering approach used in my method [2] are one and the same.

The minimization of Eq. (2.1) leads to the following algebraic equations for the estimated parameters $\hat{\mu}$:

$$\langle g - m, m_i \rangle|_{\mu=\hat{\mu}} = 0, \qquad i = 1, \ldots, M\,, \tag{2.4}$$

where

$$m_i \equiv \frac{\partial m(\mu, t)}{\partial \mu_i}. \tag{2.5}$$

Let us now take into account that for any unknown signal the amplitude is one of the unknown parameters that has to be adjusted to minimize the distance (2.1). We can do so by rewriting the template as

$$m(\mu, t) = hK(\tilde{\mu}, t), \tag{2.6}$$

where K is a function of known amplitude, h is the unknown amplitude parameter, and $\tilde{\mu}$ are the other $M - 1$ unknown parameters. (Such a parameter change is always possible.) With this change of parameters, we can re-express the equations (2.4) as

$$\langle g - hK, K_j \rangle \quad = 0 \qquad j = 1, \ldots, M - 1, \tag{2.7}$$

$$\langle g - hK, K \rangle \quad = 0. \tag{2.8}$$

These are algebraic equations for Finn's maximum-likelihood estimates of the parameters h, $\tilde{\mu}_j$. From Eq. (2.8) we obtain the value of h in terms of the other parameters, $\tilde{\mu}_j$.

$$h = \frac{\langle g, K \rangle}{\langle K, K \rangle} \tag{2.9}$$

This value, when replaced in (2.7) gives the following equations for the $\tilde{\mu}_j$:

$$\langle g, K_j \rangle - \frac{\langle g, K \rangle \langle K, K_j \rangle}{\langle K, K \rangle} = 0, \tag{2.10}$$

or equivalently,

$$\frac{\langle g, K_j \rangle}{\langle K, K \rangle^{1/2}} - \frac{\langle g, K \rangle \langle K, K_j \rangle}{\langle K, K \rangle^{3/2}} = 0, \tag{2.11}$$

which is the same as

$$\frac{\partial}{\partial \tilde{\mu}_j}\left(\frac{\langle g, K\rangle}{\langle K, K\rangle^{1/2}}\right) = 0. \tag{2.12}$$

These equations state that one should maximize the ratio of the filtered signal to the output noise, which is precisely my Wiener optimal-filtering method for extracting the black-hole parameters from the noisy signal; see Eq. (3.20) of the above paper (Ref. [2]). We thus conclude that the two methods are exactly equivalent and therefore should produce the same results.

I shall now show explicitly that Finn's formalism does reproduce the same accuracies for the extracted parameters as I obtained in the above paper. I begin with a brief sketch of Finn's [1] derivation of the maximum-likelihood method's error estimate.

Finn denotes the errors in the estimated parameters by $d\mu_i$; i.e.,

$$d\mu_i = \hat{\mu}_i - \mu_i^0 . \tag{2.13}$$

Assuming that these errors are small, Finn expands

$$m(\hat{\mu}, t) = m(\mu^0, t) + m_i(\mu^0, t) d\mu_i, \tag{2.14}$$

and

$$m_i(\hat{\mu}, t) = m_i(\mu^0, t) + m_{ij}(\mu^0, t) d\mu_i, \tag{2.15}$$

which, when replaced in (2.4) and keeping terms only up to first order in $d\mu$, give

$$\langle n, m_k\rangle - \langle m_i, m_k\rangle d\mu_i + \langle n, m_{kj}\rangle d\mu_j = 0. \tag{2.16}$$

Since the third term is an inner product of the noise with the signal, while the second is an inner product of the signal with itself, the the second is larger than the third by a factor of order the amplitude signal-to-noise ratio $\rho = \sqrt{2\langle m, m\rangle}$ (see Ref. [2]), and therefore (because we are assuming that $\rho \gg 1$), the third term can be neglected. [Note that this is equivalent to the neglecting of second-order terms in the noise contribution to the optimal-filter method, in my paper [2], Eqs.(3.14)–(3.18).] Neglecting the third term leads to

$$\langle n, m_i\rangle = \langle m_i, m_j\rangle d\mu_j. \tag{2.17}$$

By inverting this linear equation and then performing an ensemble average to account for the randomness of the noise, Finn [1] obtains the following error estimate:

$$\overline{d\mu_i d\mu_j} = \tfrac{1}{2} A^{-1}_{ij}, \tag{2.18}$$

where

$$A_{ij} \equiv \langle m_i, m_j \rangle. \tag{2.19}$$

Equation (2.18) embodies the uncertainties in the estimated parameters, as well as the correlation between any pair of them.

I shall now show that Finn's error estimate (2.18), when applied to the black-hole ring-down problem, gives precisely the same results as I obtained by my method [2]. The signal parameters, in the notation of Ref. [2], are the black hole's pulsation frequency and damping time, the signal's start time, and the signal amplitude (ω_s, τ_s, t_s, h_s). Among these, the two parameters whose errors and correlation we seek are ω_s and τ_s. The uncertainty and correlations involving the start time t_s and amplitude h_s can be computed equally easily, but we are not interested in them, since they play no role in the uncertainties for the black-hole parameters.

We use the signal $m(\mu, t)$ defined in Ref. [2], Eq. (1.3), for our calculations. By performing the time integrations prescribed by (2.3) to obtain the matrix coefficients A_{ij} defined in (2.19), and then inverting the matrix, we obtain for the coefficients that concern us:

$$A^{-1}_{\omega\omega} = \frac{(1 - 2\,Q_s^2 + 8\,Q_s^4)\;\omega_s^3}{4\,h_s^2\,S_n Q_s^7}, \tag{2.20}$$

$$A^{-1}_{\tau\tau} = \frac{8\;(5 + 4\,Q_s^2)}{h_s^2\,S_n Q_s\,\omega_s}, \tag{2.21}$$

$$A^{-1}_{\omega\tau} = \frac{(3 - 4\,Q_s^2)\;\omega_s}{h_s^2\,S_n Q_s^4}, \tag{2.22}$$

where $Q_s \equiv \frac{1}{2}\omega_s \tau_s$.

With these results, and using (2.18), and the amplitude signal-to-noise ratio

$$\rho = \sqrt{2\langle m, m\rangle} = \sqrt{\frac{4h_s^2 Q_s^3}{S_n(1 + 4Q_s^2)\omega_s}}, \tag{2.23}$$

we can express the fractional uncertainties for the estimates of ω_s and τ_s and their correlation as

$$\begin{aligned}
\frac{\Delta\omega_s}{\omega_s} &= \frac{1}{\rho Q_S}\sqrt{\frac{1-\frac{1}{4}Q_s^{-2}+\frac{1}{8}Q_s^{-4}}{1+\frac{1}{4}Q_s^{-2}}} \simeq \frac{1}{\rho Q_s}\left(1-\tfrac{1}{4}Q_s^{-2}\right) , \\
\frac{\Delta\tau_s}{\tau_s} &= \frac{2}{\rho}\sqrt{\frac{1+\frac{5}{4}Q_s^{-2}}{1+\frac{1}{4}Q_s^{-2}}} \simeq \frac{2}{\rho}\left(1+\tfrac{1}{2}Q_s^{-2}\right) , \\
C_{\omega_s\tau_s} &= -\frac{1}{2Q_s}\frac{1-\frac{3}{4}Q_s^{-2}}{\sqrt{(1+\frac{5}{4}Q_s^{-2})(1-\frac{1}{4}Q_s^{-2}+\frac{1}{8}Q_s^{-4})}} \simeq -\frac{1}{2Q_s}\left(1-\tfrac{5}{4}Q_s^{-2}\right) .
\end{aligned}$$

Here, in the approximate expressions, we neglect corrections of order Q_s^{-4}. Comparing these results with Eq. (3.30) and Table I of Ref. [2], we conclude that as expected, the same results are obtained, including correction terms that correspond exactly to the "correction functions" listed in the table.

Bibliography

[1] S. L. Finn, paper in preparation.

[2] F. Echeverria, Phys. Rev. D **40**(10), 3194 (1989).

[3] L. A. Wainstein and V. D. Zubakov, *Extraction of Signals from Noise* (Dover, New York, 1962).

Chapter 3

Gravitational collapse of an infinite, cylindrical dust shell

Abstract

The evolution of an infinitely long, cylindrical shell of pressureless matter, which collapses because of its own gravitational pull, is studied analytically at late times and numerically for all times. The shell starts from rest and collapses in finite time, as seen by all observers, to form a naked singularity. The singularity is strong in the sense that observers riding on the shell experience, as they reach the singularity, an infinite net stretch parallel to the symmetry axis and an infinite net squeeze in the azimuthal direction. A strong burst of gravitational radiation, which is emitted just before the singularity forms, creates stretches and squeezes in opposite directions to those of the singularity itself: a squeeze along the symmetry axis and a stretch in the azimuthal direction. The numerical analysis gives a complete picture of the shell's motion during the collapse and of the evolution of the spacetime geometry and the emission and propagation of the gravitational wave burst.

1 Introduction

The gravitational collapse of a realistic massive body is not easy to study. The results known so far have been obtained mostly for idealized cases, such as bodies with spherical symmetry. It is hard to obtain results for asymmetric bodies because a full 3+1 numerical simulation of the highly nonlinear Einstein equations is needed to explore their evolution.

An interesting case to study is the collapse of a strongly elongated (prolate), axisymmetric body. This type of collapse could occur in a real astrophysical situation, but it is also interesting in its own right, because (according to recent numerical simulations [1], [2]) it is a possible candidate for violation of the Cosmic Censorship Conjecture [3], and it gives insight into the Hoop Conjecture [4]. (The Cosmic Censorship Conjecture states that no singularity can form without a surrounding horizon; i.e., "naked singularities" are forbidden; the Hoop Conjecture states that black holes with horizons form when and only when a mass M gets compacted into a region whose circumference, in every direction, is $C \lesssim 4\pi M$.)

Studies of prolate collapse require full 2+1-dimensional numerical simulations. However, a simpler approach that can give some insight into the properties of this collapse at late times is the study of an idealized, infinitely long, cylindrical body (1+1 dimensions). The simplest such body is the one analyzed in this paper: a collapsing, cylindrical shell of dust. It may well be that the local behavior of a collapsing, elongated body will be very similar to that of an infinite, cylindrical one.

It has been shown analytically that the collapse of a cylindrical dust shell terminates in a naked singularity [4]. In this paper we shall study in detail how this singularity develops.

It has also been shown recently [5] that if the shell is endowed with any rotation at all, centrifugal forces will halt the collapse at some nonzero, minimum radius, and the shell will then oscillate until it settles down at some final, finite radius.

Therefore, by assuming no rotation whatsoever, our analysis deals with a highly idealized, unrealistic situation. Nevertheless, our analysis may provide information that is useful in guiding and interpreting the much more difficult numerical simulations of collapsing, prolate spheroids.

For example, our analysis reveals the nature and severity of the naked singularity that develops at the end point of the collapse, and this may provide useful insight for future numerical computations, along the lines of Ref. [1], which explore the singularities that appear to develop at the sharp ends of imploding spindles and along the spindles' middles. Our analysis also gives information about the gravitational waves emitted just before the singularity forms, information that may also be of value in the study of collapsing spindles.

The dust shell that we study is idealized as infinitely thin and as having vanishing pressure. These idealizations lead to equations of structure and evolution that are simple enough to admit approximate analytic solutions at late times, and to permit rather tractable numerical simulations at all times.

Our analytic and numerical solutions reveal (not surprisingly) that as the collapse nears its end point, the shell's radial velocity gets closer and closer to the speed of light, and the shell begins to behave as though it were made from "null" dust (i.e., from particles that travel radially at the speed of light). Our approximate analytic solutions treat not only the extreme, late-time, null-dust limit of the collapse, but also the leading departures from null-dust behavior.

Our numerical simulations provide a complete description of the shell's motion and the evolution of the spacetime metric, from the initial moment when the shell is released from rest, until a time very close to the singularity. However, the numerical integration breaks down before the singularity is actually reached. At late times our numerical solution agrees rather well with our approximate analytic solution, if the free parameters of the analytic solution are chosen appropriately.

From the analytic solution, with the numerically determined parameters, it is found that the singularity at the end point of the collapse is strong, in the sense

that the double time integral of the physical components of the Riemann tensor, as measured by an observer riding on the collapsing shell, diverges. In other words, the observer experiences an infinite net stretch and squeeze: a stretch parallel to the symmetry axis; a squeeze azimuthally.

The numerical solution reveals that a sharp burst of gravitational waves is emitted by the shell just before the singularity forms (Fig. 8 below). The waves' strain grows sharply as the retarded time of singularity formation is approached, but it is opposite in sign to the singularity's own strain: As the waves pass distant observers, they squeeze parallel to the symmetry axis and stretch azimuthally. We have no firm proof, but our numerical and analytical solutions strongly suggest that the wave reaches a finite-amplitude peak shortly before the Cauchy horizon, at which the singularity first becomes visible to the outside world. The peak is strong in the sense that the wave's dimensionless strain there is of order unity when the peak passes the radius at which the shell started its collapse.

How this sharply growing stretch and squeeze terminate we cannot say, because the singularity influences them in an unknown way.

This paper is organized as follows:

In Section II we present the basic equations that describe the cylindrical dust shell and its evolution, including the spacetime metric, the wave equations arising from applying Einstein's equations to the metric, the junction conditions across the shell, the boundary and initial conditions, and the equation of motion for the shell.

In Section III we write down and discuss our approximate, late-time analytical solutions of the evolution equations, and we estimate their range of validity.

In Section IV we analyze analytically the evolution of a null shell and compare it with the analytic solutions of Section III.

In Section V we present the results of our numerical simulations and compare them with our analytical solutions.

In Section VI we discuss the results from the previous sections and use them

to infer the properties of the naked singularity.

The Appendix contains a full description of the numerical methods and algorithms used in the computer simulation of the collapse.

2 The governing equations

2.1 Metric for a cylindrical geometry

In a cylindrical spacetime in which the stress-energy tensor satisfies $T_0^0 + T_r^r = 0$, it is possible to introduce a coordinate system in which the metric takes the form [4, 5]:

$$ds^2 = e^{2(\gamma-\psi)}(dr^2 - dt^2) + e^{-2\psi}r^2 d\phi^2 + e^{2\psi}dz^2, \tag{3.1}$$

where ψ and γ are functions of r and t, which satisfy the following restrictions [obtained from applying Einstein's equations to the metric (3.1)]:

$$\psi_{,tt} = \frac{1}{r}(r\psi_{,r})_{,r}, \tag{3.2}$$

$$\gamma_{,r} = r\left[(\psi_{,r})^2 + (\psi_{,t})^2\right], \tag{3.3}$$

$$\gamma_{,t} = 2r\psi_{,r}\psi_{,t}\,. \tag{3.4}$$

Note the remarkably simple form of (3.2), it has exactly the same form as the cylindrical wave equation for a scalar field in flat space. The equations for γ, however, are nonlinear.

2.2 Time coordinates

The condition $T_0^0 + T_r^r = 0$ on the stress-energy tensor can be satisfied only in vacuum or in very special nonvacuum cases, such as null fluids moving toward the axis or away from it. Therefore, we cannot expect to find a global coordinate system covering both the interior and exterior of our collapsing shell, in which the metric takes the form (3.1). Instead, we must use separate coordinate systems of this type in the shell's interior and exterior. We can adjust all the coordinates

of the two systems so that they match at the shell, with the exception of the time coordinate t. Therefore, we will use a t_- coordinate for the interior and a corresponding t_+ for the exterior. This mismatch of coordinate time between the interior and exterior is a severe impediment to finding a full analytical solution for the evolution of the fields ψ and γ, and the motion of the shell. Therefore, a numerical solution becomes necessary for a full understanding of the collapse.

Henceforth in this paper, the "$-$" and "$+$" subscripts will be used on variables to indicate that they are to be evaluated on the inner or outer face of the shell, respectively.

The interior and exterior time coordinates, $t_\mp$ are related to the proper time τ measured by an observer moving with the shell, by

$$dt_\pm/d\tau = X_\pm. \tag{3.5}$$

Here $X_\pm$ are defined by

$$X_\pm \equiv \left[e^{-2(\gamma_\pm - \psi)} + V^2\right]^{1/2}, \tag{3.6}$$

where the variables must be evaluated on the shell, i.e., at $r = R(\tau)$, and $V \equiv dR/d\tau$.

2.3 Equation of motion and boundary conditions

We shall denote by λ the shell's *conserved* rest mass per unit z-coordinate length. As discussed below, the shell collapses from rest, and we adjust the z coordinate so that it coincides with proper length on the shell in the initial, static state. Therefore, λ is equal, numerically, to the shell's initial rest mass per unit proper length. An argument given in Ref. [5] shows that if λ exceeds $1/4$, the shell's mass is so great that it closes up space radially around itself. To avoid this, we shall restrict attention to shells with mass per unit length $\lambda < 1/4$.

Reference [5] analyzes the structure and evolution of a cylindrical dust shell in which half the particles are rotating around the symmetry axis in a right-handed

fashion and half in a left-handed fashion, with angular momentum per unit rest mass α. The dust shell analyzed in this paper is identical to that of Ref. [5], but with no rotation, i.e., with $\alpha = 0$.

The equation of motion for our collapsing shell, as obtained from [5] with $\alpha = 0$, is

$$\begin{aligned} A \equiv & \quad \frac{d^2R}{d\tau^2} \\ = & \quad -\frac{\lambda X_-}{R} - R\left[(X_-^2 + V^2)(\dot{\psi}_-^2 + \psi_-'^2) + 4X_- V\dot{\psi}_-\psi_-'\right] \\ & +(X_-^2 + V^2)\psi_-' + 2X_- V\dot{\psi}_-. \end{aligned} \tag{3.7}$$

Here and below, each dot represents a partial derivative with respect to coordinate time (in this case t_-, since all derivatives are in the interior), and the prime represents a partial derivative with respect to the radial coordinate r.

The junction conditions arising from the jump in intrinsic curvature across the shell can be expressed as [5]

$$X_+ - X_- = -4\lambda \tag{3.8}$$

and

$$\psi_{+,n} - \psi_{-,n} = -2\lambda/R, \tag{3.9}$$

where the derivatives (denoted "$_{,n}$") are taken along the direction normal to the shell in the shell's rest frame, which means that $\psi_{+,n} = V\dot{\psi}_+ + X_+\psi_+'$ and similarly for $\psi_{-,n}$.

The requirement of integrability of (3.2) in the interior of the shell imposes the conditions

$$\psi(r = 0, t_-) \quad \text{finite}, \tag{3.10}$$

$$\psi'(r = 0, t_-) = 0. \tag{3.11}$$

In addition, ψ has to be continuous across the shell:

$$\psi_-(\tau) = \psi_+(\tau). \tag{3.12}$$

Equations (3.9) and (3.12) can be rewritten in a more computationally useful form, in terms of radial and time derivatives of ψ, as follows:

$$(X_+\dot{\psi}_+ + V\psi'_+) - (X_-\dot{\psi}_- + V\psi'_-) = 0, \tag{3.13}$$

$$(V\dot{\psi}_+ + X_+\psi'_+) - (V\dot{\psi}_- + X_-\psi'_-) = -\frac{2\lambda}{R}. \tag{3.14}$$

Requiring that spacetime be locally flat on the axis implies the condition

$$\gamma(r = 0, t_-) = 0. \tag{3.15}$$

We have chosen to study the collapse of a shell that has been at rest until $t_- = t_+ = \tau = 0$, the instant at which the collapse is allowed to start. The only length scale in the problem is the shell's initial radial coordinate R_0. We shall use this initial radius as our unit of length (i.e., we shall measure r, t, and z in terms of it); and by doing so we, in effect, are setting $R_0 = 1$.

The shell's initial, static state is described by the following static solution of the Einstein equations [5]:

$$\psi = \begin{cases} 0 & \text{for } r < R_0 = 1, \\ -\frac{2\lambda}{1-4\lambda} \ln r & \text{for } r > R_0 = 1, \end{cases} \tag{3.16}$$

$$\dot{\psi} = 0 \qquad \text{everywhere}, \tag{3.17}$$

and

$$\gamma = \begin{cases} 0 & \text{for } r < R_0 = 1, \\ \left(\frac{2\lambda}{1-4\lambda}\right)^2 \ln r - \ln|1-4\lambda| & \text{for } r > R_0 = 1. \end{cases} \tag{3.18}$$

Since gravitational waves cannot travel faster than the speed of light, ψ will satisfy

$$\psi(r, t_+) = -\frac{2\lambda}{1-4\lambda} \ln r, \qquad \text{for } r > t_+ + 1. \tag{3.19}$$

This solution for ψ will serve as an outer boundary condition for our numerical computations and will permit us to confine our computations to the region $r < t_+ + 1$.

3 Late-time analytical solution

As we have seen, a full analytic solution for the whole evolution of the collapse does not seem possible. However, by restricting ourselves to the collapse's late stages, when it is close to the final singularity, we can find a class of approximate solutions that depend on a set of unknown parameters, and we can then fix the parameters by matching to our numerical simulation.

In our approximate solutions we shall use as our time coordinate the "time to collapse" $\bar{t} \equiv t_{c-} - t_-$; here t_{c-} is the value of the interior time coordinate t_- at the end point of the collapse.

We are interested in the behavior of the system for $\bar{t} \ll 1$. At late times it is reasonable to expect the shell to be moving at nearly the speed of light, i.e., along the curve $r = \bar{t}$, and correspondingly we expect that the r-dependence of ψ inside and near the shell will have a characteristic length scale of $\bar{t}$. This suggests that $\psi(r, \bar{t})$ may approach a similarity solution that can be expressed as simple functions of $r/\bar{t}$ and $\bar{t}$. Using this ansatz, one arrives at the following late-time solution for ψ in the shell's interior [6]:

$$\psi(r, \bar{t}) = \alpha \ln^{\beta}(\Omega/\bar{t}) + (\alpha\beta/2) \ln^{\beta-1}(\Omega/\bar{t}) F(r/\bar{t}). \tag{3.20}$$

Here α, β, and Ω are constants that depend on the early-time evolution, which in turn depends on the initial conditions, and

$$F(x) = \ln 4 - \ln \left| x^2 \left(\frac{1 + \sqrt{1 - x^2}}{1 - \sqrt{1 - x^2}} \right) \right|. \tag{3.21}$$

[This is an asymptotic solution of the wave equation (3.2), valid only for the late-time evolution of ψ.]

Inserting this solution for ψ into (3.3), and assuming that $\bar{t}$ is small enough that $\ln(\Omega/\bar{t}) \gg 1$, we obtain, for γ, the simple expression

$$\gamma(r, \bar{t}) = \alpha^2 \beta^2 \ln^{2(\beta-1)}(\Omega/\bar{t}) \left[-\ln(1 - x^2) - F(x) \right], \tag{3.22}$$

where $x \equiv r/\bar{t}$. It can also be shown that (3.20) satisfies the wave equation (3.2). Next, from the equation of motion, and assuming that $\alpha \sim 1$, $\ln^{\beta}(\Omega/\bar{t}) \gg 1$, and

$\ln^{1-\beta}(\Omega/\bar{t}) \gg 1$ (as will turn out to be true when we match to our numerical simulation), we find that

$$R/\bar{t} = 1 - e^{-2\alpha \ln^{\beta}(\Omega/\bar{t})}. \tag{3.23}$$

Using this result to evaluate ψ and γ on the shell we obtain

$$\psi_s(\bar{t}) = \alpha \ln^{\beta}(\Omega/\bar{t}), \tag{3.24}$$

$$\gamma_-(\bar{t}) = 2\alpha^3\beta^2 \ln^{3\beta-2}(\Omega/\bar{t}), \tag{3.25}$$

which implies that only for $0 < \beta < 2/3$ does γ_- goes to zero as $\bar{t} \to 0$. (We will see in the following section why this is necessary; and in Sec. V, when we match to our numerical simulation, we will see that β does indeed lie in this range.)

Using (3.23), plus the definitions $V = dR/d\tau$ and (3.6), we obtain the additional asymptotic expressions

$$X_- = -V \quad = (1/\sqrt{2\sigma})e^{2\alpha \ln^{\beta}(\Omega/\bar{t})}, \tag{3.26}$$

$$X_- + V \quad = \sqrt{\sigma/2}, \tag{3.27}$$

where σ, like α, β, and Ω is a constant to be determined by matching to the numerical simulation. Finally, using the above relations plus Equations (3.6) and (3.8), we obtain for the jump in γ across the shell, assuming $\gamma_- \to 0$ at the singularity,

$$\gamma_+ - \gamma_- \to -\frac{1}{2}\ln(1 - 8\lambda/\sqrt{2\sigma}). \tag{3.28}$$

How late in the collapse will the approximate solutions (3.20)–(3.28) to the collapse equations be valid? The conditions we had to impose to be able to obtain these simple solutions, namely,

$$\ln^{\beta}(\Omega/\bar{t}) \gg 1, \qquad \ln^{1-\beta}(\Omega/\bar{t}) \gg 1, \tag{3.29}$$

along with the constraint $\beta < 2/3$, imply that if $\Omega \sim 1$ (as will turn out to be the case), these results will be valid only for $\bar{t} \lesssim 10^{-10}$ — which means very late times indeed. Thus, in order to match the above solutions to our numerical simulations and determine the unknown parameters α, β, Ω, and σ, we will have to evolve our simulations until the shell is extremely close to the end of the collapse.

4 The null-shell limiting case

As the cylindrical shell nears the end point of its collapse, it will asymptotically approach the behavior of a null shell, that is, one made of a null fluid, which moves along radial, lightlike geodesics. To gain insight into the consequences of this, we shall briefly review some features of imploding null-fluid cylinders, as developed in Ref. [7].

The stress-energy tensor for an imploding, cylindrical shell of null fluid has as its only nonzero components

$$T_{rr} = -T_{tt} = \frac{A(u)}{2\pi r}, \tag{3.30}$$

where $u = (1/\sqrt{2})(t + r)$ and $A(u)$ is an arbitrary function that describes the radial profile of the shell's energy density. This stress-energy tensor satisfies the condition $T^r_r + T^t_t = 0$, which implies (as we mentioned in Sec. II) that one can find a single, global coordinate system, valid across the shell, in which the metric has the form (3.1).

Let us look at the behavior of the null shell during its inward radial motion. Since we can find a globally valid coordinate system that satisfies (3.1), the evolution equation for ψ, Eq. (3.2), is valid everywhere, which means that the evolution of ψ is completely decoupled from the motion of the null shell [7].

If no gravitational waves are present in the initial data (i.e., if ψ vanishes initially), then ψ will vanish everywhere, and the solution for γ will be determined by [7]

$$\gamma_{,u} = 4\sqrt{2}A(u), \qquad \gamma_{,v} = 0, \qquad \gamma(r = 0) = 0, \tag{3.31}$$

where $u = (1/\sqrt{2})(t + r)$, and $v = (1/\sqrt{2})(t - r)$. This means that γ will be identically zero in the interior of our shell of null fluid, and will abruptly jump to a constant value outside the shell, since $A(u)$ is zero everywhere except on the shell.

How do these results relate to our timelike dust shell? As our collapsing shell approaches the axis, it should gradually and asymptotically begin to behave like a

null shell. This implies that ψ should become asymptotically decoupled from the shell, and its evolution should gradually become more and more dominated by the field that was laid down in the early part of the collapse. Moreover, the interior and exterior coordinate systems should asymptotically mesh together into a global one.

We can verify that this is indeed the case for the timelike shell at very late times, by proving that the radial and time derivatives of ψ on both sides of the shell, though different during the early evolution, get closer and closer as the collapse nears its end, and by proving that the fractional difference between $X_+ = dt_+/d\tau$ and $X_- = dt_-/d\tau$ goes to zero.

From the junction condition (3.8) and the asymptotic form (3.26) of X_-, it is clear that the fractional difference between X_+ and X_- does asymptote to zero, as claimed. In the junction conditions (3.13), (3.14), it is easy to see that for late times, the λ-dependent term becomes negligible compared to the other terms. Then, using the results (3.26) from the preceding section for $X_\pm$, V , the derivatives on the exterior side of the shell can be expressed in terms of those on the interior side as

$$\dot{\psi}_+ = (1+\kappa)\dot{\psi}_- + \kappa\psi'_-, \tag{3.32}$$

$$\psi'_+ = \kappa\dot{\psi}_- + (1+\kappa)\psi'_-, \tag{3.33}$$

$$\kappa \equiv \frac{2\lambda}{1-4\lambda}. \tag{3.34}$$

These expression and the constancy of λ would seem to imply that the derivatives on the two sides are always different. However, from (3.24) and (3.23), it can be seen that $\dot{\psi}_-$ and ψ'_- asymptote to the same absolute value, with opposite signs:

$$\psi'_- = -\dot{\psi}_- = \frac{\alpha\beta}{2\bar{t}}\ln^{\beta-1}(\Omega/\bar{t})e^{\alpha\ln^\beta(\Omega/\bar{t})}, \tag{3.35}$$

$$\psi'_- + \dot{\psi}_- = -\frac{\alpha\beta}{2\bar{t}}\ln^{\beta-1}(\Omega/\bar{t}). \tag{3.36}$$

This means that the κ-dependent terms in (3.32) and (3.33) become negligible compared to the remaining term, therefore implying that $\dot{\psi}_+/\dot{\psi}_- \to 1$, $\psi'_+/\psi'_- \to 1$,

as claimed.

In the next section we will see strong evidence that the gravitational waves emitted by our collapsing, timelike shell reach a nondivergent peak amplitude shortly before the singularity forms. The apparent lack of divergence may well be related to the asymptotic decoupling of ψ from the shell, but we are not certain of this.

There is no question that our timelike shell forms a singularity at the end point of its collapse (Ref. [4] and Sec. VI of this paper). However, Morgan [7] shows that for a null shell *no* singularity (not even a conical one) develops, in the absence of gravitational waves ($\psi \equiv 0$). That is, if one imposes the condition that ψ and its time derivatives vanish at past infinity, which means that ψ will always be zero (since its evolution is completely decoupled from the shell's evolution), then the shell collapse and the evolution of γ will lead the pulse to pass through the axis and back out, with no singularity formed.

We suspect that the reason that our timelike shell, unlike a precisely null one, is able to form a singularity is that our shell never gets fully decoupled from the ψ field, but only asymptotically decoupled; however, we are not certain that this is the reason.

We have tried to produce a complete mapping between the asymptotic evolution of our timelike shell at late times and that of a null shell, but we were not fully successful. Our failure may be related to the fact that when dust particles with nonzero rest mass are boosted to the speed of light, their 4-momenta diverge, but the 4-momentum of any small patch of a truly null shell is finite.

5 Numerical simulation

We have developed a numerical simulation of the shell's collapse, and have followed its evolution and that of the gravitational waves it emits. (For a description of the numerical methods used, see the Appendix.)

It is easy to follow the evolution of the shell until it is close enough to the singularity to determine, to a fraction of a percent accuracy, the total collapse time. For a rest mass per unit length $\lambda = 0.1$, the collapse times in units of the initial radius (which we have set to unity in our formulas) are:

$$\tau_c = 3.76, \qquad t_{c-} = 4.26, \qquad t_{c+} = 2.76. \tag{3.37}$$

Figure 1 shows how the collapse times vary as a function of λ. Also plotted is the collapse time predicted by Newtonian physics,

$$\tau_N = (2\lambda)^{-1/2} \int_0^1 [-\ln(1-x)]^{-1/2} dx = 1.2533\lambda^{-1/2}. \tag{3.38}$$

As one might expect, the smaller the shell's mass per unit length, the smaller the difference between the proper time and the two coordinate times, and the closer they are to the Newtonian time, but for the highly relativistic case (large λ), the various times differ considerably. Notice also that for all cases, the proper time for the collapse τ_c is smaller than the Newtonian time τ_N. This might not seem too surprising, since it is also true for a collapsing spherical shell that $\tau_c > \tau_N$ (see Ref. [8]); however, in the cylindrical case there are gravitational waves that are not present in the spherical case, so it was far from obvious in advance that the collapse times would behave similarly.

We were able to follow the collapse until $\bar{t} \sim 10^{-12}$, which is very close to the singularity and is adequate for matching to our analytic solution, though just barely; see the last paragraph of Sec. III. Soon after $\bar{t} \sim 10^{-12}$, the simulation started to break down. As a control for the accuracy of the simulation, we used the fact that the integral of $\nabla\gamma$ around a spacetime loop outside the shell should vanish. We evaluated this integral for a loop that has its bottom leg on the initial constant-time slice, its top leg on the constant-time slice for the current integration time, its left side along a curve parallel to the shell's world line and just a few grid points outside it, and its right side on a segment of the outer limit of integration. We regarded the simulation as no longer reliable when the integral

around this loop became larger than a few percent of the difference in γ between the shell and the outer boundary. This loss of reliability was usually followed by a complete breakdown of the simulation, typically as a result of not being able to solve Equation (3.56), which arises from the junction conditions on the shell.

In our numerical simulations, ψ in the interior of the shell always became very uniform (independent of r) quite rapidly, but with its near-constant value increasing with time. This agrees with the analytical solution (3.20), for which the r-dependent term becomes less and less important as $\bar{t}$ approaches zero.

For ψ in the exterior, the numerical evolution was a little more interesting. Figure 2 shows the evolution for a shell with mass per unit length $\lambda = 0.1$, which is fairly relativistic. (Recall that $\lambda = 0.25$ is sufficient to begin to close space up radially.) The envelope in the figure represents the value ψ_s of ψ on the shell.

In our late-time analytic solutions (Sec. III), there are several relationships that are independent of the (as yet) unknown constants α, β, Ω, and σ. Figures 3 and 4 show two such relationships as predicted by the approximate analytic solutions and as produced by our numerical simulation for $\lambda = 0.1$. The agreement between the analytic and numerical solutions is reasonably good.

Figures 5 and 6 depict quantities, $X_- + V$ and $\gamma_+ - \gamma_-$, that are predicted by our analytic solutions to approach constants that depend only on the unknown parameter σ. The numerical solutions do indeed seem to be approaching constants, and the numerical values of both constants agree very well with the analytical values if σ has the value 1.186.

Figure 7 plots the numerical results for ψ on the shell as a function of the "time-to-collapse" $\bar{t}$, and also the analytical result (3.24) for the best-fit values of the parameters, $\alpha = 0.3262$, $\beta = 0.4999$, and $\Omega = 1.009$. The least-squares method used for the parameter fit turned out to have a very sharp dip around these values, giving very precise results, especially for β and Ω (precision much better than 1 percent). These best-fit values strongly suggest that β and Ω have exact values of $1/2$ and 1, respectively, and therefore only α and σ really depend on

the initial conditions. Note that for these values of the parameters, the numerical and analytical results coincide fairly well at late times.

The final piece of information obtained from our numerical analysis is the gravitational waves (the ripples in ψ) emitted by the collapsing shell just before it creates the singularity. To compute the waves, we start from the numerical results obtained for $\psi(r)$ at a time very close to the singularity (Fig. 2). Then, after subtracting the static solution [Eq. (3.16) extended down to the shell's radius at that time], we evolve ψ analytically, using its wave equation (3.2). Let t_0 be the value of t_+ at the moment we start this analytical evolution. Then for any later time $\delta\psi \equiv \psi - \psi_{static}$ will be given by

$$\delta\psi(r,t) = \int dk J_0(kr)[A(k)\cos k(t_+ - t_0) + B(k)\sin k(t_+ - t_0)], \tag{3.39}$$

where, assuming $R(t_0) \ll 1$, the functions $A(k)$ and $B(k)$ are given by

$$A(k) = k\int_{R(t_0)}^{\infty} rJ_0(kr)\delta\psi(r,t_0)dr, \tag{3.40}$$

$$B(k) = \int_{R(t_0)}^{\infty} rJ_0(kr)\delta\psi_{,t_+}(r,t_0)dr. \tag{3.41}$$

Of course, this waveform is valid only at radii r that are outside the domain of influence of the singularity; i.e., it is valid only for $r > R(t_0) + t_+ - t_0$; and the waveform will vanish outside the domain of influence of the shell's initial location, i.e., at $r > 1 + t_+$.

The waveform $\delta\psi(t_+, r)$ was computed by numerical integration of Eqs. (3.39)–(3.41), using for $\delta\psi$ and $\delta\psi_{,t_+}$ at time t_0, the results of our numerical simulation. The resulting waves are shown in Fig. 8.

Because the waves have $\delta\psi$ negative, they stretch objects along the azimuthal (ϕ) direction and squeeze objects parallel to the symmetry axis (z direction); cf. Eq. (3.1). As we shall see in the next section, these directions of stretch and squeeze are opposite to those produced by the singularity.

Notice that, as one would expect from geometric optics and energy conservation, once the waves have propagated to radii r large compared to the wavelengths

they contain, the shape of the waveform ceases to change, and its amplitude dies out thereafter as $1/\sqrt{r}$ (see Fig. 9).

One might have expected the peak amplitude of the gravitational waves to grow higher and higher, without bound, as the time slice on which we start our wave-evolution calculation gets closer and closer to the end point of collapse. This seems not to be the case. We found essentially the same gravitational wave pulse, with the same peak amplitude at late times, independently of whether we initiated the pulse's evolution at $t_0 = t_{+c} - 10^{-4}$ or $t_{+c} - 10^{-8}$ or $t_{+c} - 10^{-12}$. Moreover, when we initiated the evolution at very late values of t_0, there actually seemed to be a rounded peak in the initial data rather than a monotonic peak (see the leftmost curve in Fig. 9). [This is not terribly surprising, since our analytic solution for ψ_s, the value of ψ on the shell, has the property that $\delta\psi_s\sqrt{R/r}$ goes to zero, for fixed r, in the limit as the shell approaches the singularity ($\bar{t} \to 0$ and $R \to 0$), which means that if the waves from the shell's location itself, at the end point of collapse, were to propagate along the Cauchy horizon in a geometric optics manner, their amplitude at any finite r would be zero.] We regard this as strong evidence that one will see the waves as having a finite, nonsingular behavior as one approaches the Cauchy horizon (the location at which one first feels the influence of the singularity).

6 Tidal forces at the singularity

We have found that as was expected, the shell collapses to form a singularity in finite proper time.

It is interesting to study the properties of the singularity. One way to do this is to determine the tidal forces and deformations experienced by an observer who rides on the collapsing shell. The tidal forces are embodied in the equation for the relative gravitational acceleration of two parts of the observer's body that have a

separation vector $\xi^{\hat{k}}$ [9]

$$\frac{D^2\xi^{\hat{j}}}{D\tau^2} = R^{\hat{\tau}}{}_{\hat{j}\hat{\tau}\hat{k}}\xi^{\hat{k}}. \tag{3.42}$$

Here and below, the hats denote components as measured in an orthonormal frame carried by the observer. As we shall see, the components of the Riemann curvature tensor that enter into this tidal-force equation diverge as the collapse reaches its end point, and correspondingly, the observer on the shell gets infinitely stretched and squeezed.

One criterion for the severity of the singularity is the total deformation (the total strain) that the observer experiences. This deformation is given by the double time integral

$$\int d\tau \int d\tau' R^{\hat{\tau}}{}_{\hat{j}\hat{\tau}\hat{k}}. \tag{3.43}$$

If this quantity diverges, then the net deformation that the observer experiences, by the time he reaches the singularity, is infinite; that is what happens, e.g., as seen by an observer falling into the singularity at the center of a Schwarzschild black hole. [9]. If the double time integral does not diverge, then, even though the tidal force becomes infinite, there is not enough time before the singularity is reached for the observer to become infinitely deformed. This type of "whimper" singularity is what occurs at the center of a realistic, old, Kerr black hole, according to classical, general-relativistic perturbation calculations [10].

One can show from the approximate analytic solution of Sec. II that as expected, the Riemann curvature tensor does diverge at the end point of the collapse. This, of course, is an explicit proof that the collapse produces a singularity, as expected. It follows from the form of the line element (3.1) and the forms of our analytic and numerical solutions that the singularity is naked. (For a more rigorous and complete proof of its nakedness, see Ref. [4].)

In order to study the nature of the singularity for our cylindrical shell, we would like to compute the Riemann tensor components in (3.43) on the outside face of the shell. However, as we showed in Sec. IV, for times very close to the final collapse

time, the shell behaves more and more like a lightlike shell, and the distinction between the inside and the outside vanishes (for example, the derivatives of ψ asymptote to the same value on both sides of the shell). Therefore, we expect the Riemann tensor on the outside face of the shell to be the same, asymptotically, as on the inside face; and we can compute it on the inside face rather easily, using the analytic formulae that we obtained for the shell's interior in Sec. III.

We find, from such a calculation, that on the shell's inside face, the only nonzero components of the Riemann tensor as measured by an observer riding on the shell are

$$R^{\hat{\tau}}{}_{\hat{z}\hat{\tau}\hat{z}} = -R^{\hat{\tau}}{}_{\hat{\phi}\hat{\tau}\hat{\phi}} = (V^2 + X_-^2)\psi_-'' + 2VX_-\dot{\psi}_- \sim \frac{1}{\bar{t}^2}\ln^{\beta-1}(\Omega/\bar{t})e^{7\psi_s}. \qquad (3.44)$$

Recall that our numerical results strongly suggest that $\Omega = 1$ and $\beta = 1/2$, and recall that $\psi_s = \alpha\ln^{\beta}(\Omega/\bar{t})$, where a tiny correction has been neglected and where $\alpha = 0.3262$ when $\lambda = 0.1$). Thus, the Riemann tensor diverges slightly more rapidly than $1/\bar{t}^2$. From $d\bar{t}/d\tau = X_- = (2\sigma)^{-1/2}e^{2\psi_s}$ we infer that at late times, the proper time to collapse, $\bar{\tau} \equiv \tau_c - \tau$, and the inner coordinate time to collapse, $\bar{t}$, are related by $\bar{\tau} = \sqrt{2\sigma}\bar{t}e^{-2\alpha\ln^{\beta}(\Omega/\bar{t})} = \sqrt{2\sigma}\bar{t}e^{-2\psi_s}$; and correspondingly, the Riemann tensor as a function of proper time also diverges slightly more rapidly than $1/\bar{\tau}^2$. This means in turn that the double time integral of the Riemann tensor, Eq. (3.43), diverges slightly more rapidly than $\ln\tau$. This and the signs in Eq. (3.44) mean that the observer riding on the shell will experience no deformation radially, but will be stretched infinitely in the $\hat{z}$ direction, i.e., parallel to the symmetry axis, and will be squeezed infinitely in the $\hat{\phi}$ direction, i.e., the azimuthal direction.

7 Acknowledgments

I would like to thank Kip Thorne for introducing me to this problem, for supplying me with his unpublished results on the subject, and for his constant encouragement that led to the completion of this paper.

I would also like to thank Charles "Chuck" Evans, who introduced me to some of the secrets of the integration of partial differential equations.

This paper was supported in part by the National Science Foundation Grants AST-8817792 and AST-9114925.

8 Appendix: Description of the numerical method

The main problem faced when we try to perform a numerical simulation of the collapse of the cylindrical dust shell is that it is necessary to deal with two different time coordinates, one for the interior and a different one for the exterior. This makes it very hard to use methods that require a fixed ratio between time step and spatial step, since such methods would lead to two sets of constant-time slices, one for the interior and one for the exterior, which will not match at the shell.

A second impediment to the simulation is that the location at which the two coordinate systems meet (the shell's location) moves with time, and this makes it hard to apply the junction conditions,

In order to solve both problems we have used, at each step, a pair of slices: one with constant t_- in the interior, and one with constant t_+ in the exterior, at times chosen so that the slices match on the shell; and we have used an adaptive mesh to follow the evolution of the shell.

The adaptive mesh allows us to have a constant number of grid points in the interior and exterior parts of the slice, and it has the advantage of always keeping the same grid point on the shell (actually two points, one just inside and one just outside it), thus making it easier to apply the junction conditions. (See Figure 10.)

This choice of grid leads to a shrinking of the interior spatial step, and a stretching of the exterior spatial step as time passes. We chose to use evenly spaced points on the interior, while on the exterior slice the points right outside the shell start with a separation matching that of the interior points, but their separation increases (by a constant factor very close to unity) as they approach

the outer limit of integration. This arrangement allows us to deal properly with the increasingly fine detail inside the shell and in the near zone outside the shell.

This shrinking of the spatial step implies that we also have to keep reducing the time step proportionally at each iteration, in order to maintain the $\Delta t/\Delta r$ ratio smaller than unity, to satisfy the Courant condition and to avoid numerical instability [11].

In addition to the slices where ψ was computed, we used another set of slices, each of which falls betweeen two consecutive ψ-slices (see Fig. 11). On this alternating set of slices, we computed the values of $\xi \equiv \psi_{,t}$. In this way we can solve the following set of two first-order equations:

$$\left(\frac{\partial\psi}{\partial t}\right)_{g.p.} = \xi + v\psi_{,r}, \tag{3.45}$$

$$\left(\frac{\partial\xi}{\partial t}\right)_{g.p.} = \frac{1}{r}(r\psi_{,r})_{,r} + v\xi_{,r}, \tag{3.46}$$

where the subscript "$g.p.$" means that the time derivatives are taken at fixed grid point, not fixed r. Here $v = \partial r/\partial t$ is the speed of the grid points, and the second terms in both equations arise from the fact that these points are moving.

The difference equations used for the numerical evolution were an implementation of the Lax-Wendroff method [11]. Briefly, this method uses 3 points on one slice to compute 2 points on an intermediate slice, and then uses these plus one of the initial 3 points to compute one point on the next slice (see Fig. 11). When applied to Equation (3.45) the difference equations for ψ turn out to be

$$\psi^{n+\frac{1}{2}}_{j+\frac{1}{2}} = \tfrac{1}{2}\left(\psi^n_j + \psi^n_{j+1}\right) + \tfrac{1}{2}xi^{n+\frac{1}{4}}_{j+\frac{1}{2}}\Delta t^n + v^{n+\frac{1}{4}}_{j+\frac{1}{2}}\frac{\Delta t^n}{2\Delta r_j}\left(\psi^n_{j+1} - \psi^n_j\right), \tag{3.47}$$

$$\psi^{n+1}_j = \psi^n_j + \Delta t^n \xi^{n+\frac{1}{2}}_j + v^{n+\frac{1}{2}}_j \frac{\Delta t^n}{\Delta r_{j-\frac{1}{2}}}\left(\psi^{n+\frac{1}{2}}_{j+\frac{1}{2}} - \psi^{n+\frac{1}{2}}_{j-\frac{1}{2}}\right), \tag{3.48}$$

where (3.47) gives the result for one of the intermediate (Lax) steps (the other one is obtained from an analogous formula, but with j replaced by $j-1$ everywhere), and (3.48) gives the value on the next slice ("staggered-leapfrog" step).

In the above equations the superscript corresponds to the time slice where the value resides (with integer n corresponding to the ψ-slices), and the subscript

indicates the spatial location on the slice (with integer j corresponding to the grid points).

Similarly, applying the Lax-Wendroff method to Eq. (3.46), we obtain for ξ:

$$\begin{aligned}
\xi^n_{j+\frac{1}{2}} = \quad & \tfrac{1}{2}\left(\xi^{n-\frac{1}{2}}_{j+1} + \xi^{n-\frac{1}{2}}_{j}\right) + \frac{\Delta t^n}{2\Delta r_j} v^{n-\frac{1}{2}}_{j+\frac{1}{2}} \left(\xi^{n-\frac{1}{2}}_{j+1} - \xi^{n-\frac{1}{2}}_{j}\right) \\
& + \frac{\Delta t^n}{2 r_{j+\frac{1}{2}} (\Delta r_j)^2} \times \\
& \left[r_{j+1}\left(\psi^{n-\frac{1}{4}}_{j+\frac{3}{2}} - \psi^{n-\frac{1}{4}}_{j+\frac{1}{2}}\right) - r_j \left(\psi^{n-\frac{1}{4}}_{j+\frac{1}{2}} - \psi^{n-\frac{1}{4}}_{j-\frac{1}{2}}\right)\right], \qquad (3.49) \\
\xi^{n+\frac{1}{2}}_{j} = \quad & \xi^{n-\frac{1}{2}}_{j} + \frac{\Delta t^n}{\Delta r_j} v^n_j \left(\xi^n_{j+\frac{1}{2}} - \xi^n_{j-\frac{1}{2}}\right) \\
& + \frac{\Delta t^n}{r_j (\Delta r_j)^2} \left[r_{j+\frac{1}{2}} \left(\psi^n_{j+1} - \psi^n_j\right) - r_{j-\frac{1}{2}} \left(\psi^n_j - \psi^n_{j-1}\right)\right], \qquad (3.50)
\end{aligned}$$

where, again, (3.49) results from one of the intermediate Lax steps (and the other one is obtained by replacing $j \to j-1$), and (3.50) results from the final staggered-leapfrog step.

These equations allow us to evolve ψ in vacuum. But we also need to apply boundary conditions. First, on the axis, we know from Eq. (3.11) that the radial derivative of ψ vanishes. In addition, we cannot have grid points right on the axis, since Eq. (3.50) involves a division by the value of r at the grid point. Therefore, we use a first grid point at half the size of a radial step from the axis ($j = 0$), and another "mirror" point ($j = -1$) on the "opposite side" of the axis, and use $\psi(r_{-1}) = \psi(r_0)$ (see Fig. 11).

Next, there is the issue of the outer boundary. Since we are mostly interested in the evolution that occurs during the collapse — and this lasts a finite amount of time — there is a radial limit past which no information from the collapse will have arrived at the end of the collapse. Therefore, it is enough to choose an outer limit of integration bigger than this limit.

Finally, we have to to deal with the junction conditions on the shell [Eqs. (3.13) and (3.14)]. For this, we used the method of characteristics [12]. Briefly, this is a method to evolve numerically a partial differential equation from one slice to the next by computing the value on one grid point by integrating along

the "characteristic" curves that cross that point, starting with the values on the previous slice. In our case the characteristics are the two diagonal lightlike lines ($dr = \pm dt$) that cross the slice at the given point.

This allows us to express the values of the variables (ψ and derivatives) on the grid point that lies on the shell as functions of the known values close to the shell in the previous slice, and this in turn leads to an equation that can be solved for ψ on the shell.

More specifically, from Fig. 12 and the equations for propagation along the characteristics [12], we obtain

$$d\psi'_- - d\dot{\psi}_- + \frac{1}{r}\psi'_- dt_- \quad = 0, \tag{3.51}$$

$$-d\psi'_+ - d\dot{\psi}_+ + \frac{1}{r}\psi'_+ dt_+ \quad = 0; \tag{3.52}$$

and correspondingly, we obtain, by applying a first-order approximation to the triangle PQR in the figure:

$$(\psi'_{R-} - \psi'_{P-}) - (\dot{\psi}_{R-} - \dot{\psi}_{P-}) + \frac{1}{2r}(\psi'_{R-} + \psi'_{P-})(t^R_- - t^P_-) \quad = 0, \tag{3.53}$$

$$-(\psi'_{R+} - \psi'_{Q+}) - (\dot{\psi}_{R+} - \dot{\psi}_{Q+}) + \frac{1}{2r}(\psi'_{R+} + \psi'_{Q+})(t^R_+ - t^Q_+) \quad = 0. \tag{3.54}$$

These equations plus those arising from the junction conditions [Eqs. (3.13) and (3.14)], evaluated at point R, allow us to obtain expressions for the radial and time derivatives of ψ at point R on the inside and the outside of the shell (ψ'_{R-}, ψ'_{R+}, $\dot{\psi}_{R-}$, $\dot{\psi}_{R+}$). Finally, using the evolution equation for ψ along, say, $\overline{PR}$

$$d\psi = \psi'_- dr + \dot{\psi}_- dt_-, \tag{3.55}$$

we obtain the following expression for ψ_R:

$$\psi_R = \psi_P + \tfrac{1}{2}(\psi'_{P-} + \psi'_{R-})(r_R - r_P) + \tfrac{1}{2}(\dot{\psi}_{P-} + \dot{\psi}_{R-})(t^R_- - t^P_+). \tag{3.56}$$

Notice that in (3.53), (3.54), (3.13), and (3.14), the values $X_\pm$ depend on the value of ψ_R [Eq. (3.6)], and therefore this last expression is actually a nonlinear equation

for ψ_R, which we solve by iteration, starting with an estimate based on the values ψ_P and ψ_Q.

Notice also that the value of γ at the shell is necessary for the junction conditions. To obtain it we integrated (3.3) along each slice.

Bibliography

[1] S. L. Shapiro and S. A. Teukolsky, Phys. Rev. Lett. **66**(8), 994 (1991).

[2] S. L. Shapiro and S. A. Teukolsky, Phys. Rev. D **45**(6), 2006 (1992).

[3] R. Penrose, Rivista del Nuovo Cimento **1** (Numero Special), 252 (1969).

[4] K. S. Thorne in *Magic Without Magic: John Archibald Wheeler*, edited by J. Klauder (Freeman, San Francisco, 1972).

[5] T. A. Apostolatos and K. S. Thorne, to Phys. Rev. D, in press.

[6] K. S. Thorne, unpublished research (1973).

[7] Thomas A. Morgan, General Relativity and Gravitation **4**(4), 273 (1973).

[8] W. Israel, Phys. Rev. **153**, 1388 (1967).

[9] C. W. Misner, K.S. Thorne, and J. A. Wheeler, *Gravitation* (Freeman, San Francisco, 1973), p. 860.

[10] A. Ori, Phys. Rev. Lett. **68**, 2117 (1992).

[11] W. H. Press, B. P. Flannery, S. A. Teukolsky, and W. T. Vetterling *Numerical Recipes in C* (Cambridge University Press, 1988).

[12] G. D. Smith *Numerical solution of partial differential equations: finite difference methods*, 3rd ed., (Oxford University Press, 1985).

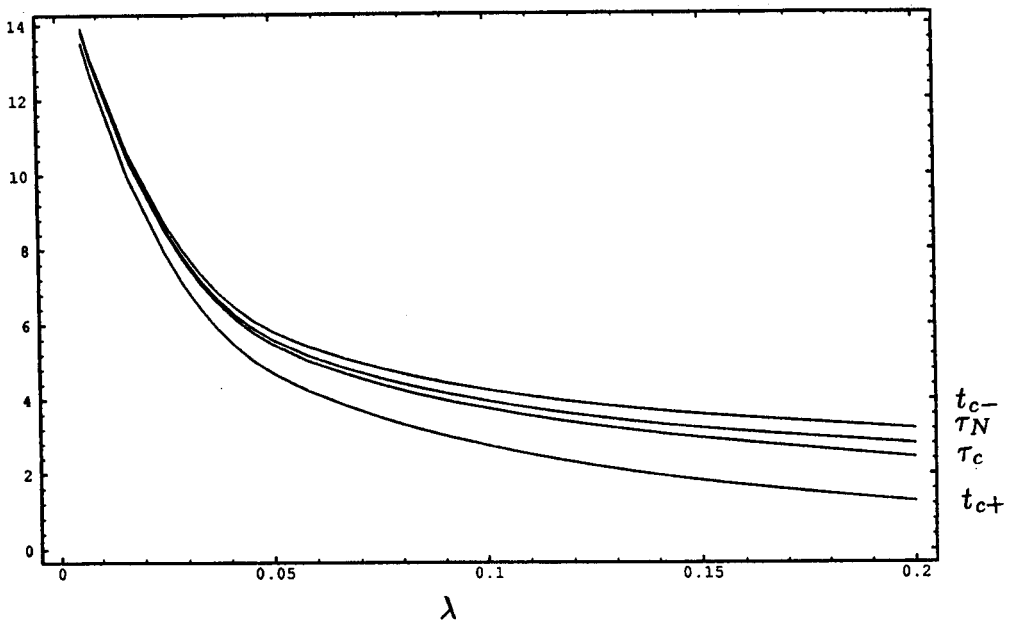

FIG. 1. The proper time, interior and exterior coordinate times, and Newtonian time elapsed from the start of collapse until the formation of the final singularity are here plotted as functions of the shell's mass per unit length λ. These collapse times are expressed in units of the shell's initial radius R_0.

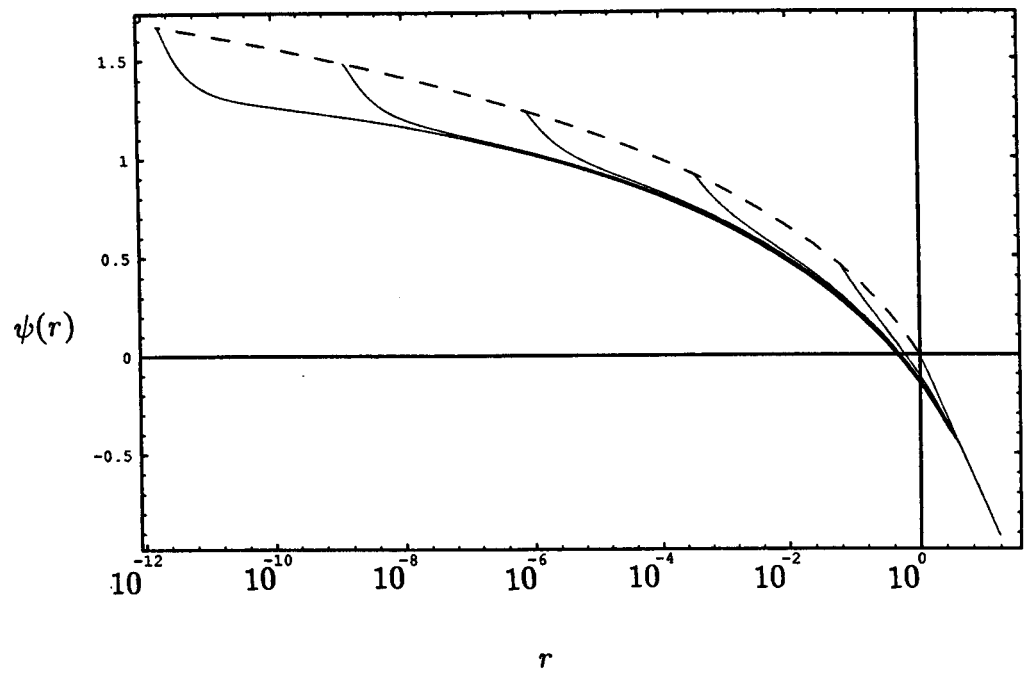

FIG. 2. Shape of the potential $\psi(r)$ outside the shell at different instants t_+ of the collapse, for a shell with mass per unit length $\lambda = 0.1$. The left-hand starting location of each curve is the position of the shell, and the dashed envelope represents ψ_s, the value of ψ on the shell.

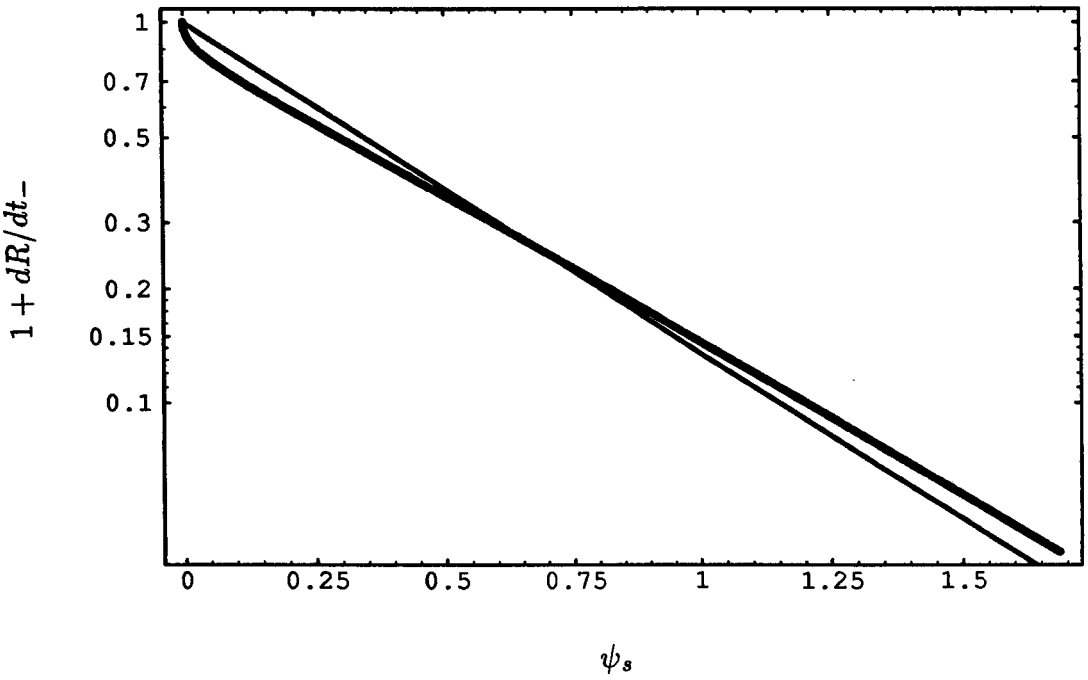

FIG. 3. Comparison between the analytical prediction (thin line) and the numerical results (thick line) for $1 + dR/dt_-$ (difference between the shell's actual coordinate speed and the speed of light) as a function of ψ_s. See Eqs. (3.23) and (3.24). Note that the collapse proceeds along the curves from left to right. The shell has mass per unit length $\lambda = 0.1$.

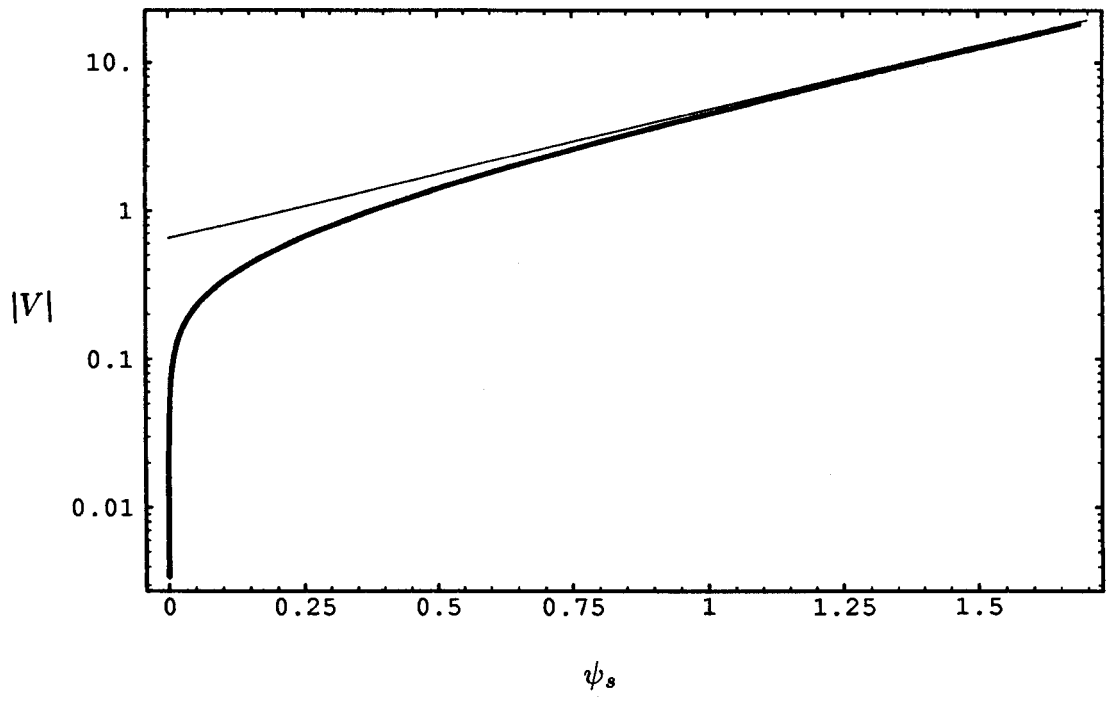

FIG. 4. Comparison between the analytical prediction (thin line) and the numerical results (thick line) for $|V| = |dR/d\tau|$ as a function of ψ_s. See Eqs. (3.26) and (3.24). Note that the collapse proceeds along the curves from left to right. The shell has $\lambda = 0.1$.

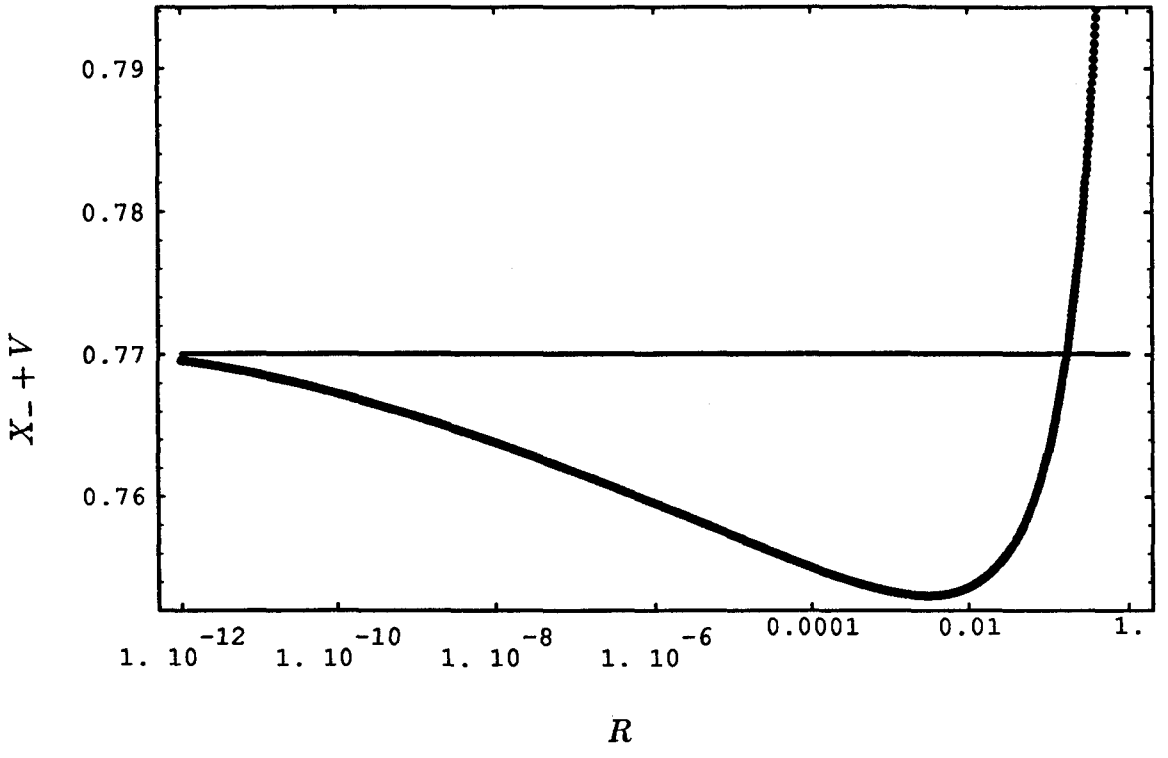

FIG. 5. $X_- + V$ as a function of the shell's radius R, which should asymptote to the constant shown in Eq. (3.27). The horizontal line is the asymptote for the value of the parameter σ that best fits this curve and that in Fig. 6: $\sigma = 1.186$. The shell has $\lambda = 0.1$

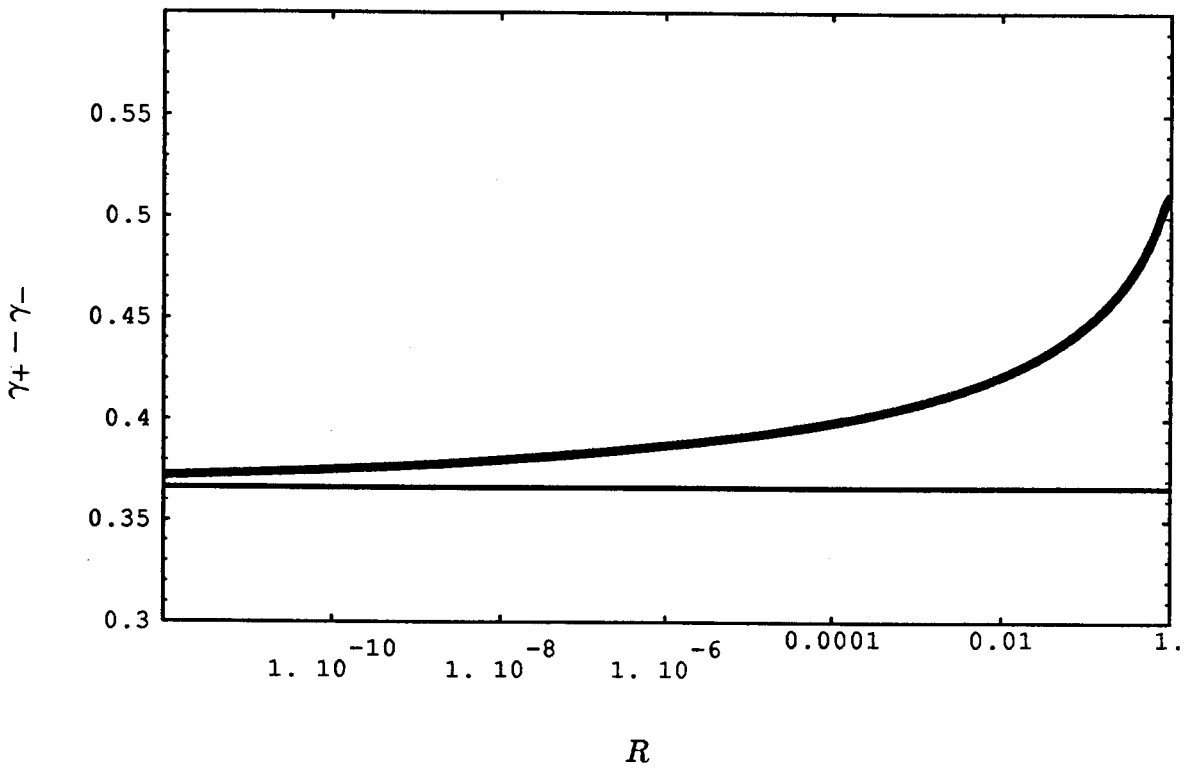

FIG. 6. Jump in the metric coefficient γ across the shell, as a function of the shell's radius R, for $\lambda = 0.1$. The horizontal line is the analytic value of the asymptote for $\sigma = 1.186$; cf. Eq. (3.28).

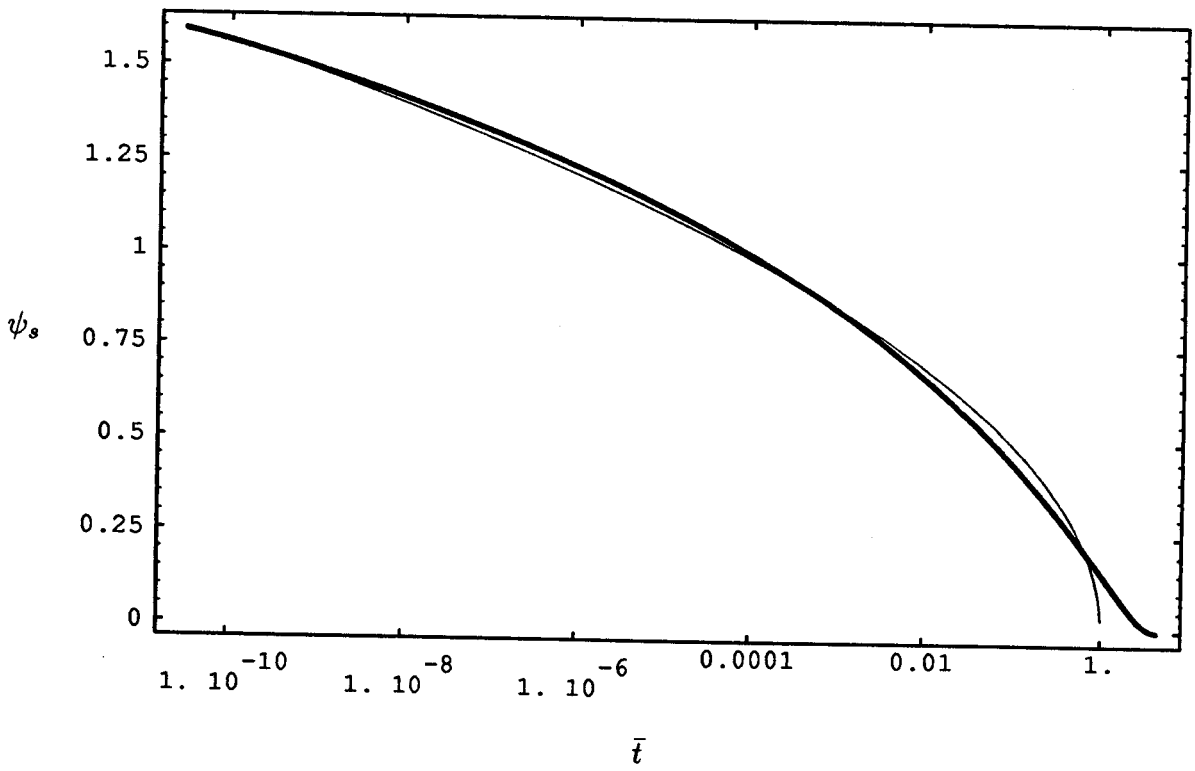

FIG. 7. Comparison between the numerical results for ψ_s as a function of $\bar{t}$ (thick curve) and the approximate analytical relation (thin curve) (3.24) with parameters $\alpha = 0.3262$, $\beta = 0.4999$, and $\Omega = 1.009$. The shell has $\lambda = 0.1$.

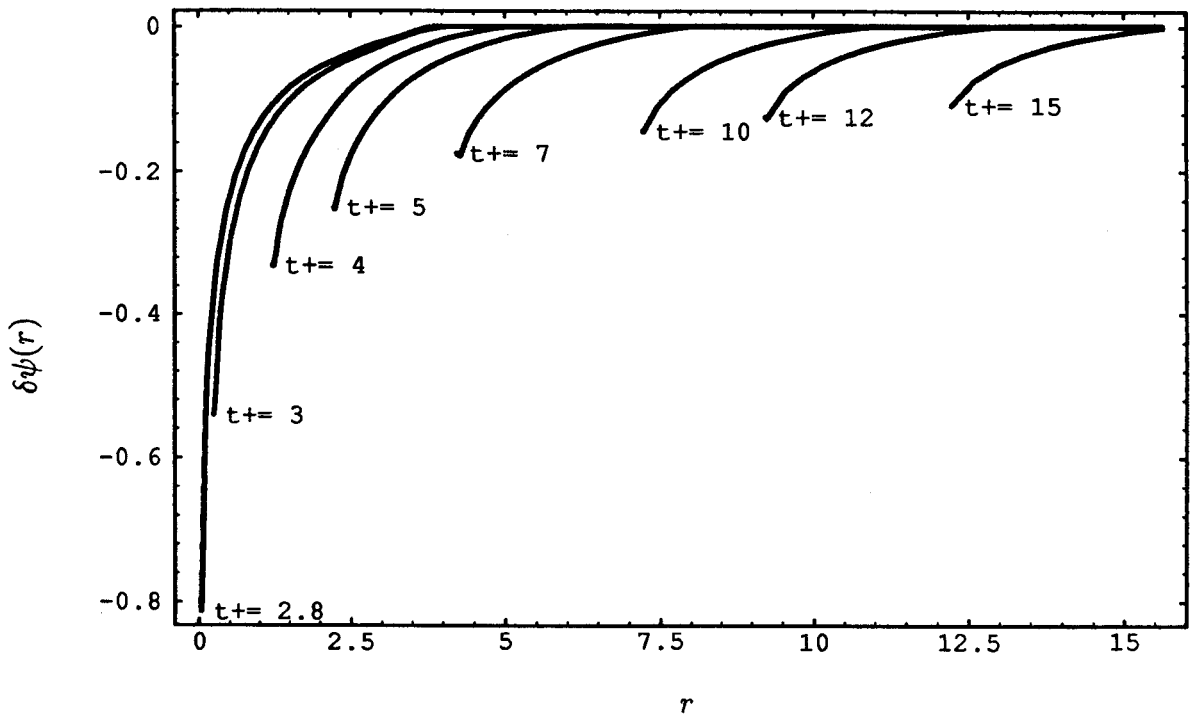

FIG. 8. The Gravitational waves (deviation $\delta\psi$ of ψ from the static solution) emitted by the collapsing shell, plotted as a function of radius for different times. The shell has $\lambda = 0.1$.

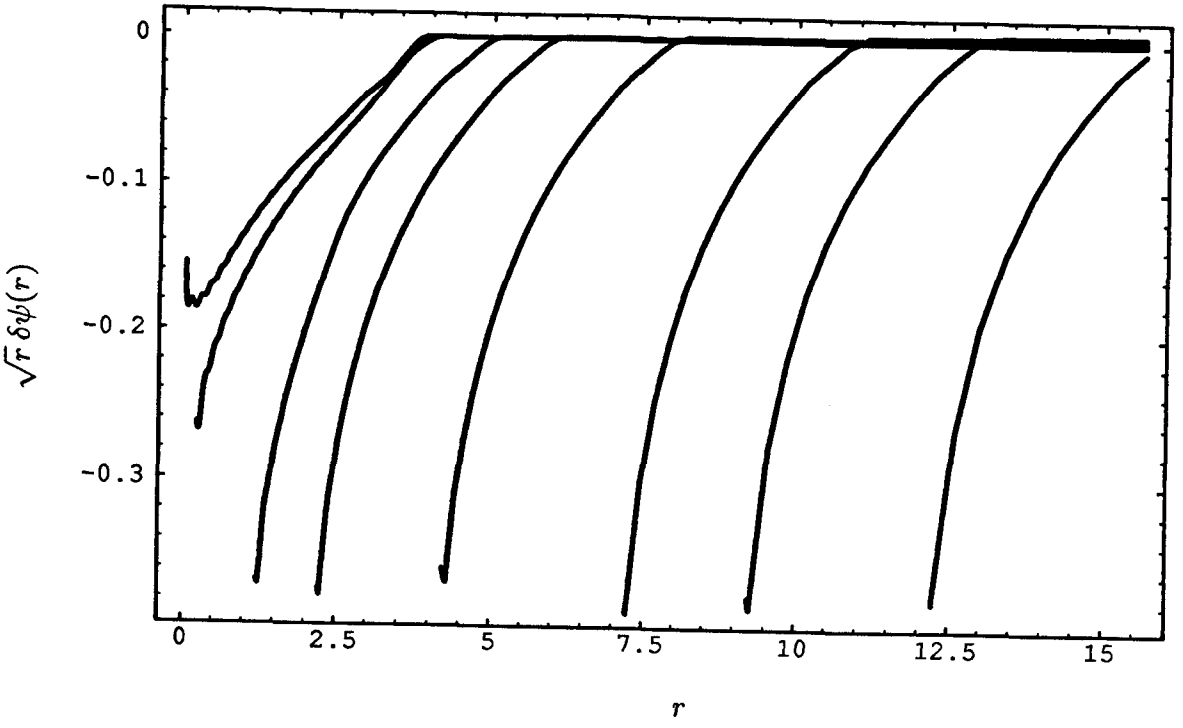

FIG. 9. The Gravitational waves (deviation $\delta\psi$ of ψ from the static solution) emitted by the collapsing shell, scaled by the factor $\sqrt{r}$, plotted as a function of radius for different times. The shell has $\lambda = 0.1$.

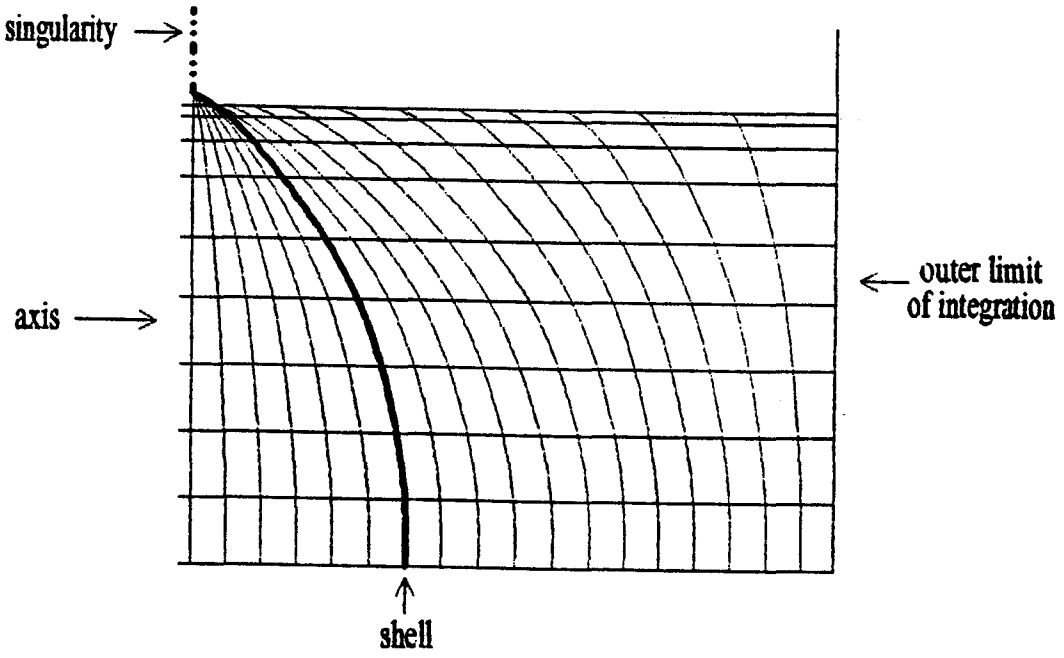

FIG. 10. Adaptive mesh used for the numerical integration of the wave equation.

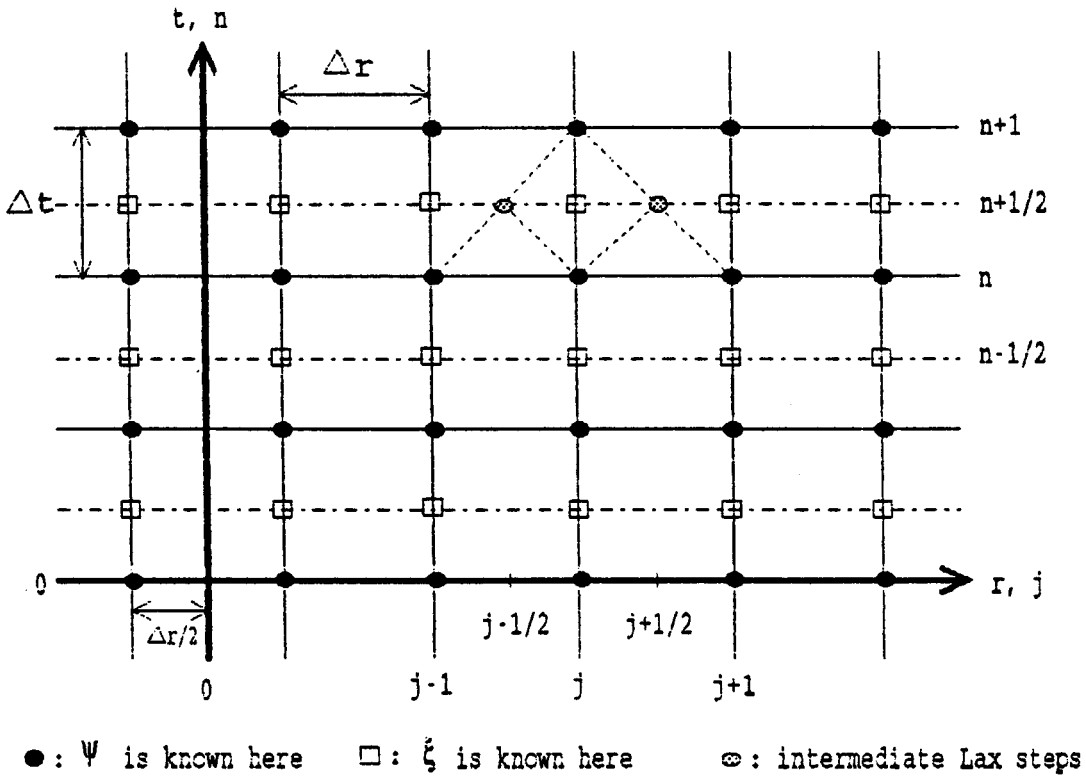

FIG. 11. Implementation of the Lax-Wendroff method for 2 sets of alternating slices.

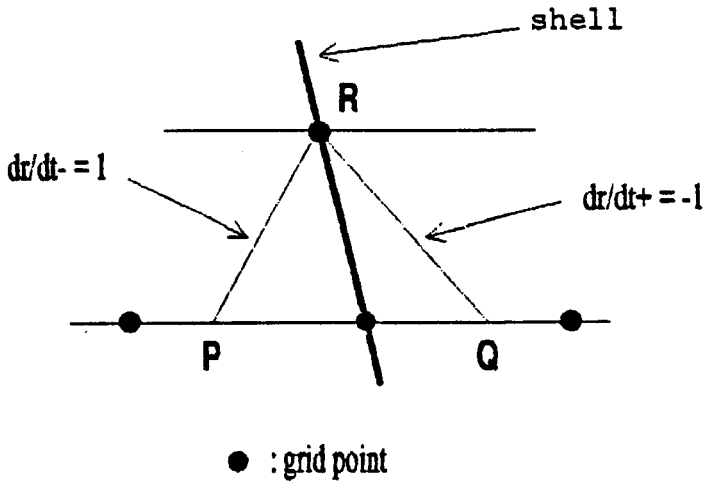

FIG. 12. Method of characteristics applied on the shell with junction conditions to obtain the derivatives of ψ on both sides.

Chapter 4

Billiard balls in wormhole spacetimes with closed, timelike curves: Classical theory

(By F. Echeverria, G. Klinkhammer, and K. S. Thorne. Originally appeared in Phys. Rev. D **44**, 1077 (1991).)

PHYSICAL REVIEW D VOLUME 44, NUMBER 4 15 AUGUST 1991

Billiard balls in wormhole spacetimes with closed timelike curves: Classical theory

Fernando Echeverria, Gunnar Klinkhammer, and Kip S. Thorne
Theoretical Astrophysics, California Institute of Technology, Pasadena, California 91125
(Received 27 February 1991)

The effects of self-interaction in classical physics, in the presence of closed timelike curves, are probed by means of a simple model problem: The motion and self-collisions of a nonrelativistic, classical billiard ball in a space endowed with a wormhole that takes the ball backward in time. The central question asked is whether the Cauchy problem is well posed for this model problem, in the following sense: We define the *multiplicity* of an initial trajectory for the ball to be the number of self-consistent solutions of the ball's equations of motion, which begin with that trajectory. For the Cauchy problem to be well posed, all initial trajectories must have multiplicity one. A simple analog of the science-fiction scenario of going back in time and killing oneself is an initial trajectory which is *dangerous* in this sense: When followed assuming no collisions, the trajectory takes the ball through the wormhole and thereby back in time, and then sends the ball into collision with itself. In contrast with one's naive expectation that dangerous trajectories might have multiplicity zero and thereby make the Cauchy problem ill posed ("no solutions"), it is shown that *all* dangerous initial trajectories in a wide class have *infinite* multiplicity and thereby make the Cauchy problem ill posed in an unexpected way: "far too many solutions." The wide class of infinite-multiplicity, dangerous trajectories includes all those that are nearly coplanar with the line of centers between the wormhole mouths, and a ball and wormhole restricted by (ball radius)$\ll$(wormhole radius)$\ll$(separation between wormhole mouths). Two of the infinity of solutions are slight perturbations of the self-inconsistent, collision-free motion, and all the others are strongly different from it. Not all initial trajectories have infinite multiplicity: trajectories where the ball is initially at rest far from the wormhole have multiplicity one, as also, probably, do those where it is almost at rest. A search is made for initial trajectories with zero multiplicity, and none are found. The search entails constructing a set of highly nonlinear, coupled, algebraic equations that embody all the ball's laws of motion, collision, and wormhole traversal, and then constructing perturbation theory and numerical solutions of the equations. A future paper (paper II) will show that, when one takes account of the effects of quantum mechanics, the classically ill-posed Cauchy problem ("too many classical solutions") becomes quantum-mechanically well posed in the sense of producing unique probability distributions for the outcomes of all measurements.

I. INTRODUCTION AND SUMMARY

A. Motivation

This is one of a series of papers that try to sharpen our understanding of causality by exploring whether the standard laws of physics can accommodate themselves, in a reasonable manner, to closed timelike curves (CTC's).

Previous papers have provided a natural spacetime arena for such an exploration: The arena of spacetimes that contain classical, traversible wormholes (i.e., multiply connected spatial slices). Morris, Thorne, and Yurtsever [1] showed that generic relative motions of the mouths of a traversible wormhole produce CTC's that loop through the wormhole's throat, and Frolov and Novikov [2] showed that generic gravitational redshifts at a wormhole's two mouths, due to generic external gravitational fields, also produce CTC's. (It is not clear whether the laws of physics permit the existence of such traversible wormholes; the attempt to find out is a separate line of research [1, 3–5], which we shall not discuss here.)

A consortium [6] of researchers from Moscow, Milwaukee, Chicago, and Pasadena (henceforth referred to as "the consortium") has raised the issue of whether the Cauchy problem is well posed in spacetimes with CTC's, and has explored many facets of the issue. This paper is one of several that elaborate on the ideas raised by the consortium [6].

Two examples of wormhole spacetimes with CTC's are depicted in Fig. 1. Both of these spacetimes are flat and Minkowski, except for the vicinity of the wormhole throat. The wormhole is arbitrarily short, and its two mouths move along two world tubes that are depicted as thick lines in the figure. The mouths are so small compared to their separation that one cannot see in the figure their finite size. Proper time τ at the wormhole throat is marked off along the mouths' world tubes; points with the same values of τ are the same event, on the throat, as seen through the two different mouths.

In Fig. 1(a) mouth 1 remains forever at rest, while mouth 2 accelerates away from 1 at high speed, then returns and decelerates to rest. Because the motions of the two mouths are like those of the twins in the standard special-relativistic twin paradox, we shall refer to this as the "twin-paradox spacetime." The same relative aging as occurs in the twin paradox produces, here, closed timelike curves that loop through the wormhole [1]. The

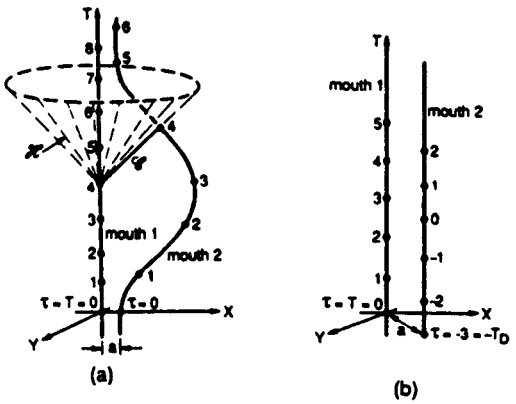

FIG. 1. Two examples of wormhole spacetimes with closed timelike curves. (a) The "twin-paradox spacetime," (b) the "eternal-time-machine spacetime."

light-cone-like hypersurface $\mathcal{H}$ shown in the figure is a Cauchy horizon. Through every event to the future of this Cauchy horizon $\mathcal{H}$ there are CTC's; nowhere in the past of $\mathcal{H}$ are there any CTC's.

In Fig. 1(b) the two mouths are both forever at rest, but with a time delay T_d between them that is greater than the distance a separating them. Because there are CTC's looping through the wormhole throughout this spacetime, the wormhole can be used in principle as a "time machine" for traveling arbitrarily far into the past or the future. For this reason, it has become conventional to call this the "eternal-time-machine spacetime."

Many aspects of the twin-paradox spacetime and the eternal-time-machine spacetime have been studied elsewhere in the literature [1, 6, 3, 7]. Most importantly for us, the consortium [6], and Friedman and Morris [7] have used these spacetimes as "testbed arenas" for studying whether the Cauchy problem is well posed in the presence of CTC's.

As the consortium has shown [6], it is an exceedingly delicate enterprise to pose initial data in a region of spacetime that is threaded by CTC's (the region to the future of the Cauchy horizon in the twin-paradox spacetime; anywhere, except past null infinity, in the eternal-time-machine spacetime). The delicacy is caused by the absence of well-behaved spacelike or null hypersurfaces in such a region, on which to pose the data. Various aspects of this delicacy are discussed by the consortium [6] and by Yurtsever [8], and we shall not in this paper attempt to elucidate them further. Rather, we shall confine attention to the more straightforward situation of initial data that are posed in regions to the past of all CTC's; i.e., data posed on a spacelike or null Cauchy surface to the past of the Cauchy horizon $\mathcal{H}$ in the twin-paradox spacetime, and data posed on past null infinity in the eternal-time-machine spacetime. We shall ask (as did the consortium [6]) whether the Cauchy problem is well posed for such initial data, in the following sense: If one gives the same standard initial data as one would do in a spacetime without CTC's, then for each choice of those data does there exist a self-consistent, global solution of the standard, local evolution equations, and if so is the self-consistent solution unique? (The demand for self-consistency has been discussed in depth by the consortium [6].)

One can ask about the well posedness of the Cauchy problem for a variety of types of evolving systems in spacetimes with CTC's. The first step, carried out by Friedman and Morris [7], was to study the evolution of a classical, massless scalar field ϕ. Friedman and Morris showed rigorously that the Cauchy problem is well posed for such a field in the eternal-time-machine spacetime: Every arbitrary initial value of the field $r\phi$ (where r is radial distance), posed at past null infinity (limit as $T-r \to -\infty$), gives rise, via the standard local evolution equation $\Box\phi = 0$, to a unique, globally self-consistent field ϕ throughout the eternal-time-machine spacetime. It seems highly likely that this behavior is prototypical in the sense that, for any zero-rest-mass, noninteracting, classical field (e.g., the vacuum electromagnetic field) in any stable wormhole spacetime with CTC's, the Cauchy problem will be well posed [1, 6, 7].

It seems probable that the well posedness of the Cauchy problem for the field ϕ results from the fact that ϕ has no self-interactions. More likely to produce peculiar results is a system that, after traveling around a nearly closed timelike world line, can interact with its younger self (e.g., a person who tries to kill his younger self). The simplest such classical system is a single, classical particle that carries a hard-sphere, repulsive potential and has no internal degrees of freedom (a "billiard ball"), and that travels with a speed small compared to light so special-relativistic effects can be ignored. The purpose of this paper is to study the Cauchy problem for such a billiard ball in the twin-paradox and the eternal-time-machine spacetimes.

Other papers in this series study the well posedness of the Cauchy problem for systems that embody other pieces of physics: A companion paper to this one (paper II [9]) studies the effects of nonrelativistic quantum mechanics on the Cauchy problem for this paper's billiard ball; Novikov and Petrova [10] are currently studying a classical billiard ball that has huge numbers of internal degrees of freedom and thus can behave inelastically when it collides with itself; and Novikov [11] has examined, semiquantitatively, a number of complicated classical systems (e.g., a bomb that explodes in response to a trigger signal, sending explosive debris through a wormhole and backward in time where it tries to trigger the explosion before the explosion actually occurs). For his complicated classical systems, Novikov shows that it is *plausible* that there always exists at least one self-consistent solution, no matter how paradoxical the initial data may appear. Unfortunately, for such complicated systems it seems hopeless to obtain firm results. Accordingly, in this paper, in a quest for firmness, we examine the simplest system we can think of that has self-interactions: the perfectly elastic, nonrelativistic billiard ball.

B. The Cauchy problem for classical billiard balls

In this paper we pose our initial data (initial billiard ball *trajectory*, by which we mean *initial path and speed*), in the region of spacetime that is devoid of CTC's: before the Cauchy horizon for the twin-paradox spacetime [Fig. 1(a)], or at past null infinity for the eternal-time-machine spacetime [Fig. 1(b)]. For the twin-paradox spacetime, we confine attention for simplicity to initial trajectories that take the ball into the vicinity of the wormhole long after mouth 2 has returned to rest. This permits us, throughout the calculation, to ignore the early-time, relative motion of the wormhole mouths and to treat the twin-paradox spacetime as though it were the same as the eternal-time-machine spacetime, i.e., the same as Fig. 1(b).

The structure of this (common) spacetime can be understood easily as follows [6]: Take ordinary, flat, Minkowski spacetime, cut out of it the world tubes of two balls that are at rest in a chosen Lorentz coordinate system (T, X, Y, Z), and identify the surfaces of the balls, with a time delay T_d between them. The surfaces of the two balls are the mouths of the wormhole, and because they have been identified with each other, the wormhole is vanishingly short.

We shall denote by D the separation between the centers of the two mouths as measured in the Lorentz frame where they are at rest, by b the radii of the two mouths (radius of curvature of their surfaces), by T_d the time delay between the two mouths, and by r the radius of the billiard ball. Throughout this paper we shall measure spatial distances in units of D (so the wormhole mouth separation is unity) and times in units of T_d (so the time delay between the two mouths is unity); and we shall denote by $B \equiv b/D$ and $R \equiv r/D$ the wormhole radius and the billiard ball radius, measured in these units, and by v the billiard ball speed, measured in these units (units of D/T_d).

The identification we shall use for the two wormhole mouths is one in which diametrically opposed points (points obtained by reflection in the plane half way between the two mouths) are identical. Stated more pedestrianly (see Fig. 2): Adjust the Lorentz frame's spatial, Cartesian coordinates so the line of centers between the two mouths lies on the X axis. Then set up a right-handed spherical polar coordinate system (Θ, Φ) on the right mouth with the polar axis pointed in the $-X$ direction (along the line of centers, toward the left mouth) and with $\Phi = 0$ along the $-Y$ direction; and set up a left-handed spherical polar coordinate system (Θ, Φ) on the left mouth with polar axis pointed in the $+X$ direction (along the line of centers, toward the right mouth) and with $\Phi = 0$ along the $-Y$ direction. Then points on the two mouths with the same values of Θ and Φ are identified.

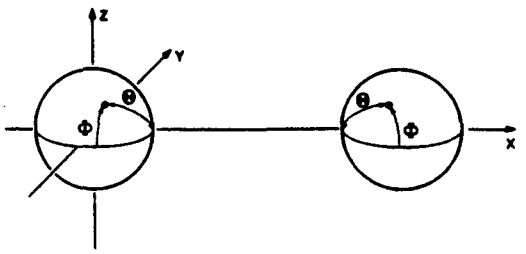

FIG. 2. The identification of points on the two mouths of the wormhole.

In our study of the Cauchy problem for a billiard ball in the above spacetime, we shall focus on the issue of the *multiplicity* of solutions to the ball's equations of motion. For each initial trajectory (initial path and speed) we define the multiplicity to be the number of self-consistent solutions of the equations of motion that begin with that trajectory. Not surprisingly, it will turn out that each initial trajectory has a discrete set of solutions, and thus has multiplicity zero or one or two or .... In the absence of CTC's, all trajectories have multiplicity one, which is just a fancy way of saying that the Cauchy problem is well posed. From exposure to science-fiction scenarios (e.g., those in which one goes back in time and kills oneself), one might expect CTC's to give rise to initial trajectories with zero multiplicity—a severe form of ill posedness for the Cauchy problem. However, we have searched hard for initial trajectories with zero multiplicity and have found none. On the other hand, our search has not covered all initial trajectories (see especially Sec. V), so we cannot guarantee the nonexistence of zero-multiplicity trajectories.

The only trajectories that have any possibility for zero multiplicity are those which, when followed assuming no collision, produce a collision. We call such trajectories *dangerous*. A trajectory can be dangerous only if it leads the ball into the wormhole, and this can happen only if the trajectory is nearly coplanar with the line that connects the centers of the wormhole mouths—more specifically, only if it is within a distance B = (mouth radius) of being coplanar with the line of centers. For this reason, in this paper we restrict attention to nearly coplanar trajectories. The analysis of the billiard ball motion is fairly manageable when the initial trajectory is precisely coplanar (Secs. II, III, and IV); and the *slightly* noncoplanar case (within a distance $\ll B$ of coplanar) can be treated using perturbation theory (Sec. V). However, we have not found a manageable way to analyze the case of coplanarity to within a distance $\sim B$.

For the slightly noncoplanar case, and for $R \ll B \ll D \equiv 1$ (ball small compared to mouths and mouths small compared to separation of mouths), we shall derive a rather remarkable result (Sec. IV A): *All dangerous initial trajectories have infinite multiplicity*. What a contrast with one's naive, science-fiction-based expectation of zero multiplicity.

Figure 3 gives insight into two of the infinite set of solutions in the precisely coplanar case. Figure 3(a) is the self-inconsistent solution which tells us that the initial trajectory, labeled α, is dangerous. When, as in Fig. 3(a), we assume that the ball travels freely along α without suffering a collision, it passes through the wormhole, emerges along β before it went in, and hits itself so hard that it knocks itself along α', preventing itself from go-

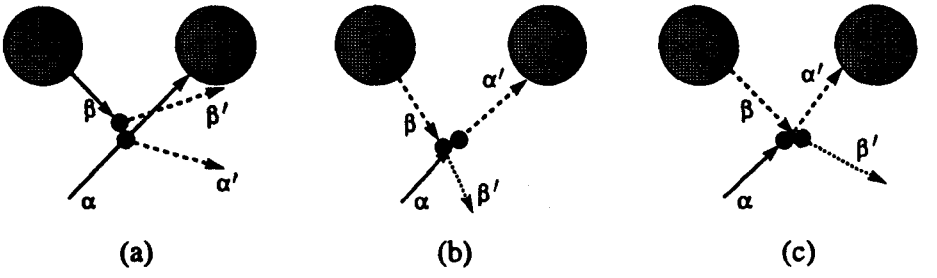

FIG. 3. Spatial diagrams showing a prototypical example of initial data that produce two self-consistent solutions to the billiard-ball equations of motion. Each diagram shows the ball's spatial trajectory, and also shows the ball itself (young version in black and old version in grey) at the moment of self-collision. (a) The self-inconsistent solution which arises if one assumes the ball does not get hit before traversing the wormhole. (b) A "class-I" self-consistent solution in which the ball is speeded up and deflected rightward slightly by a collision before entering the wormhole. (c) A "class-II" self-consistent solution in which the ball is slowed and deflected leftward slightly by a collision before entering the wormhole.

ing through the wormhole. Figure 3(b) is what we call a "self-consistent solution of *class I*" for this same initial trajectory α. The ball, while traveling toward the wormhole on α, gets hit gently on its left rear side and is speeded up a bit and deflected rightward a bit (along trajectory α'); it then enters the wormhole and reemerges before it went down (trajectory β), it tries to pass behind its younger self, but gets hit a gentle, glancing blow by its younger self and deflected slightly (along trajectory β'). Figure 3(c) is what we call a "self-consistent solution of *class II*." While traveling toward the wormhole, the ball (trajectory α) gets hit gently on its front right side and is slowed a bit and deflected leftward a bit (along trajectory α'), it enters the wormhole and reemerges before it went down (trajectory β), it passes in front of its younger self and, just before getting all the way past, it gets hit a gentle, glancing blow by its younger self and deflected slightly (along trajectory β'). We shall study the details of such coplanar class-I and class-II solutions in Sec. IV and in Appendixes A and B—and shall do so not only for $R \ll B \ll D \equiv 1$, but also for wormholes with large mouths and balls with large radii.

The class-I and class-II solutions are small perturbations of the self-inconsistent solution, in the sense that the ball's path is displaced by only enough (typically of order the ball's radius R) to permit the ball to undergo a glancing collision rather than a head-on collision. By contrast, the other self-consistent solutions are quite different from the self-inconsistent one. They (or at least the ones studied in this paper) involve a collision that occurs somewhat farther from the wormhole than for class I and class II, and correspondingly the distance the ball travels, from its first encounter with the collision to its second, is rather larger than in the class-I and class-II solutions. This means the ball must travel farther back in time to achieve such a solution. It does so by undergoing several wormhole traversals. In Sec. III we shall exhibit a self-consistent solution corresponding to each value of the integer $n \equiv$ (number of wormhole traversals); and we shall do so not only when the initial trajectory is dangerous, but in fact for almost all coplanar initial trajectories with speeds $v_1 > D/T_d \equiv 1$. Figure 9 (in Sec. III) is an example with eight traversals.

Our analysis of these multiple-traversal solutions, by contrast with our analysis of the class-I and class-II solutions, is restricted to $R \ll B \ll D \equiv 1$. This restriction permits us to ignore the details of the balls' relative geometry during the collision event (aside from proving, in Sec. II, that the necessary geometry exists). By decoupling the details of the collision geometry from the rest of the solution, we bring the multiple-traversal analysis into an elegant geometric form that contrasts with the complicated algebraic calculations used to analyze the class-I and class-II solutions. This difference motivates our presenting the multiple-traversal analysis (Sec. III) before the class-I–class-II analysis (Sec. IV).

This paper restricts attention, for simplicity, to solutions that entail a single self-collision. There presumably are also multiple-collision solutions, and we speculate about some possible, rather strange ones in the paragraph containing Eq. (3.11). Such solutions can only increase the tendency of initial trajectories to have high, even infinite, multiplicity.

Having identified this tendency toward high multiplicity, we ask ourselves in Sec. III C whether there exist any solutions with multiplicity 1; and in Secs. IV and V, whether there exist any with multiplicity zero. Our search for multiplicity zero comes up empty handed; all initial trajectories that we have examined have self-consistent solutions. By contrast, there is *at least* a small (measure-zero) class of initial trajectories with unit multiplicity: those in which the ball is initially at rest far from the wormhole. We suspect, but have not proved, that the (finite-measure) initial trajectories with speeds $v_1 \ll D/T_d \equiv 1$ and with impact parameters $h \gg D \equiv 1$ also have unit multiplicity; see Sec. III.

The above conclusions are derived for the precisely coplanar case in Secs. II, III, and IV; and they then are all extended to the slightly noncoplanar case in Sec. V. This extension is accomplished by demonstrating (via perturbation theory) that for each slightly noncoplanar initial trajectory there is a one-to-one correspondence between its self-consistent solutions and those of a nearby, precisely coplanar initial trajectory.

This paper's principal conclusion, that the Cauchy problem is ill posed for classical billiard balls in the

eternal-time-machine spacetime, suggests at first sight that the laws of physics might not be able to accommodate themselves in any reasonable way to CTC's. However, the laws of classical mechanics are only an approximation to the more fundamental laws of quantum mechanics, and in paper II [9] it will be shown that quantum mechanics can cure the multiple-solution ill posedness (and can also cure a zero-multiplicity ill posedness, if it occurs): For each initial quantum state of a nonrelativistic billiard ball, posed before the region of CTC's, the sum-over-histories formulation of quantum mechanics predicts unique probabilities for the outcomes of all sets of measurements that one might make in the region of CTC's.

C. Outline of this paper

We begin our quantitative analysis of coplanar solutions in Sec. II, by laying some foundations. In Sec. II A we derive simple "wormhole traversal" rules for the change of a billiard ball's velocity when it goes through the wormhole. Then in Sec. II B we analyze the kinematics of a billiard ball's self-collision when there is only one collision event along the ball's world line. Our analysis simplifies subsequent calculations by embodying all the kinematics (energy conservation, momentum conservation, and friction-free billiard-ball contact at the collision event) in one simple rule: the collision must produce either a direct "velocity exchange," or a "mirror exchange" of velocities.

In Sec. III, by combining the wormhole traversal rules with velocity-exchange and mirror-exchange collisions, and restricting attention to $R \ll B \ll D \equiv 1$, we show that multiple solutions to the billiard ball's equations of motion are ubiquitous. More specifically, we show that a finite measure of such (coplanar) initial trajectories produce not only multiple solutions (Sec. III A), but in fact an infinity of solutions (infinite multiplicity; Sec. III B). We then show that *not all* initial trajectories have infinite multiplicity; there do exist some with only one solution (unit multiplicity; Sec. III C).

In Sec. IV we turn our attention to *dangerous*, coplanar initial trajectories. We begin in Sec. IV A by proving, as a corollary of the Sec. III B analysis, that for $R \ll B \ll D \equiv 1$ almost all such trajectories have infinite multiplicity. Then we extend our search for multiplicity zero to balls that are large enough for the geometry of the collision to couple significantly into the rest of the solution, $R \not\ll B$. In Appendix A and Sec. IV B we derive a set of highly nonlinear, coupled equations governing self-consistent solutions with such collisions. Those equations are valid not only for $R \not\ll B$, but also for $B \not\ll D \equiv 1$. However, in Appendix B and Sec. IV C we return to the restriction $B \ll D$ and there search for solutions of the equations. We find analytic, perturbation-theory solutions of classes I and II for almost all initial trajectories; and we construct numerical solutions for some typical initial trajectories in the extreme regions where the perturbation-theory solutions fail. Our spot checks in these extreme regions have not turned up any initial trajectories for which numerical solutions do not exist.

In Sec. V, using perturbation theory, we extend to slightly noncoplanar initial trajectories all the coplanar results of the previous sections.

II. FOUNDATIONS: WORMHOLE TRAVERSALS AND SELF-COLLISIONS

In this section we give brief analyses of coplanar wormhole traversals and billiard-ball self-collisions—analyses that produce simple rules for use in subsequent sections.

A. Coplanar wormhole traversals

For nearly all the wormhole traversals encountered in this paper, the ball's trajectory is coplanar with the line of centers of the wormhole mouths, and the ball enters mouth 2 and exits from mouth 1, thereby traveling backward in time. In this section we shall confine attention to such traversals.

For all traversals, we shall presume that the ball is small enough (ball radius R sufficiently small compared to mouth radius B) that we can ignore the impulsive tidal force exerted on the ball's hard-sphere potential by the concentrated spacetime curvature at the wormhole throat. Just how small R must be for this depends on one's model for the internal structure of the ball.

In this paper our model for the ball will have the following features. (i) We shall refuse to consider collisions that occur while the center of the ball is on one side of the wormhole throat and its colliding surface is on the other; thereby we shall avoid worrying about instantaneous tidal deformations of the ball's hard-sphere potential during the traversal. (ii) We shall assume (for simplicity and definiteness) that, even if R is as large as, say, $B/2$, the ball's center moves through the wormhole in the same manner as would an arbitrarily small ball. (iii) We shall assume that, even for R as large as $B/2$, the ball recovers from its tidal distortions and resumes its radius-R, spherical shape arbitrarily quickly after a traversal. These features of our model are sufficient to permit R to be as large as $B/2$. (Our choice of $B/2$ rather than $B/4$ or $9B/10$ is quite arbitrary.)

Since the ball's center moves through the wormhole in the same manner as would an arbitrarily small ball, its motion must be on a straight line and with constant speed, as seen by an observer at rest on the throat. Such motion guarantees energy and momentum conservation during the traversal, as seen by the observer. (We presume that the wormhole recoils negligibly; i.e., we treat the ball as a "test object" that moves through the fixed wormhole geometry.)

Since the wormhole mouths are both at rest in the external space, constant speed as seen on the throat implies that the speed of the ball, as measured in the exterior, is unchanged by the traversal: $v_{\text{out}} = v_{\text{in}}$.

Straight-line motion, as measured on the throat, implies that the ball's outgoing velocity $\mathbf{v}_{\text{out}}$ makes the same angle θ, with the outgoing mouth's outward normal, as the ball's ingoing velocity $\mathbf{v}_{\text{in}}$ makes with the ingoing mouth's inward normal. This in turn implies (cf. Fig. 4) that the angle ψ from the mouths' line of centers

(the X axis) to the ball's velocity vector changes during the wormhole traversal from $\psi = \theta + \phi$ to $\psi = \theta - \phi$. Here ϕ is the angular location of the traversal on the wormhole throat as depicted in Fig. 4 (not to be confused with the Φ of Fig. 2).

These conclusions are summarized by the following "wormhole traversal rules":

$$v_{\rm out} = v_{\rm in} , \tag{2.1a}$$

$$\psi_{\rm out} = \psi_{\rm in} - 2\phi . \tag{2.1b}$$

Here and throughout, an italic v denotes the magnitude (speed) of the velocity $\mathbf{v}$.

B. Coplanar self-collisions

In this section and throughout this paper we restrict attention to self-consistent solutions that involve a single self-collision. We shall denote by $\mathbf{v}_1$ the ball's velocity as it enters the collision the first time, by $\mathbf{v}_1'$ its velocity as it leaves the collision the first time, by $\mathbf{v}_2$ its velocity as it enters the second time, and by $\mathbf{v}_2'$ its velocity as it leaves the second time. In other words, the sequence of velocities as measured by the ball itself is $\mathbf{v}_1$, $\mathbf{v}_1'$, $\mathbf{v}_2$, $\mathbf{v}_2'$.

No matter how many wormhole traversals the ball may make between its two visits to the collision event, the "speed in equals speed out" wormhole traversal rule implies that

$$v_1' = v_2 ; \tag{2.2a}$$

and this, combined with energy conservation, implies that

$$v_2' = v_1 . \tag{2.2b}$$

These two speed relations, together with the collision's law of momentum conservation,

$$\mathbf{v}_1' + \mathbf{v}_2' = \mathbf{v}_1 + \mathbf{v}_2 , \tag{2.2c}$$

are a complete set of conservation laws for the ball's velocity.

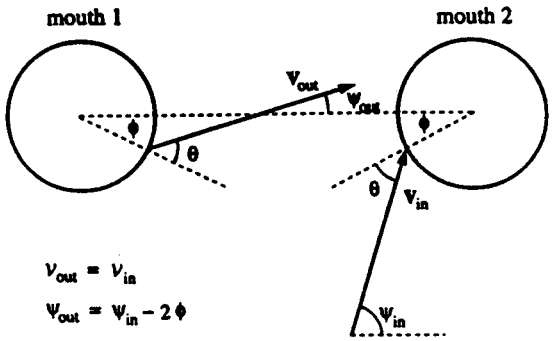

FIG. 4. The "wormhole traversal rules" [Eqs. (2.1)], which govern coplanar wormhole traversals from mouth 2 to mouth 1.

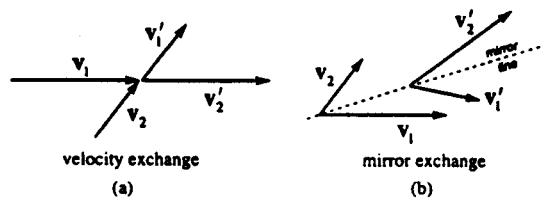

FIG. 5. The two solutions to the self-collision equations: "velocity exchange" [Eq. (2.3a)], and "mirror exchange" [Eq. (2.4a)].

These conservation laws can be satisfied in precisely two ways (Fig. 5): (i) *velocity exchange*,

$$\mathbf{v}_1' = \mathbf{v}_2, \quad \mathbf{v}_2' = \mathbf{v}_1 , \tag{2.3a}$$

for which the relative position of the balls at the moment of collision (the vector separation of their centers) is

$$\mathbf{r}_1 - \mathbf{r}_2 = 2R\frac{\mathbf{v}_2 - \mathbf{v}_1}{|\mathbf{v}_2 - \mathbf{v}_1|} ; \tag{2.3b}$$

and (ii) *mirror exchange*,

$$\begin{aligned} \mathbf{v}_1' &= (\mathbf{v}_2)_{\text{reflected in line parallel to } \mathbf{v}_1+\mathbf{v}_2} , \\ \mathbf{v}_2' &= (\mathbf{v}_1)_{\text{reflected in line parallel to } \mathbf{v}_1+\mathbf{v}_2} , \end{aligned} \tag{2.4a}$$

for which the relative position of the balls at the moment of collision is

$$\mathbf{r}_1 - \mathbf{r}_2 = 2Rs\frac{\mathbf{v}_2 + \mathbf{v}_1}{|\mathbf{v}_2 + \mathbf{v}_1|} , \tag{2.4b}$$

where $s = \text{sign}(v_2 - v_1)$. [The relative position of the balls when they collide, Eq. (2.3b) or (2.4b), is determined by the fact that the momentum transfer $\mathbf{v}_1' - \mathbf{v}_1$ must be along the balls' line-of-centers direction $\mathbf{r}_1 - \mathbf{r}_2$, and the centers must be separated by a distance $2R$.]

In summary, all the constraints on velocity that a self-collision must satisfy are embodied in the simple statement that *either the balls undergo velocity exchange* (2.3a), *or they undergo mirror exchange* (2.4a).

III. UBIQUITY OF MULTIPLE SOLUTIONS FOR COPLANAR INITIAL TRAJECTORIES

In this section we shall use the geometry of the velocity exchange, mirror exchange, and wormhole traversal rules to show that multiple solutions to the billiard ball's equations of motion are ubiquitous. Our discussion will be confined to coplanar initial data. However later, in Sec. V, we shall see that all coplanar solutions are stable (continue to exist) when one perturbs the initial data in an arbitrary but infinitesimal, noncoplanar way. In our discussion, as in Sec. I, we shall refer to the number of solutions that an initial trajectory produces as its "multiplicity."

We begin in Sec. III A by showing that all coplanar initial trajectories that are aimed between the wormhole mouths have multiplicity at least two. One solution is unperturbed straight-line motion, and a second is com-

posed of a wormhole traversal and a velocity-exchange collision. Then in Sec. III B we show that there is a wide variety of coplanar initial trajectories (a set of finite measure) with infinite multiplicities. Each of the solutions we exhibit, for these initial trajectories, has a single mirror-exchange collision, together with some number n of wormhole traversals; n ranges over positive integers up to infinity. Finally, in Sec. III C, we show that a ball initially at rest far from the wormhole has only one solution to its equations of motion: the trivial solution where it remains forever at rest. We also argue, but do not prove firmly, that there is only a single solution for any ball with (i) an initial speed that is sufficiently slow but not zero, and (ii) an initial path of motion that, if extended forever, remains far from the wormhole.

A. Multiplicity larger than 1 is generic

Consider a ball whose initial path is coplanar with the mouths' line of centers and is directed between the mouths, and whose initial speed is arbitrary but nonzero. An obvious solution to the ball's equation of motion is collision-free, wormhole-traversal-free, straight-line motion [Fig. 6(a)]. A second solution is shown, for the case of an arbitrarily small ball, in Fig. 6(b). The ball is hit as it crosses the mouths' line of centers and gets knocked radially into mouth 2. Regardless of the ball's initial speed v_1, it is hit with just the right impulse to give it a speed $v_1' = (D - 2B)/T_d \equiv 1 - 2B$. It travels through the wormhole and returns to its impact point at just the right moment to hit itself and be deflected back onto its original trajectory. Since the wormhole traversal rules (2.1) are trivially obeyed, and the ball has obviously undergone a velocity-exchange collision, all the equations of motion are satisfied.

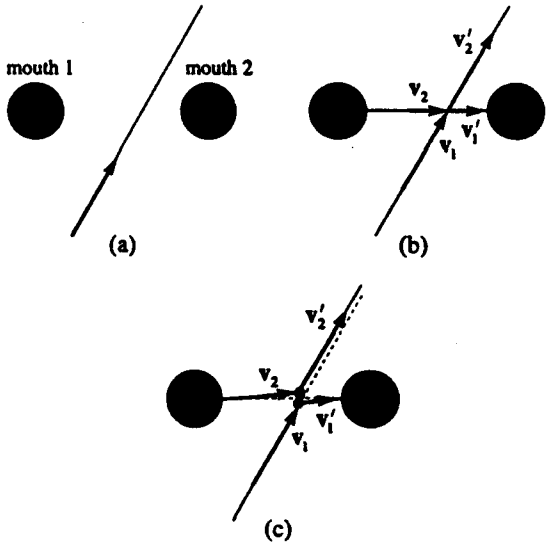

FIG. 6. Solutions to the equations of motion for a coplanar initial trajectory that is directed between the wormhole mouths. The ball's speed is arbitrary. (a) The trivial solution. (b) A solution with one wormhole traversal and a velocity-exchange collision. (c) Modification of solution (b) when the radius of the ball is not negligible.

If the ball's radius is not arbitrarily small, both solutions, (a) and (b), still exist. However, the details of solution (b) are modified slightly, as shown in (c). The collision still entails a precise velocity exchange, and the wormhole traversal rule is still satisfied (but not quite so trivially as before). However, there is now an offset of the various pieces of the ball's path (solid lines) relative to the previous path (dotted lines).

It is not hard to convince oneself that, when the ball is given a finite but small size $R \ll B$, all the solutions described in the remainder of Sec. III remain valid with tiny modifications similar to those in Fig. 6(c). However, for ease of presentation we henceforth in Sec. III shall keep the ball's size infinitesimal.

B. Infinite multiplicity is generic

As a first step in demonstrating that infinite multiplicity is generic (i.e., that all the initial trajectories in a set of finite measure have infinite multiplicity), consider the highly symmetric initial trajectory shown in Fig. 7. The ball's initial speed is arbitrary, and its initial path is coplanar with and perpendicular to the line of centers and is directed half way between the two mouths. Figures 7(a)–7(d) are four self-consistent solutions for this initial trajectory, and they obviously are generalizable to produce an infinite set of solutions. Yet another solution is that of Fig. 6(b), which involves velocity exchange by contrast with the mirror exchange of Fig. 7.

The solution shown in Fig. 7(b) was pointed out to us by Forward [12] (and it motivated our discovery of the infinite multiplicity of solutions). In this solution the ball experiences a mirror-exchange collision, which knocks it radially into mouth 2. It then emerges radially from mouth 1, earlier in external time by precisely the right amount $T_d = 1$ to enable it to return to the collision event. The wormhole-traversal rules (2.1) are trivially satisfied ($\psi_{\rm in} = \phi$, $\psi_{\rm out} = -\phi$; $v_1' = v_2$), and the mirror-exchange rule is satisfied with the mirror line parallel to the line of centers (horizontal dashed line). Since the mirror line must be along $\mathbf{v}_1 + \mathbf{v}_2$, the speed v_2 must be $v_2 = v_1/\sin\psi$ (where ψ, as shown in the figure, is the $\psi_{\rm in}$ of the wormhole-traversal rule). The total distance traveled by the ball between collisions (in the limit, for simplicity, that $B \ll 1$) is $1/\cos\psi$, so the total time lapse as measured by the ball between collisions is $(1/\cos\psi)(1/v_2) = \tan\psi/v_1$. This ball-measured time lapse must be equal to the amount of backward time travel, $T_d = 1$, during the ball's wormhole traversal, in order that the ball return to the collision event. Correspondingly, the value of ψ must be given by

$$\tan\psi = v_1 \ . \tag{3.1}$$

Notice that there is no constraint whatsoever on the initial speed v_1. All the equations of motion are satisfied in Fig. 7(b), when ψ has the value (3.1), regardless of

how large or how small v_1 might be.

In the limit as v_1 goes to zero, the ball is initially at rest on the mouths' line of centers; it gets hit and knocked radially into mouth 2 at speed $v_2 = 1$; it travels backward in external time by $T_d = 1$ while traversing the wormhole; and it then emerges radially from mouth 1, travels to the collision event, hits itself, and comes to rest. Note that this solution is really a continuous infinity of solutions: the time T of the collision is completely arbitrary.

The solution in Fig. 7(c) involves two wormhole traversals. As measured by the ball, using its own local time, the sequence of events is the following: (i) initial path α, (ii) mirror-exchange collision, (iii) path β from collision to mouth 2, (iv) first wormhole traversal, (v) path γ from mouth 1 to mouth 2, (vi) second wormhole traversal, (vii) path δ from mouth 1 to collision event, (viii) path ϵ (opposite to initial path).

As seen by external observers, the sequence is quite different. It is straightfoward to verify, by the same method as was used in solution (b), that in the limit $B \ll 1$ the angle ψ is given by

$$\sin\psi + \tan\psi = 2v_1 , \tag{3.2}$$

and that the sequence of events is as follows. (i) At time $T = -1/(1+\cos\psi)$ before the collision, the ball emerges from mouth 1 and starts traveling along δ toward the collision event, while (in its younger incarnation) it is also traveling up α. (ii) At time $T = -\cos\psi/(1+\cos\psi)$, the ball emerges from mouth 1 and starts traveling along γ toward mouth 2; there are now three incarnations of the ball present. (iii) At time $T = 0$, the collision between incarnations α and δ occurs, knocking incarnation α along β and incarnation δ along ϵ; the third incarnation is still traveling along γ. (iv) At $T = \cos\psi/(1+\cos\psi)$, the ball on γ enters mouth 2 and disappears, leaving just two balls: one on ϵ, the other on β. At $T = 1/(1+\cos\psi)$, the ball on β enters mouth 2 and disappears, leaving just one ball, traveling along the final trajectory ϵ.

Figure 7(d) involves three wormhole traversals. The sequence of paths as measured by the ball is in Greek alphabetical order. It is left as an exercise for the reader to compute the angle ψ in the limit $B \ll 1$ and compute the detailed timings of events as seen by external observers. The reader should also be able to verify (perhaps with the aid of Fig. 9 below and the associated discussion) that the wormhole-traversal rules and mirror-exchange rules are satisfied.

The generalization of the solutions of Fig. 7 to an arbitrarily high number of wormhole traversals should be obvious. We shall examine, in Fig. 9 below, the details of the sequence of wormhole traversals involved in that generalization.

The generalization of these mirror-exchange solutions to arbitrary coplanar initial trajectories is not quite so easy as in the velocity-exchange case of Fig. 6. The method of generalization, for a one-traversal solution, is shown in Fig. 8. The steps in the method are as follows: (i) Specify the initial path α, but not the initial speed v_1; the initial speed will be calculated as the last step in the method. Specify, instead of the initial speed, the location P along the initial trajectory α at which the collision occurs. (ii) By trial and error find a path that takes the

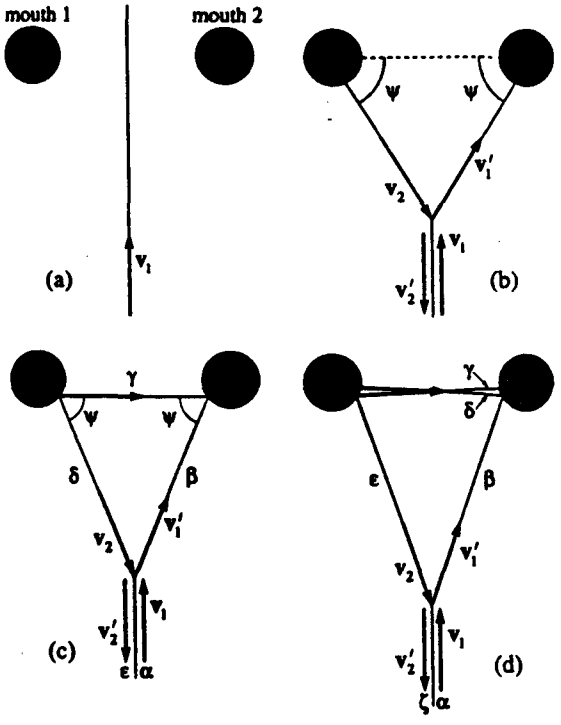

FIG. 7. A specific example of an initial trajectory with an infinite number of solutions (infinite multiplicity). (a) The trivial solution. (b) Solution with one mirror-exchange collision and one wormhole traversal. (c) Solution with one mirror-exchange collision and two wormhole traversals. (d) Solution with one mirror-exchange collision and three wormhole traversals. Solution (b) was pointed out to us by Forward [12] and motivated our discovery of solutions (c) and (d) and their generalizations.

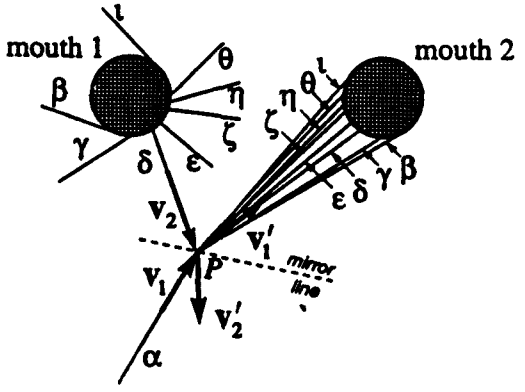

FIG. 8. Trial-and-error method of generating a one-traversal, mirror-exchange solution for an arbitrary, coplanar initial trajectory.

ball from point P to mouth 2, then through the wormhole in accord with the wormhole-traversal rule, then back to point P. That the trial and error will produce precisely one path of the desired type is demonstrated by the sequence of trials β, γ, $\delta, \ldots, \iota$. The wormhole traversal rule (2.1b) guarantees that the modest displacements of the path into mouth 2, in going from β to γ to ... to ι, will produce the large swing of the path around mouth 1 that is shown in Fig. 8. This large swing, in fact, is an obvious consequence of the "diverging-lens" property of any wormhole mouth [13,1]. And this monotonic, "diverging-lens swing" will obviously produce precisely one path of the desired form: path δ in Fig. 8. (iii) From the collision-to-collision travel distance along path δ and the backward time travel $T_d = 1$ of the wormhole traversal, compute the speed $v_2 = v_1'$ with which δ must be traversed. This, together with the path δ, gives the velocities $\mathbf{v}_2$ and $\mathbf{v}_1'$. (iv) From the fact that these $\mathbf{v}_2$ and $\mathbf{v}_1'$ must be the reflection of each other in the mirror line, infer the mirror line's orientation. (v) From the fact that the mirror line must be parallel to $\mathbf{v}_1 + \mathbf{v}_2$, and from the known value of $\mathbf{v}_2$ and direction of $\mathbf{v}_1$ (along α), *compute the ball's initial speed* v_1. (vi) From the initial speed and direction infer the initial velocity $\mathbf{v}_1$. (vii) Reflect this $\mathbf{v}_1$ in the mirror line to get $\mathbf{v}_2'$. All details of the solution are now known, and all the ball's equations of motion have been satisfied.

This same method can be used to produce solutions with one mirror-exchange collision and an arbitrary number of wormhole traversals:

For simplicity, restrict attention to a ball with radius R and a wormhole with mouth separation $D \equiv 1$ and mouth radius B satisfying

$$R \ll B \ll 1 . \tag{3.3}$$

Consider an arbitrary coplanar initial trajectory, as shown in Fig. 9(a). It is characterized by the ball's initial speed v_1, the angle ψ_A that its initial velocity makes with the mouths' line of centers, and its initial impact parameter h with respect to the center of mouth 2. (The subscript A is used on ψ_A because, in the limit that the collision point is infinitely far from the wormhole, the angle ψ_0, at which the ball first hits mouth 2, asymptotically approaches ψ_A; cf. Eq. (3.10) below: ψ_A is the *asymptotic* value of ψ_0.) By suitable choices of these parameters in the range $0 \le v_1 < \infty$, $0 \le \psi_A \le \pi$, and $-\infty < h < \infty$, we can describe all possible coplanar initial trajectories. (Trajectories with $-\pi < \psi_A < 0$ are obtained from those with $0 < \psi_A < \pi$ by reflection in the line of centers.) As we shall see, to obtain an infinite number of solutions, each with a single mirror-exchange collision and all with the same initial trajectory, we need only place two constraints on the initial trajectory:

$$v_1 > 1, \quad \psi_A > B . \tag{3.4}$$

There typically will be solutions (e.g., the class-I and class-II solutions of Fig. 3) in which the collision occurs in the vicinity of the wormhole. However, in this section, in order to demonstrate the existence of infinite numbers of solutions, we can and shall restrict attention to collisions that occur far from the wormhole, i.e., at

$$L \gg 1 \quad \text{and} \quad L \gg h , \tag{3.5}$$

where L is the distance, along the initial trajectory, from the collision to the point of closest approach to mouth 2; cf. Fig. 9(a). As was the case in Fig. 7, for a fixed incoming trajectory, the location L of the collision will turn out to depend on the number n of wormhole traversals, and in the limit $n \to \infty$, L will become arbitrarily large. In the discussion associated with Fig. 8, we regarded the initial path and L as fixed, and solved for the initial speed v_1. Here we shall regard the initial path and speed (i.e., ψ_A, h, and v_1) as fixed and shall solve for L in terms of ψ_A, h, v_1, and n.

Because $L \gg 1$, the velocity $\mathbf{v}_1'$ with which the ball

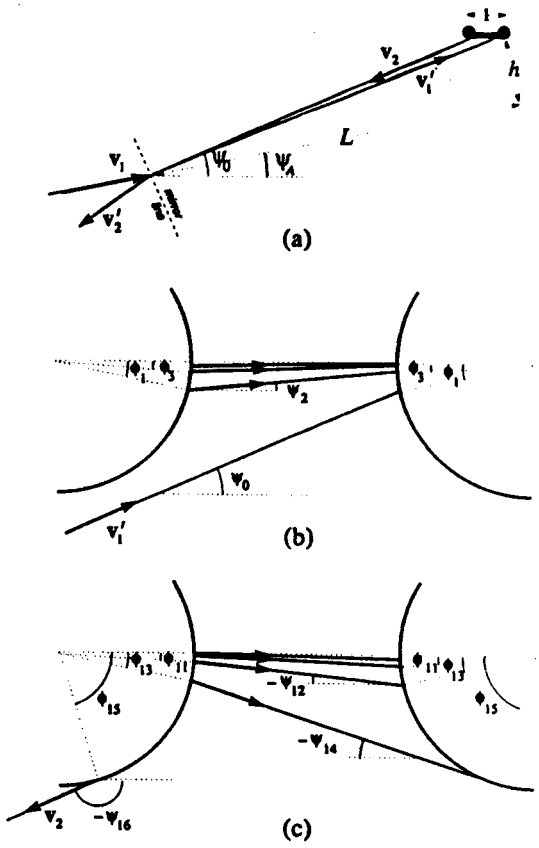

FIG. 9. A solution to the equations of motion for $R \ll B \ll 1$, with an arbitrary number n of wormhole traversals. The figure is drawn for $n = 8$. The initial trajectory, characterized by v_1, ψ_A, and h, is arbitrary except that $v_1 > 1$ and $\psi_A > B$. (a) The large-scale geometry of the solution. (b) The sequence of wormhole traversals as the ball works its way up toward the line of centers. (c) The sequence of traversals as the ball works its way back down from the line of centers. The angles ψ_{2k} and ϕ_{2k+1} are given by the diverging-lens map (3.6).

heads toward the wormhole and the velocity $\mathbf{v}_2$ with which it returns are very nearly antiparallel. Since these velocities must be the reflections of each other, the mirror line (which is along $\mathbf{v}_1 + \mathbf{v}_2$) must be very nearly orthogonal to $\mathbf{v}_2$, and correspondingly, the speeds must be related by

$$v_2 = v_1' = v_1 \cos(h/L) = v_1[1 - \tfrac{1}{2}(h/L)^2] , \qquad (3.6)$$

where we ignore corrections of higher order in h/L. In its sequence of n wormhole traversals, the ball goes backward in time by $\Delta T = -nT_d = -n$. Correspondingly, in order to return to the collision point at the moment of collision, it must travel a total distance nv_2. The total distance traveled, for large L and n, is easily seen from the diagram to be $2L + n$ (aside from unimportant fractional corrections of order h^2/L^2). By equating these distances to each other and using the value (3.6) for the speed v_2, we obtain the relation

$$n = \frac{2L}{v_1 - 1 - \frac{1}{2}(h/L)^2 v_1} . \qquad (3.7)$$

This is the promised relation which determines the location L of the collision in terms of the initial trajectory (characterized here by h and v_1) and the number n of wormhole traversals.

Notice that this relation cannot be satisfied, for arbitrarily large n and positive L, unless $v_1 > 1$. This is the origin of the first of constraints (3.4) on our initial trajectory. The second of those constraints, $\psi_A > B$, is required to ensure that, for arbitrarily large L and n [which means for $\psi_A \simeq \psi_0 \simeq 2\phi_1$ in Fig. 9(b), see discussion below], the ball can reach mouth 2 on its after-collision inward trajectory, without first running into mouth 1.

For a wide class of initial trajectories, there is a lower bound on the number n of wormhole traversals that can produce a self-consistent solution. In the regime of our analysis ($n \gg 1$, $L \gg 1$, $L \gg h$) this lower bound shows up as the fact that n viewed as a function of L with fixed v_1 and h [Eq. (3.7)] has a minimum:

$$n_{\min} = \frac{3\sqrt{3v_1/2}}{(v_1 - 1)^{3/2}}|h| . \qquad (3.8)$$

As the initial speed v_1 decreases toward unity (with h fixed), the minimum number of traversals $n_{\min}$ increases toward infinity.

To recapitulate, for every choice of initial conditions in the range $v_1 > 1$ and $\psi_A > B$, there is an infinite number of solutions (labeled by n) to (i) the laws of energy and momentum conservation in the billiard-ball collision [embodied in Eq. (3.6) which produces mirror-exchange], and (ii) the condition that the ball return to its collision point at the same time T as it left it [Eq. (3.7)]. We can be sure that each $n > n_{\min}$ gives a full solution to the equations of motion as soon as we have verified one more thing: that there is a path leading from the collision point of Fig. 9(a), to mouth 2, then through the wormhole n times [*and obeying the rules* (2.1) *at each traversal*], then out of mouth 1 and back to the collision point. We shall now demonstrate that this is so.

We shall label the wormhole traversals by odd integers $1, 3, 5, \ldots, 2n - 1$, and shall label the path up to mouth 2, the paths between traversals, and the path back to the collision point by even integers $0, 2, 4, \ldots, 2n$. Figure 9 is drawn for $n = 8$, $2n = 16$. The location of traversal $2k - 1$ is described by its angle ϕ_{2k-1} on the wormhole mouths relative to the line of centers, and the direction of path $2k$ is described by the angle ψ_{2k} from the line of centers to the path's velocity direction. The wormhole traversal rule (2.1b), in this notation, reads

$$\psi_{2k+2} - \psi_{2k} = -2\phi_{2k+1} \quad \text{for } 0 \le k \le n - 1; \qquad (3.9a)$$

and the expression for the slope of path $2k$ in terms of the locations of its end points reads (for $B \ll 1$ so $|\psi_{2k}| \ll 1$)

$$\sin\phi_{2k+1} - \sin\phi_{2k-1} = -\frac{\psi_{2k}}{B} \text{ for } 1 \le k \le n - 1 . \qquad (3.9b)$$

For all except the first and last traversals, the angle ϕ is small compared to unity. Therefore, in (3.9b) *the* $\sin\phi_{2k\pm1}$ *can be approximated by* $\phi_{2k\pm1}$, *except for* $\sin\phi_1$ *and* $\sin\phi_{2n-1}$.

Equations (3.9a) and (3.9b) constitute a map from the direction ψ_0 of the ingoing path to the direction ψ_{2n} of the outgoing path. This map embodies all the equations-of-motion constraints on the trial-and-error search for the desired ingoing path. In this map we are to take ψ_0 as fixed by our chosen location for the collision

$$\psi_0 = \psi_A + h/L \qquad (3.10)$$

[cf. Fig. 9(a)], and we are to adjust the location ϕ_1 of the ingoing path so as to produce n wormhole traversals followed by an outgoing path with direction $\psi_{2n} = \psi_0 - \pi$. The diverging-lens behavior of the wormhole guarantees that ϕ_1 can be so adjusted: By elementary geometric optics it should be clear that the correct route must work its way up toward the mouths' line of centers in the manner of Fig. 9(b) during the first half of its trip, and must then work its way back down in the manner of Fig. 9(c) during the second half. In order to do this successfully, the paths on the upward route must have $\psi_{2k+2} \ll \psi_{2k}$ and, correspondingly [cf. Eq. (3.9a)], $\phi_{2k+1} \simeq 2\psi_{2k}$—or, as one sees from a more precise study of the map (3.9a) and (3.9b), $\phi_{2k+1} = 2\psi_{2k}[1 + O(B)]$, where $O(B)$ denotes a k-dependent quantity of order B. In particular (choosing $k = 0$), ϕ_1 must be equal to $\frac{1}{2}\psi_0[1 + O(B)]$.

We can understand qualitatively (but not quantitatively), with the aid of Fig. 8, how the pattern of paths in the vicinity of the hole changes as the trial-and-error value of ϕ_1 is gradually decreased toward and then past the fixed $\frac{1}{2}\psi_0$. Initially, for $\phi_1 \simeq \pi/2$, there is just one wormhole traversal and the outgoing path at mouth 1 has the form β of Fig. 8. As ϕ_1 is decreased, the outgoing path at mouth 1 swings from β to γ, which is the desired path in our present trial-and-error search [point P very far down path γ as in Fig. 9(a)]. We thereby obtain a solution with one wormhole traversal. As ϕ_1 is further decreased, the output path at mouth 1 swings through δ and ϵ and up to ζ. Suddenly at ζ the output path plunges down mouth 2 and emerges from mouth 1

along β. A further decrease of ϕ_1 swings the output path around to γ, the desired position. We now have a solution with two wormhole traversals. By continuing to decrease the trial-and-error ϕ_1 toward $2\psi_0$, we cause the output path to swing again from γ to ζ, there enter the wormhole a second time and emerge on β, then swing down to γ, producing a solution with three traversals, then continue its swing to produce solutions with four traversals, five traversals, six traversals, ... Ultimately, as ϕ_1 decreases through the singular limit point of an infinite number of traversals [ϕ_1 = a certain value $\phi_{1\text{crit}} = \frac{1}{2}\psi_0 + O(\psi_0 B)$], the output path flips over to path η, which passes just above mouth 2; and further decreases of ϕ_1 cause it to swing through a pattern η, θ, ι, reduction of traversals by 1; then η, θ, ι, reduction by 1; ... until the number of traversals is reduced to zero. During this reduction sequence we get no acceptable solutions because the output path is not swinging through the required position γ.

This completes our demonstration that for each coplanar initial trajectory with $v_1 > 1$ and $\psi_A > B$ (and for a ball and wormhole satisfying $R \ll B \ll 1$), there exists an infinite number of solutions of the billiard-ball equations of motion, one corresponding to each value $n > n_{\min}$ of the number of wormhole traversals. To construct the solution with n traversals one can (i) specify the initial trajectory (the parameters ψ_A, h, v_1), (ii) then compute the location L of the collision from Eq. (3.7), and (iii) then find the location ϕ_1 at which the ball first enters mouth 2 by the above geometrical trial-and-error method. (Readers who seek higher rigor than we do might worry that our analysis has examined only the leading-order effects in the small parameters B, R/B, $1/L$, and h/L and has not proved rigorously that higher-order corrections are negligible. We are not worried.)

C. Initial trajectories with only one solution

In this section we turn attention from initial trajectories with infinite multiplicity (an infinite number of solutions), to the issue of whether there exist trajectories with only one solution: collision-free motion. As in the last section, we shall restrict attention to initial trajectories that are coplanar with the wormhole's line of centers and shall describe them by the parameters v_1, h, and ψ_A of Fig. 9(a).

We learned in the last section that for speeds $v_1 > 1$ the multiplicity is almost always infinite. This suggests that we should seek unit multiplicity in the regime $v_1 \ll 1$. Moreover, it seems intuitively clear that a good strategy for avoiding collisions is to keep the initial trajectory far from the wormhole, i.e., to choose $h \gg 1$.

That $h \gg 1$ and $v_1 \ll 1$ are indeed likely to produce unit multiplicity we can see from the following: If there were a solution with one or more collisions, the first collision encountered by the ball presumably would have to be of the type depicted in Fig. 9(a): the old incarnation of the ball flies out from near the wormhole and knocks the young incarnation inward, toward it, and then the old incarnation flies away never to collide again. Such a collision can only be of the mirror-exchange type and not the velocity-exchange type. Moreover, even if the ball encounters many additional collisions near the wormhole, energy conservation in the entire sequence of collisions implies that $v_2 = v_1'$ in the ball's first, distant collision; and this, together with the argument preceding Eq. (3.6), implies that

$$v_2 = v_1' = v_1 \cos(\psi_0 - \psi_A) < v_1 \ll 1 \,. \tag{3.11}$$

In other words, after its first collision, the ball heads toward the wormhole with a speed $v_1' = v_2$ very small compared to $D/T_d = 1$, and after it has finished all its near-wormhole activity, it heads back out toward its first collision with the same tiny speed. This implies, in turn, that the ball must travel backward in time, via wormhole traversals, by a huge amount, $\Delta T > 2h/v_2 > 2h/v_1 \gg 2h \gg 1$. Since each traversal produces a backward time travel of only $T_d = 1$, and there is a forward time travel of at least $D/v = 1/v$ between traversals, the only way the ball can achieve such an evolution is by a peculiar sequence of multiple collisions near the wormhole that build up speeds $v > 1$, temporarily, followed (from the ball's viewpoint) by multiple wormhole traversals into the past at these high speeds, and then followed (from the ball's viewpoint) by collisions that reduce the ball back to $v_2 \ll 1$ and send it back out toward its first collision event. We have searched cursorily for such peculiar solutions, without success, and we suspect they do not exist. However, we have no proof.

On the other hand, in the limit that the ball's initial velocity is precisely zero, and the ball's initial location is far from the wormhole mouths, it is easy to prove (with one caveat; see below) that there is only one solution, the trivial one where the ball remains always at rest. The proof makes use of a sequence of nested convex surfaces that enclose the wormhole mouths, which for concreteness we take to be ellipsoids of revolution (Fig. 10). The ellipsoids are labeled by a generalized radius r which increases outward. We require that the ball initially reside at a radius r_0 larger than that, $r_{\min}$, of the ellipsoid which barely encloses both wormhole mouths.

Now, suppose that there were a solution to the equations of motion other than the one in which the ball re-

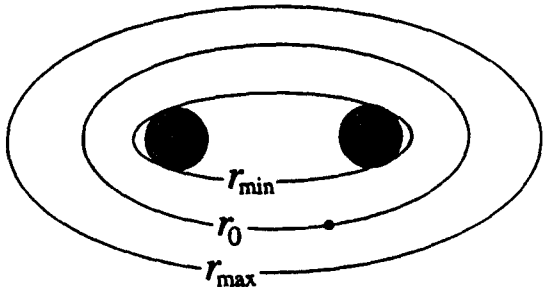

FIG. 10. Nested ellipsoids of revolution surrounding the wormhole, which are used to prove that a ball initially at rest sufficiently far from the wormhole must always remain at rest.

mains at rest. In this solution, the ball would have to undergo one or more self-collisions. There are two possibilities: (i) As seen by the ball there is an infinite sequence of self-collisions that goes on and on forever. We have not been able to rule out such a solution rigorously, but it seems exceedingly unlikely that one could exist. (ii) As seen by the ball there is a last collision. We restrict ourselves to this case.

After completing all its collisions, in order to conserve energy (cf. Fig. 5 of Ref. [6]), the ball would have to return to rest. Let r_{max} be the largest radius the ball reaches while it is in motion. Since $r_{max} \geq r_0 > r_{min}$, this largest radius must lie outside the wormhole, and there thus must be a collision at this r_{max}, for otherwise the moving ball would be at larger radii momentarily before or after it is at r_{max}. However, the object that the ball collides with, as it rises to r_{max} and then gets deflected back downward, can only be the ball itself (since there exist no objects in this problem except the ball and the wormhole), on a path that is coming downward from radii $r > r_{max}$. We thus reach a contradiction; r_{max} is not the ball's maxium radius. Therefore, there exist no solutions except the trivial one.

Note that this proof fails if the ball is initially at rest inside radius r_{min}, since the maximum radius then can lie at the wormhole mouth, and the wormhole rather than a collision can be responsible for deflecting the ball back inward toward smaller radii. A specific example of a nontrivial solution of this type is the one where the ball is initially at rest on the mouths' line of centers, gets hit and knocked into mouth 2, emerges earlier from mouth 1, hits itself and returns to rest; cf. the second paragraph after Eq. (3.1).

IV. SEARCH FOR COPLANAR INITIAL TRAJECTORIES WITH NO SELF-CONSISTENT SOLUTIONS

We now turn attention to the issue of whether there exist coplanar initial trajectories with vanishing multiplicity—i.e., initial trajectories that have no self-consistent solutions whatsoever. If there are such initial trajectories, they must be of the "dangerous" type, i.e. they must be trajectories that, when followed assuming no self-collision, produce a self-collision; cf. the discussion in Sec. I B.

Our search for zero multiplicity among the dangerous trajectories will be carried out in three pieces. In subsection A we shall consider the restrictive case of a ball and wormhole satisfying $R \ll B \ll 1$, and shall show that in this case all (coplanar) dangerous initial trajectories have infinite multiplicity. In Sec. IV B and Appendix A, we shall completely relax these restrictions, and require only that $B < \frac{1}{2}$ so the wormhole mouths do not overlap each other, and $R/B < \frac{1}{2}$ so the ball can pass through the wormhole and we can ignore the effects of tidal forces on the ball during and after its traversal (cf. Sec. II A). For this case we shall derive a pair of coupled, highly nonlinear algebraic equations that govern self-consistent solutions. These equations have solutions in all regimes we have examined (the multiplicity is nonzero), but their high nonlinearity has prevented us from proving definitively that there always is a solution. In Sec. IV C and Appendix B we shall examine the intermediate case $R/B < \frac{1}{2}$ but $B \ll 1$. In this case we shall show that for a wide range of dangerous initial trajectories there is always at least one self-consistent solution, and we shall argue that this is probably so for all initial trajectories, i.e., the multiplicity is probably always nonzero.

To summarize, our search will turn up no evidence at all for initial trajectories with zero multiplicty.

As a by-product of our search, we shall obtain a detailed understanding of the class-I and class-II solutions depicted in Fig. 3, above.

A. Ball and wormhole with $R \ll B \ll 1$

When $R \ll B \ll 1$, we can infer from the analysis given in Sec. III B above that all dangerous initial trajectories have infinite multiplicity. The argument goes as follows.

Each dangerous initial trajectory, if followed assuming no self-collision, must travel backward in time by a mouth-2 to mouth-1 wormhole traversal so as to produce a self-collision. This means that it must hit mouth 2 upon nearing the wormhole, and not be blocked from doing so by mouth 1, which in turn means that the angle ψ_A in Fig. 9(a) must be larger than B:

$$\psi_A > B \tag{4.1a}$$

[cf. Eq. (4.7) below with $\psi_A = \theta + \phi$]. Moreover, it is easy to see that, if n is the total number of mouth-2 to mouth-1 wormhole traversals that the (self-inconsistent) trajectory undergoes before hitting itself, then the total distance it travels from its first encounter with the event of self-inconsistent collision to its second encounter is $\Delta l > nD = n$. Since the wormhole traversals produce a backward time travel of $\Delta T = -nT_d = -n$, the demand that there be zero external time lapse between the first and second encounters, $\Delta l/v_1 + \Delta T = 0$, implies that the ball's initial speed is

$$v_1 > 1 \,. \tag{4.1b}$$

Since each dangerous initial trajectory satisfies conditions (4.1a) and (4.1b), all dangerous initial trajectories are in the class for which we proved infinite multiplicity in Sec. III B; cf. Eq. (3.4).

B. $B < \frac{1}{2}$ and $R/B < \frac{1}{2}$

Turn next to a wormhole whose size is constrained only by $B < \frac{1}{2}$ (mouths do not overlap) and $R/B < \frac{1}{2}$ (tidal forces ignorable during traversal; cf. Sec. II A).

As in the extreme case of $R \ll B \ll 1$, so also here, all dangerous initial trajectories must extend directly from infinity to mouth 2, so as to initiate their backward time travel. This makes it advantageous to label the initial trajectories by a different triplet of parameters than those of Fig. 9(a) above. The previous parameters were the

initial speed v_1 of the ball's center, its impact parameter h, and its angle ψ_A relative to the wormhole mouths' line of centers. Our new parameters are v_1 and the two angles θ, ϕ shown in Fig. 11. The two sets of parameters are related by $h = -B\sin\theta$, $\psi_A = \theta + \phi$.

In order to make progress in the search for self-consistent solutions in this weakly constrained case of possibly large B and R/B, we have confined our search to self-consistent solutions (i) with just one collision, which (ii) is of the mirror-exchange type, and (iii) in which the ball first encounters the collision event before any wormhole traversal and then encounters it again after only one traversal. We shall characterize such a self-consistent solution by (among others) the two angles α and β shown in Fig. 11; β is the ball's deflection angle when it first passes through the collision event, and α is the angle between the two incoming balls (old incarnation and new incarnation) at the collision event. In Appendix A we show that, corresponding to each nonspurious solution (α, β) of the following two equations, there exists a self-consistent solution of the full equations of motion for the billiard ball; and we give in Appendix A equations for computing all features of that solution. The two equations for α and β are

$$B\sin\alpha\sin\frac{\alpha-\beta}{2}\left[\sin\theta-\sin\left(\theta+\phi-\frac{\alpha-\beta}{2}\right)\right]$$

$$+\sin\beta\sin\frac{\alpha-\beta}{2}\left\{\sin(\theta+\phi)-B\left[\sin\theta+\sin\left(\theta+\phi+\frac{\alpha-\beta}{2}\right)\right]\right\}=(v_1+d)\sin\frac{\alpha+\beta}{2}\sin\alpha\sin\beta\,, \quad (4.2)$$

$$B\sin\left(\frac{\alpha+\beta}{2}-\theta-\phi\right)(\sin\alpha+\sin\beta)+B\sin\theta\sin(\alpha-\beta)-\sin\beta\sin(\alpha-\theta-\phi)=-d\sin\alpha\sin\beta, \quad (4.3)$$

where

$$\rho=\frac{\sin[\frac{1}{2}(\alpha+\beta)]}{\sin[\frac{1}{2}(\alpha-\beta)]}\,, \quad (4.4a)$$

$$d=2sR/(1+\rho^2+2\rho\cos\alpha)^{1/2},\quad s=\mathrm{sign}(d)\,; \quad (4.4b)$$

and if one is interested in the ball's speed between collisions, it is given by

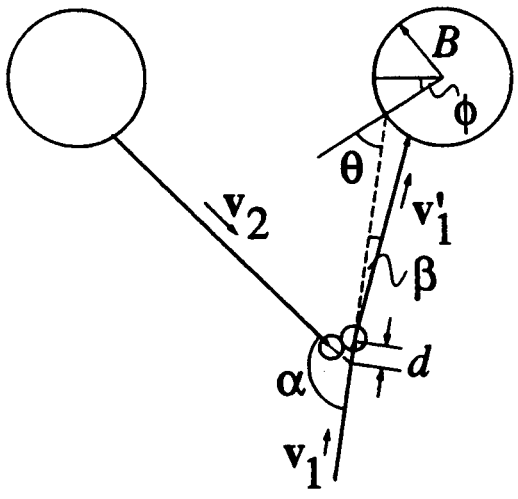

FIG. 11. Geometry of a self-consistent solution with one wormhole traversal and one billiard-ball collision. More details of this geometry are depicted in Figs. 17 and 18 of Appendix A. By convention all angles and distances (e.g., α, β, and d) are positive when their orientations are as shown here.

$$v_2=v_1\rho\,. \quad (4.5)$$

The parameter d is shown in Fig. 11; it is the distance that the ball's younger incarnation must travel *past* the point of intersection of the two incoming trajectories, to reach the collision event. One can choose its sign s arbitrarily in a search for solutions. If $s=+1$ (the case shown in Fig. 11), the ball's older incarnation passes behind the younger, the younger is deflected to the right ($\beta>0$), and we call the collision "class I" [cf. Fig. 3(b)]. If $s=-1$, the older incarnation passes in front of the younger, the younger is deflected to the left ($\beta<0$), and we call the collision "class II" [cf. Fig. 3(c)]

Equations (4.2) and (4.3) for α and β have the following set of *spurious solutions* that were introduced by manipulations carried out in Appendix A:

$$(\alpha,\beta)=(0,0),\ (\pi,0),\ (0,\pi),\ (\pi,\pi),\ (2\phi,0)\,, \quad (4.6a)$$

$$\text{any solution with } \rho<0\,, \quad (4.6b)$$

$$\text{any solution with } \mathrm{sign}(\beta)\neq\mathrm{sign}(d)\equiv s\,. \quad (4.6c)$$

Equations (4.2) and (4.3) for α and β are so horribly nonlinear that we can say only one thing definitive and universal about their solutions: since there are two equations for two unknowns, the solutions must form a discrete set. It is far from obvious, just looking at the equations, whether there exist values of the wormhole and ball radii B, R and initial-trajectory parameters v_1, θ, ϕ that produce zero solutions. Numerical exploration, and the analytic considerations of the next section, have not turned up any such zero-multiplicity trajectories.

C. $B \ll 1$ and $R/B < \frac{1}{2}$

To make further progress in our search for dangerous initial trajectories with no self-consistent solutions, we shall retain $R/B < \frac{1}{2}$, but shall specialize to a wormhole with mouth radii small compared to their separation, $B \ll D = 1$. (Note that these relations imply $R \ll 1$.) We shall also limit ourselves to a large but not complete set of dangerous initial trajectories: those whose self-*inconsistent* solutions have the same form as the self-consistent solutions analyzed in the last section: the ball comes in from infinity, passes through (and ignores) its collision event, traverses the wormhole just once, and then hits its collision event a second (self-inconsistent) time. The parameters of such initial trajectories lie in the range

$$B/2 < \phi < \pi/2, \quad B - \phi < \theta < \phi, \quad v_{1\min} < v_1 < v_{1\max}, \tag{4.7}$$

where

$$\left.\begin{matrix} v_{1\min} \\ v_{1\max} \end{matrix}\right\} = \frac{\cos\theta}{\cos\phi}(1 - 2B\cos\phi) \mp \frac{2R}{\cos\phi}. \tag{4.8}$$

The θ, ϕ part of this dangerous region is the interior of the thick-lined triangle of Fig. 12. We shall call this the "dangerous triangle." The constraint $\theta > B - \phi$ (lower left edge of dangerous triangle) is required so the ball will avoid entering mouth 1 before it reaches mouth 2; parameters (θ, ϕ) near this edge correspond to incoming trajectories that skim past mouth 1, go down mouth 2, emerge from mouth 1, and then collide self-inconsistently near mouth 1. The constraint $\phi < \pi/2$ (right edge of dangerous triangle) is required so the ball's path will intersect itself after passing through the wormhole; near this edge the outgoing path emerges from the wormhole nearly antiparallel to the ingoing path, thereby producing a self-inconsistent collision far from the wormhole. The constraint $\theta < \phi$ (upper left edge of dangerous triangle) is required to make the collision occur before the ball enters mouth 2 a second time; for (θ, ϕ) near this edge, the self-inconsistent collision occurs close to mouth 2. The constraint (4.8) on v_1 (not depicted in the figure) guarantees that the ball returns to the collision region at the right time to produce a self-inconsistent collision.

In Appendix B we carry out a search for self-consistent solutions throughout this range of dangerous initial trajectories. The strategy of the search is based on the physical idea that, because $R < B/2 \ll 1$, the ball travels a distance huge compared to its size R between its first and second encounters with the collision. This means that a very tiny deflection, $|\beta| \sim R \ll 1$, can significantly alter the geometry of the collision, and possibly change it from the self-inconsistent form of Fig. 3(a) to the class-I or class-II self-consistent form of Figs. 3(b) and 3(c). A tiny value of $|\beta|$ goes hand in hand with a tiny change of α from its self-inconsistent-solution value 2ϕ (which is dictated by the wormhole traversal rule shown in Fig. 4). This motivates us to search for solutions in the parameter range

$$|\beta| \ll 1, \quad |\epsilon| \ll 1, \quad \text{where } \epsilon \equiv \alpha - 2\phi. \tag{4.9}$$

In Appendix B we search in this range by expanding Eqs. (4.2) and (4.3) for α, β in powers of ϵ and β. In order to obtain real solutions, rather than just the spurious solutions of Eq. (4.6a), the equations are expanded to quadratic order, and they then are combined to yield one quadratic and one linear equation, Eqs. (B2) and (B12) [in which λ_1 is as defined in Eq. (4.10) below]. These equations have simple analytic solutions throughout the regime (4.7) of dangerous initial trajectories (throughout the interior of Fig. 12's dangerous triangle), except near the triangle's left corner and near its lower left edge.

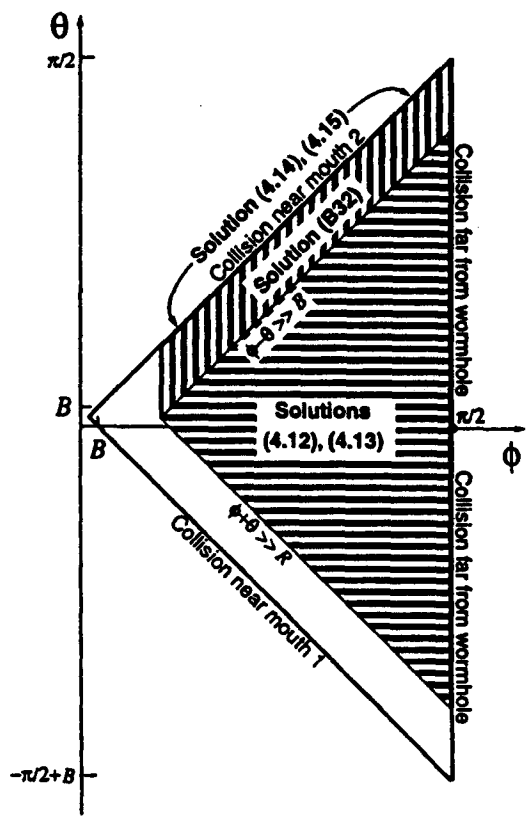

FIG. 12. Parameter space for the ball's initial trajectory when $B \ll 1$, $R/B < \frac{1}{2}$. The interior of the thick-lined triangle is the region of dangerous initial trajectories that produce a self-inconsistent collision after one wormhole traversal [Eq. (4.7)]. We call this the "dangerous triangle." Equations (4.2) and (4.3) govern solutions throughout this dangerous triangle. Simple analytic solutions of these equations are given, in the indicated shaded regions of the dangerous triangle, by the indicated equations. Analytic solutions cannot be derived by the techniques of Appendix B for the white regions of the triangle (left corner and lower left edge), but numerical solutions have been found in spot checks throughout that white region. Figure 14 below shows, as an example, a solution (part analytic, part numerical) all along the upper left edge of the dangerous triangle, including the left corner.

Near this corner and edge, tiny changes of the incoming trajectory produce huge changes in the location of the self-inconsistent solution; and correspondingly, it turns out that self-consistent solutions there typically have a large value of ϵ. This causes the power-series expansion of Appendix B to break down. However, near this corner and edge one can go back to the exact, nonlinear equations (4.2) and (4.3), and find solutions numerically. At all points near the left corner and lower left edge where we have tried, we found numerical solutions. Thus, it seems likely that solutions exist everywhere in the dangerous triangle.

The simple analytic solutions in the horizontally shaded central part of the triangle (i.e., for collisions not close to either mouth; cf. Fig. 12) are interesting and instructive. In describing these simple solutions we shall give formulas not only for β and ϵ (a surrogate for the angle α), but also for the ball's speed v_2 between collisions. Other parameters describing the solutions can be inferred from the equations in Appendix A. To simplify notation in the solutions, we shall characterize the initial speed v_1 and the speed between collisions v_2 by parameters λ_1 and λ_2 defined by

$$v_1 = v_{1\min} + \lambda_1(v_{1\max} - v_{1\min}) , \tag{4.10}$$

$$v_2 = v_{1\min} + \lambda_2(v_{1\max} - v_{1\min}) . \tag{4.11}$$

Note that the dangerous initial trajectories have $0 < \lambda_1 < 1$. In the central region of the triangle ($\phi - \theta \gg B$, $\phi + \theta - B \gg R$, and $\pi/2 - \phi \gg B$) there are two simple solutions to the quadratic and linear equations (B2) and (B12): one of class I, the other of class II. The class-I solution ($s = +1$) is

$$\beta = \frac{8\sin\phi}{\cos\theta(\tan^2\phi - \tan^2\theta)} BR\lambda_1 , \tag{4.12a}$$

$$\epsilon = \frac{8\cos\phi}{\sin(\theta+\phi)}\lambda_1 R , \tag{4.12b}$$

$$\lambda_2 = \left(1 + \frac{2\cos\phi}{\tan^2\phi - \tan^2\theta} B\right)\lambda_1 . \tag{4.12c}$$

The class-II solution ($s = -1$) is

$$\beta = -\frac{8\sin\phi}{\cos\theta(\tan^2\phi - \tan^2\theta)} BR(1-\lambda_1) , \tag{4.13a}$$

$$\epsilon = -\frac{8\cos\phi}{\sin(\theta+\phi)}(1-\lambda_1)R , \tag{4.13b}$$

$$1 - \lambda_2 = \left(1 + \frac{2\cos\phi}{\tan^2\phi - \tan^2\theta} B\right)(1-\lambda_1) . \tag{4.13c}$$

These solutions, which when viewed as functions of λ_1 (i.e., of v_1) are linear, actually extend out of the region $0 < \lambda_1 < 1$ of dangerous initial trajectories: The class-I solution is valid for $R^{-1} \gg \lambda_1 > 1$, as well as for $0 < \lambda_1 < 1$, but it is spurious for $\lambda_1 < 0$ since there it predicts opposite signs for β and s; cf. Eqs. (4.12a) and (4.6c). Similarly, the class-II solution is valid for $-R^{-1} \ll \lambda_1 < 0$, as well as for $0 < \lambda_1 < 1$, but for $\lambda_1 > 1$ it predicts opposite signs for β and s and thus is spurious. At the point $\lambda_1 = 0$ or 1 where one of the solutions stops (becomes spurious), it actually joins onto (converts over into) a valid, collision-free solution in a manner depicted in Fig. 13.

These simple solutions for the interior region of the dangerous triangle (Fig. 12) break down near the triangle's upper left and lower left edges. There, in solving the coupled linear and quadratic equations (B2) and (B12), one must keep nonlinear terms. It is straightforward to do so, and thereby obtain solutions valid near the upper left edge, but not near the left corner or lower left edge. In Appendix B we analyze the region near the upper left edge (collisions that occur near mouth 2): $0 < \phi - \theta \lesssim B$, $\phi \gg B$. By combining Eqs. (B2) and (B12), we obtain a quadratic equation [Eq. (B29)], with rather simple coefficients, for the incoming ball's deflection angle β. Some of the solutions to this quadratic equation are spurious (wrong sign of β for a chosen sign of s). In Appendix B it is shown that, throughout our chosen region ($0 < \phi - \theta \lesssim B$, $\phi \gg B$), there is a nonspurious class-I ($s = +1$) solution, Eq. (B32), but in some parts of that region there is no nonspurious class-II solution. We suspect, but have not proved, that the missing class-II solution actually exists, but the ball first encounters its collision shortly after passing through the wormhole, rather than before, and therefore this solution is beyond the domain of validity of our analysis.

On the upper left edge of the dangerous triangle (at $\phi = \theta$), the class-I solution (B32) has the form depicted in Fig. 14. This figure is drawn for $\lambda_1 = \frac{1}{2}$, $B = 10^{-2}$

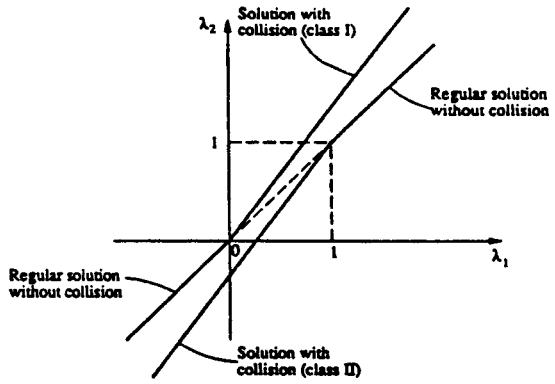

FIG. 13. Billiard-ball speeds for the two self-consistent solutions (4.12) and (4.13) in the central region of Fig. 12's dangerous triangle. (This central region represents collisions that occur neither very close to a wormhole mouth nor at huge distances from the wormhole.) The parameters plotted, λ_1 and λ_2, are proportional to the speeds v_1 and v_2 [Eqs. (4.10) and (4.11)], and the dangerous range of incoming speeds is $0 < \lambda_1 < 1$. At each edge of the dangerous range, one of the solutions joins continuously onto a collision-free solution, and the other continues to exist as a solution with collision.

and $R = 10^{-5}$ (though the solution is valid also when R is close to B). Notice the sharp change in the deflection angle as one passes from $\phi > \pi/4$ to $\phi < \pi/4$, and from $\phi > \sqrt{B} = 0.1$ to $\phi < \sqrt{B} = 0.1$: At $\phi > \pi/4$, the deflection angle β is of order $R = 10^{-5}$ [This is rather larger than in the central region of the triangle, where it is of order BR; cf. Eqs. (4.12a) and (4.13a)]. At $\sqrt{B} < \phi < \pi/4$, β is of order $B = 10^{-2}$. As ϕ decreases toward zero (as one moves toward the left corner of the dangerous triangle), ϵ grows large and the power series expansion of Appendix B begins to break down. We have solved numerically the full, nonlinear equations (4.2) and (4.3) for α and β in this corner region and have verified that a solution continues to exist right up to the corner.

The analytic solution (B32) takes on especially simple forms for a very small ball ($R\tan^2\phi \ll B$), very near the upper left edge of the dangerous triangle ($|\phi-\theta|\tan^2\phi \ll 1$), and away from the regions of rapidly changing β: At $\phi \gg \sqrt{B}$ and $\pi/4 - \phi \gg B$ the solution becomes

$$\beta = \sin\phi\cos 2\phi B, \quad \epsilon = \frac{\cos 2\phi \cos^2\phi}{\sin\phi} B \ ; \tag{4.14}$$

and at $\phi - \pi/4 \gg B$ (but $\pi/2 - \phi \gg \sqrt{R/B}$ and $\pi/2 - \phi \gg |\phi-\theta|^{1/2}$), it becomes

$$\beta = \epsilon = -\frac{4\sin\phi}{\cos 2\phi} R\lambda_1 \ . \tag{4.15}$$

These approximations to the solution are plotted as dashed lines in Fig. 14.

To recapitulate, self-consistent analytic solutions with $|\beta| \ll 1$ and $|\epsilon| \ll 1$ exist throughout the dangerous region of Fig. 12, except its left corner and lower left edge; and we have found numerical solutions in spot checks of that corner and edge. We find no evidence, when $B \ll 1$ and $R/B < \frac{1}{2}$, for initial trajectories with zero multiplicity.

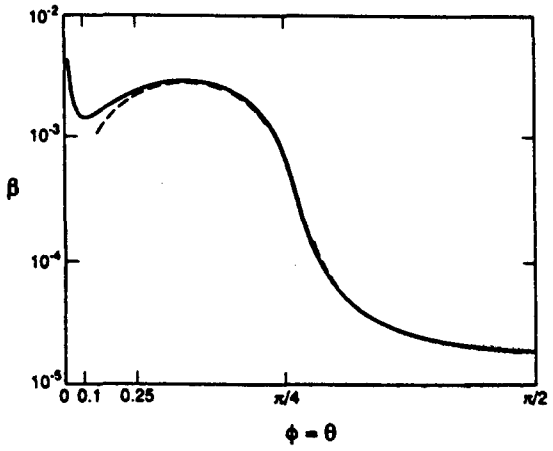

FIG. 14. A combination numerical and analytic solution for the ball's deflection angle β as a function of ϕ, along the upper edge $\theta = \phi$ of Fig. 12's dangerous triangle. This is the class-I solution ($\beta > 0$); the ball and wormhole radii are $R = 10^{-5}$ and $B = 10^{-2}$; and the incoming speed is at the center of the dangerous range, $v_1 = \frac{1}{2}(v_{1\max} + v_{1\min})$ [$\lambda_1 = \frac{1}{2}$; cf. Eq. (4.10)].

V. NONCOPLANAR TRAJECTORIES

In this section we shall extend most of the coplanar results of Secs. III and IV to initial trajectories that are slightly noncoplanar. Thereby we shall accumulate evidence which suggests, but does not really prove, that all noncoplanar initial trajectories have multiplicity larger than zero (i.e., have self-consistent solutions to the equations of motion). Throughout our discussion we shall confine attention to a wormhole with $B \ll 1$. [This same restriction was imposed throughout Sec. III and in all of Sec. IV except in the fully nonlinear equations of motion (4.2) and (4.3).]

As a first step, we shall ask ourselves how nearly coplanar a trajectory must be in order to be dangerous, i.e., in order to produce a self-inconsistent collision, if followed assuming no collision.

Consider an arbitrary initial trajectory. Define the wormhole's "equatorial plane" to be the unique plane that is parallel to this initial trajectory and contains the wormhole's line of centers. At any point along the ball's trajectory, denote by z the height of the ball's center above the equatorial plane, denote by l the distance the ball has traveled (from some arbitrary origin) parallel to the equatorial plane, and denote by $z' \equiv dz/dl$ the inclination of its trajectory to the equatorial plane. Our definition of equatorial plane guarantees that initially the trajectory has $z = \text{const} \equiv z_1$ and $z' = 0$. However, z' will be made nonzero by the first collision or wormhole traversal the ball encounters.

Now, follow the ball's initial trajectory assuming no collisions. In order for the trajectory to be dangerous, it must traverse the wormhole. The wormhole traversal will convert the trajectory's inclination from $z_1' = 0$ to $z_2' = \cos\theta\tan[2\arcsin(z_1/B)]$; cf. Fig. 15(a). Here θ is the angle at which the trajectory's equatorial projection intersects the equatorial normal to the wormhole mouth (as in Fig. 11 above). If it travels a subsequent distance $\Delta l = L_2$ parallel to the equatorial plane and then collides with itself (inconsistently), the height of its center at the collision will be $z_2 = z_1 + L_2\cos\theta\tan[2\arcsin(z_1/B)]$. To guarantee a collision, we must have $|z_2 - z_1| < 2R$. Thus, the initial trajectory will be *dangerous* only if

$$z_1 < B\sin[\tfrac{1}{2}\arctan(2R/L_2\cos\theta)] \ . \tag{5.1}$$

For typical dangerous initial trajectories, $L_2\cos\theta$ will be of order unity, and thus much larger than B, which in turn is a little larger than R; so the danger criterion (5.1) reduces to $z_1 \lesssim RB$. This means that the dangerous initial trajectories differ from coplanarity by no more than a fraction $B \ll 1$ of the ball's radius R.

We have not found a good way to analyze dangerous initial trajectories near the boundary of the region (5.1). However, for $z_1 \ll B\sin[\frac{1}{2}\arctan(2R/L_2\cos\theta)]$, the ball's motions parallel to the equatorial plane (its "in-plane motions") decouple from its motions perpendicular to the equatorial plane (its "out-of-plane motions"), and this

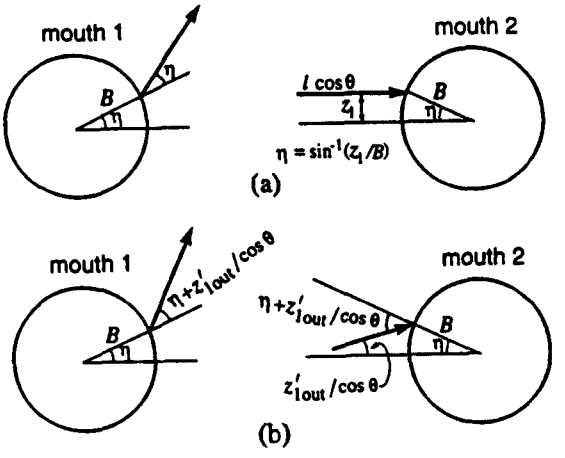

FIG. 15. Change in a noncoplanar trajectory's inclination z' when it traverses the wormhole from mouth 2 to mouth 1: (a) for a ball that does not collide before the traversal; (b) for a ball that collides and is vertically deflected before the traversal. (The change of inclination is a manifestation of the wormhole's "diverging-lens" effect.) The left and right halves of these two-dimensional diagrams are the projection of the ball's trajectory onto a plane that (i) is orthogonal to the equatorial plane (i.e., is vertical), and (ii) passes through the mouth's center and through the intersection of the trajectory with the mouth. The angle between the trajectory and this projection plane is θ, and correspondingly, horizontal distance along the projected trajectory is $l\cos\theta$.

permits us easily to extend to such trajectories most of the results of Secs. III and IV. We shall demonstrate this explicitly for self-consistent solutions that have just one wormhole traversal and one collision, and then shall argue that it is true also (though with a change in the allowed range of z_1) for all other self-consistent solutions.

Consider, then, a self-consistent solution in which the ball gets hit by itself, travels down mouth 2 and out of mouth 1, and then hits itself. We shall seek conditions on the degree of noncoplanarity that permit the in-plane motions to decouple from the out-of-plane motions.

Denote by z_1 and z_2 the out-of-plane displacements of the ball's younger and older incarnations at the moment of collision. Because the balls are round, the in-plane locations of the balls' centers are influenced by the out-of-plane displacements by amounts

$$\Delta l \sim R(1-\cos\psi) \simeq R\psi^2/2 \simeq \tfrac{1}{2}R[(z_2-z_1)/2R]^2 , \tag{5.2}$$

where ψ is the angle shown in Fig. 16. Similarly, if the ball's center passes through the wormhole mouths at a height $z_{\rm mouth}$, that height will influence the ball's in-plane motion in the same manner as would a decrease

$$\frac{\delta B}{B} \simeq -\frac{z_{\rm mouth}^2}{2B^2} \tag{5.3}$$

in the wormhole's radius. The back action of the out-of-plane motion on the in-plane motion will be negligible

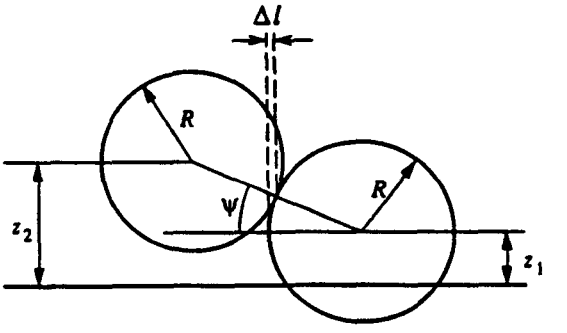

FIG. 16. Back action of a billiard ball's out-of plane motion on its in-plane motion.

in the collision and traversal if $\Delta l \ll R$ in (5.2) and $\delta B/B \ll 1$ in (5.3), i.e., if

$$|z_2 - z_1| \ll R \quad \text{and} \quad z_{\rm mouth} \ll B . \tag{5.4}$$

We now ask what values of z_1 lead to self-consistent solutions that satisfy this decoupling condition. [To keep formulas simple, we shall write them in approximate forms valid for the regime (5.4).]

In the collision, the z component of momentum transfer to ball 1 is

$$\Delta p_z = \frac{z_1 - z_2}{2R}\Delta p_l , \tag{5.5}$$

where $\Delta p_l = km v_1 \beta$ (with k typically of order unity) is the momentum transfer in the plane, m is the mass of the ball, v_1 is the ball's speed before the collision, and β is the deflection angle in the plane. This z-momentum transfer changes the inclination of the ball's trajectory from $z'_{\rm 1in} = 0$ to

$$z'_{\rm 1out} = \frac{z_1 - z_2}{2R}\frac{\Delta p_l}{p_l} = \frac{z_1 - z_2}{2R}k\beta \ll 1 , \tag{5.6}$$

where $p_l = mv_1$ is the momentum in the plane. After traveling a distance L_1 from the collision point, the ball arrives at mouth 2 with height

$$z_{\rm mouth} = z_1 + z'_{\rm 1out}L_1 \ll B . \tag{5.7}$$

The wormhole's diverging-lens effect causes the ball to emerge from its traversal with inclination [Fig. 15(b)]

$$z'_2 = z'_{\rm 1out} + \frac{2z_{\rm mouth}\cos\theta}{B} \ll 1 . \tag{5.8}$$

The height z_2 that the ball reaches after traveling through the wormhole and returning to the collision point is

$$z_2 = z_{\rm mouth} + z'_2 L_2 . \tag{5.9}$$

Combining Eqs. (5.6), (5.7), (5.8), and (5.9), we obtain

$$z_2 - z_1 = \frac{(2L_2\cos\theta/B)z_1}{1 + (k\beta/2R)(L_1 + L_2 + 2L_1L_2\cos\theta/B)} , \tag{5.10a}$$

and correspondingly

$$z_{\text{mouth}} = \frac{[1+(k\beta/2R)(L_1+L_2)]z_1}{1+(k\beta/2R)(L_1+L_2+2L_1L_2\cos\theta/B)} . \tag{5.10b}$$

Note that, whatever may be the values of the parameters L_1, L_2, θ, and β, there always is a height z_1 that makes $z_2 - z_1$ and z_{mouth} small enough to satisfy the decoupling criteria (5.4). For the typical case of $\phi - \theta \gg B$, the distances of the collision from the mouths are $L_1 \sim L_2 \sim 1$ and the in-plane deflection angle in the collision is $\beta \sim BR$ [Eq. (4.12a)], so

$$z_2 - z_1 \sim z_1/B \quad \text{and} \quad z_{\text{mouth}} \sim z_1 , \tag{5.11}$$

and both decoupling criteria (5.4) are satisfied if

$$z_1 \ll BR . \tag{5.12}$$

Unfortunately (and not surprisingly), this decoupled range is a small portion of the full range of dangerous initial trajectories $z_1 < B\sin[\frac{1}{2}\arctan(2R/L_2\cos\theta)] \sim RB$. Thus, we can say nothing about the existence of solutions over the full range. However, in the decoupled range we can infer the following from the above analysis. (i) The in-plane motion is affected negligibly by the out-of-plane motion. (ii) If there exists a solution to the equations of motion for the in-plane motion, then there is also a solution for the out-of-plane motion, and it is described by the above equations. (iii) The in-plane motion is described by the same equations as for coplanar initial trajectories. (iv) Therefore, *to each solution for any slightly noncoplanar initial trajectory there corresponds a solution for the corresponding coplanar trajectory, and conversely.* We have derived this conclusion only for the case of solutions with a single collision and single wormhole traversal. However, it should be clear that the same method can be used to derive the same final conclusion for all self-consistent nearly coplanar solutions, regardless of the number of collisions and traversals. There will be a change in the precise criteria for decoupling of the in-plane motions from the out-of-plane motions, but there will always be some out-of-plane neighborhood of coplanar initial trajectories for which the conclusion holds true.

This implies that the results of Secs III and IV for coplanar trajectories are also valid for slightly noncoplanar trajectories. Specifically: (i) When $R \ll B \ll 1$ all initial trajectories have multiplicities greater than zero (i.e., have self-consistent solutions), and all dangerous initial trajectories have infinite multiplicity. (ii) When B is allowed to be of order unity (but no larger than $\frac{1}{2}$), and R/B is constrained only to be small enough to neglect tidal forces, the extensive set of dangerous initial trajectories investigated in Sec. IV and Appendix B all have self-consistent solutions even when they are perturbed slightly in a noncoplanar way.

To recapitulate, these conclusions hold only for a neighborhood of coplanarity (typically $z_1 \ll BR$) that is much smaller than the full range of dangerous initial trajectories (typically $z_1 \lesssim BR$). However, these conclusions make us suspect that even when $z_1 \sim BR$, all initial trajectories will have at least one self-consistent solution.

VI. CONCLUSIONS

We have found that the Cauchy problem for a billiard ball in a wormhole spacetime with closed timelike curves is ill posed in the sense that large, generic classes of initial trajectories have multiple, and even infinite numbers of self-consistent solutions to the equations of motion. On the other hand, we have seen no evidence for a stronger type of ill posedness: generic initial trajectories with no self-consistent solutions. In paper II [9] it will be shown that a sum-over-histories version of quantum mechanics restores well posedness to the Cauchy problem: Quantum mechanics predicts definite probabilities for a nearly classical billiard ball to follow this, that, or another of its classical solutions.

These results give a first glimpse of the behavior of interacting systems in wormhole spacetimes with closed timelike curves. It will be interesting to study more realistic, albeit more complex, classical and quantum systems, as some researchers are currently doing [10]. However, our results suggest that in general there might be no deep conflict between the existence of closed timelike curves and the standard laws of physics.

ACKNOWLEDGMENTS

We thank Joseph Polchinski for motivating this research by asking, in a letter to one of us, how the laws of physics could deal with paradoxical situations of the sort embodied in Fig. 3(a). For helpful discussions we thank John Friedman, Mike Morris, Nicolas Papastamatiou, Leonard Parker, and Ulvi Yurtsever. This paper was supported in part by National Science Foundation Grant No. AST-8817792.

APPENDIX A: DERIVATION OF EQUATIONS FOR COPLANAR SELF-CONSISTENT SOLUTIONS

In this appendix we derive a complete set of equations that govern self-consistent, coplanar solutions with $B < \frac{1}{2}$, R/B small enough to neglect tidal forces, and a single collision that the ball first encounters before any wormhole traversals and encounters the second time after just one traversal. The bottom line of our derivation will be a proof that, to each nonspurious solution of Eqs. (4.2) and (4.3) there corresponds a solution of the complete equations of motion.

Our derivation involves the geometric parameters depicted in Fig. 17, which is a more detailed version of Fig. 11. The first phase of our derivation is to construct a full set of equations of motion. The equations in our full set will be numbered; other equations along the way will be unnumbered. The full set consists of (i) three "main equations," which can be thought of as coupled equations for three unknowns, α, β, and v_2, in terms of the wormhole and ball radii B, R and the parameters v_1, θ, ϕ of the ball's initial trajectory, and (ii) a set of auxiliary equations, which express various geometric parameters appearing in the main equations in terms of the

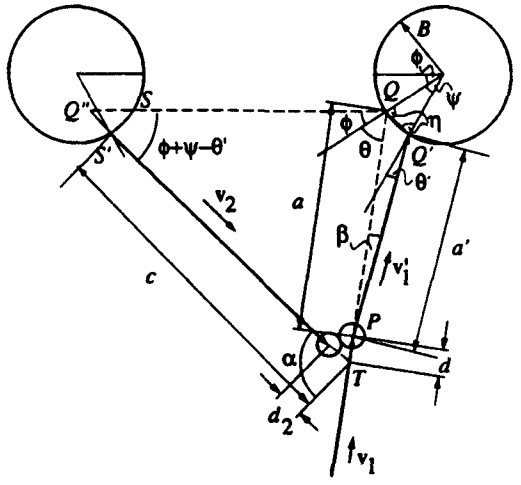

FIG. 17. Full geometry of a self-consistent solution with one wormhole traversal and one billiard-ball collision. This is the same as Fig. 11, but with many more details shown. By convention, all angles and distances (e.g., α, β, d, and d_2) are positive when their orientations are as shown here.

unknowns α, β, v_2 and the knowns B, R, v_1, θ, ϕ.

We begin by constructing the three main equations. They are based on and embody the laws of mirror exchange (which guarantee conservation of momentum and energy), the geometry of the balls relative to each other and relative to their trajectories at the moment of collision, and the demand that the ball return to the event of collision at the same external time T as it left it. (These are all the laws of motion except for the wormhole traversal rules and the law of straight-line motion between collisions and traversal; those remaining laws are embodied in the auxiliary equations.)

The laws of mirror exchange (2.4a) can be rewritten as

$$v_1' = v_2, \quad \mathbf{v}_1' \times (\mathbf{v}_1 + \mathbf{v}_2) = -\mathbf{v}_2 \times (\mathbf{v}_1 + \mathbf{v}_2) ,$$

$$v_2' = v_1, \quad \mathbf{v}_2' \times (\mathbf{v}_1 + \mathbf{v}_2) = -\mathbf{v}_1 \times (\mathbf{v}_1 + \mathbf{v}_2)$$

(together with the requirement that we reject the spurious solutions $\mathbf{v}_1' = -\mathbf{v}_2$, $\mathbf{v}_2' = -\mathbf{v}_1$). The first pair of these determine $\mathbf{v}_1'$ in terms of $\mathbf{v}_1$ and $\mathbf{v}_2$, and will be crucial to our analysis. The second pair determine $\mathbf{v}_2'$, which is of no interest, and thus we can and shall ignore them. The first relation $v_1' = v_2$ we shall automatically use throughout the analysis without even writing it down; i.e., nowhere will v_1' appear; we shall always write v_2 in its place. The second relation $\mathbf{v}_1' \times (\mathbf{v}_1 + \mathbf{v}_2) = -\mathbf{v}_2 \times (\mathbf{v}_1 + \mathbf{v}_2)$, which then becomes our sole embodiment of mirror exchange and hence of energy and momentum conservation, we rewrite in terms of the speeds and angles shown in Fig. 17:

$$v_2 \sin(\alpha - \beta) = v_1(\sin\alpha + \sin\beta) .$$

In order to free this equation from its spurious solution $\alpha - \beta = \pi$ (i.e., $\mathbf{v}_1' = -\mathbf{v}_2$), we divide both sides by $2\cos\frac{1}{2}(\alpha - \beta)$, thereby obtaining

$$v_2 \sin\tfrac{1}{2}(\alpha - \beta) = v_1 \sin\tfrac{1}{2}(\alpha + \beta) . \tag{A1}$$

This is our first main equation.

Turn, next, to the geometry of the collision. Letting the collision occur at time $T = 0$ and introducing a suitable origin of coordinates, we can write the incoming trajectories as

$$\mathbf{r}_1(T) = \mathbf{v}_1 T, \quad \mathbf{r}_2(T) = \mathbf{v}_2 T - 2sR\frac{\mathbf{v}_1 + \mathbf{v}_2}{|\mathbf{v}_1 + \mathbf{v}_2|} ;$$

cf. Eq. (2.4b). These two trajectories intersect spatially ($\mathbf{r}_1 = \mathbf{r}_2$) at times $T_1 = -d/v_1$ and $T_2 = d_2/v_2$, where d and d_2 are the distances shown in Fig. 17. By equating the above expressions for $\mathbf{r}_1(T_1)$ and $\mathbf{r}_2(T_2)$, we obtain

$$\frac{\mathbf{v}_2}{v_2} d_2 + \frac{\mathbf{v}_1}{v_1} d = 2sR\frac{\mathbf{v}_1 + \mathbf{v}_2}{|\mathbf{v}_1 + \mathbf{v}_2|} .$$

By forming the scalar products of this equation with $\mathbf{v}_1 - v_2^{-2}(\mathbf{v}_1 \cdot \mathbf{v}_2)\mathbf{v}_2$ (i.e., the component of $\mathbf{v}_1$ orthogonal to $\mathbf{v}_2$), and with $\mathbf{v}_2 - v_1^{-2}(\mathbf{v}_2 \cdot \mathbf{v}_1)\mathbf{v}_1$ (i.e., the component of $\mathbf{v}_2$ orthogonal to $\mathbf{v}_1$), we obtain several important relations: (i) our second main equation

$$|d|/v_1 = 2R/|\mathbf{v}_1 + \mathbf{v}_2|$$
$$= 2R/(v_1^2 + v_2^2 + 2v_1 v_2 \cos\alpha)^{1/2} ; \tag{A2}$$

(ii) the relation

$$d_2/v_2 = d/v_1 ,$$

which we shall use below to eliminate d_2 from our third main equation; and (iii) the signs of d and d_2

$$\text{sign}(d_2) = \text{sign}(d) = s .$$

[Recall that s was originally defined as the sign of $v_2 - v_1$; cf. Eq. (2.4b).] These signs are also the same as that of β,

$$\text{sign}(\beta) = \text{sign}(d) = s$$

[a relation embodied in the text's Eq. (4.6c)], as one can see from the following: The geometry of any collision dictates that the momentum transferred to ball 1 be along the line of centers from ball 2 to ball 1, i.e., $\mathbf{v}_1' - \mathbf{v}_1 \uparrow\uparrow \mathbf{r}_1 - \mathbf{r}_2$ (where $\uparrow\uparrow$ means "points in the same direction as"). Combining this with Eq. (2.4b), we see that $\mathbf{v}_1' - \mathbf{v}_1 \uparrow\uparrow s(\mathbf{v}_2 + \mathbf{v}_1)$. Taking the cross product with $\mathbf{v}_1$ we see that $\mathbf{v}_1' \times \mathbf{v}_1 \uparrow\uparrow s\mathbf{v}_2 \times \mathbf{v}_1$, which with the aid of Fig. 17 (and the fact that always $\sin\alpha > 0$) implies that $\sin\beta = s$.

Consider, next, the law that the total time lapse between the ball's first and second encounters with the collision must vanish. From Fig. 17, we see that the vanishing total time lapse is given by the time needed to travel the distances a' and $c - d_2$ both at speed v_2, *minus* the time delay $\Delta T = 1$ introduced by the wormhole traversal:

$$\frac{a'}{v_2} + \frac{c - d_2}{v_2} - 1 = 0 .$$

Using the preceding equation to eliminate d_2, we obtain

our third main equation:

$$v_2 = \frac{a' + c}{1 + d/v_1} . \tag{A3}$$

The auxiliary equations, which embody the laws of straight-line motion between collisions and wormhole traversal, and also embody the wormhole traversal rules, are

$$c = \frac{\sin(\theta+\phi)}{\sin\alpha}\left(1 - 2B\cos\phi + 2B\frac{\sin(\psi/2)\cos\gamma_1}{\sin\gamma_2}\right) - 2B\frac{\sin(\psi/2)\cos\gamma_3}{\sin\gamma_2} , \tag{A4}$$

$$d = -a + \frac{\sin\gamma_2}{\sin\alpha}\left(1 - 2B\cos\phi + 2B\frac{\sin(\psi/2)\cos\gamma_1}{\sin\gamma_2}\right) , \tag{A5}$$

$$a = \frac{B}{\sin\beta}[\sin(\theta-\beta) - \sin\theta'] , \tag{A6}$$

$$a' = a\frac{\cos[(\theta+\beta+\theta')/2]}{\cos[(\theta-\beta+\theta')/2]} , \tag{A7}$$

$$\psi = \theta - \beta - \theta' , \tag{A8}$$

$$\gamma_1 = \tfrac{1}{2}(\theta - 3\theta' - \beta) , \tag{A9}$$

$$\gamma_2 = \theta + \phi - 2\theta' - \beta , \tag{A10}$$

$$\gamma_3 = \tfrac{1}{2}(\theta - \theta' - \beta) + \phi , \tag{A11}$$

$$\theta' = \phi + \theta - \frac{\alpha+\beta}{2} , \tag{A12}$$

These auxiliary equations can be derived as follows:

It should be clear from Fig. 17 that $\overline{PQ} = a$ and $\overline{PQ'} = a'$, and that Q and Q' form an isosceles triangle with the center of the right-hand wormhole mouth. Hence, $\overline{QQ'} = 2B\sin(\psi/2)$ and $\eta = (\pi - \psi)/2$. The interior angles of the triangle PQQ' must add up to π:

$$\beta + (\pi - \eta - \theta) + (\pi - \eta + \theta') = \pi .$$

When η is reexpressed in terms of ψ, this immediately becomes Eq. (A8). Furthermore, applying the sine theorem to the triangle PQQ' yields (i) the relation

$$\frac{a}{\sin(\pi - \eta + \theta')} = \frac{a'}{\sin(\pi - \eta - \theta)} ,$$

which implies Eq. (A7); and (ii)

$$\frac{a}{\sin(\pi - \eta + \theta')} = \frac{2B\sin(\psi/2)}{\sin\beta} ,$$

which implies

$$2\sin[(\theta - \beta - \theta')/2]\cos[(\theta - \beta + \theta')/2] = \frac{a}{B}\sin\beta ,$$

which, by a well-known trigonometric formula, implies Eq. (A6).

Summing up the interior angles of the triangle TQQ'', we find

$$(\phi + \psi - \theta') + (\phi + \theta) + (\pi - \alpha) = \pi ,$$

which, when Eq. (A8) is used, yields Eq. (A12). Figure 18 expands on some details of Fig. 17. Applying the sine theorem to the triangle $Q''SS'$, we find

$$l_1 = 2B\sin(\psi/2)\frac{\sin(\eta + \theta')}{\sin(\phi + \psi - \theta')}$$

and

$$l_2 = 2B\sin(\psi/2)\frac{\sin(\eta - \phi)}{\sin(\phi + \psi - \theta')} .$$

For the triangle TQQ'' the sine theorem implies

$$c + l_2 = (1 - 2B\cos\phi + l_1)\frac{\sin(\phi+\theta)}{\sin(\pi - \alpha)}$$

and

$$a + d = (1 - 2B\cos\phi + l_1)\frac{\sin(\phi + \psi - \theta')}{\sin(\pi - \alpha)} ,$$

where we have used the relation $\overline{SQ} = 1 - 2B\cos\phi$. If, in the last two equations, we eliminate l_1, l_2, η, and ψ by using the relations found so far, we obtain Eqs. (A4) and (A5) with the auxiliary definitions (A6)–(A11). This completes our derivation of the auxiliary equations (A4)–(A12).

The next phase of our analysis is a derivation of the

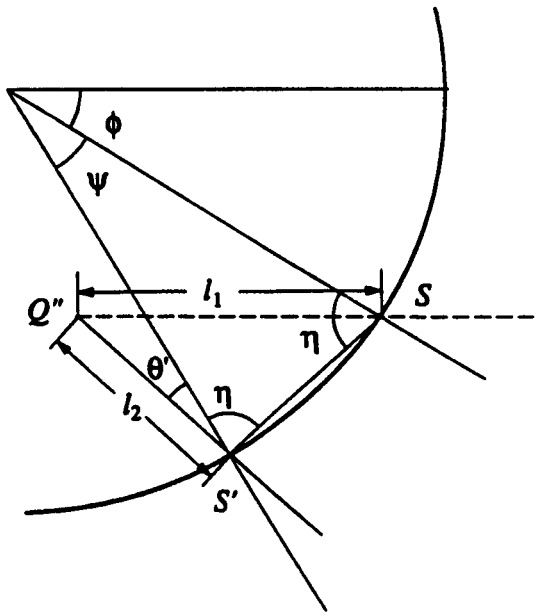

FIG. 18. Some details of Fig. 17 near the wormhole's left mouth (mouth 1).

text's equations (4.2) and (4.3) for the angles α and β. These coupled equations follow from our main and auxiliary equations in the following manner: First we define

$$\rho \equiv v_2/v_1 , \tag{A13}$$

and reexpress Eq. (A1) as

$$\rho = \frac{\sin[\frac{1}{2}(\alpha+\beta)]}{\sin[\frac{1}{2}(\alpha-\beta)]} . \tag{A14}$$

Now, using Eq. (A2) d can be expressed in terms of ρ and α as

$$d = 2sR/(1+\rho^2+2\rho\cos\alpha)^{1/2} , \tag{A15}$$

where $s = \mathrm{sign}(d)$. By combining Eqs. (A7), (A6), and (A12), it can be shown that

$$\begin{aligned} a'\sin\beta &= B[\sin\theta - \sin(\beta+\theta')] \\ &= B\left[\sin\theta - \sin\left(\theta+\phi-\frac{\alpha-\beta}{2}\right)\right] . \end{aligned} \tag{A16}$$

From Eqs. (A9)—(A11) it can be seen that $\gamma_2 = \gamma_1 + \gamma_3$, and from (A10) and (A12) that $\alpha = \theta + \phi + \gamma_2$. Using these in Eq. (A4), one can show that

$$\begin{aligned} c\sin\alpha &= \sin(\theta+\phi)(1-2B\cos\phi) \\ &\quad -2B\sin(\psi/2)\cos(\theta+\phi+\gamma_3) . \end{aligned} \tag{A17}$$

Next, using (A12) in (A8)–(A11), we obtain all the auxiliary angles in terms of α and β:

$$\psi = -\phi + \tfrac{1}{2}(\alpha-\beta), \quad \gamma_1 = -\theta - \tfrac{3}{2}\phi + \tfrac{3}{4}\alpha + \tfrac{1}{4}\beta , \tag{A18}$$

$$\gamma_2 = \alpha - \theta - \phi, \quad \gamma_3 = \tfrac{1}{2}\phi + \tfrac{1}{4}(\alpha-\beta) .$$

Using these expressions and some trigonometric manipulations, Eq. (A17) can be simplified further, giving

$$\begin{aligned} c\sin\alpha &= \sin(\theta+\phi) \\ &\quad -B\left[\sin\left(\theta+\phi+\frac{\alpha-\beta}{2}\right)+\sin\theta\right] . \end{aligned} \tag{A19}$$

Finally, eliminating v_2 between (A13) and (A3), and replacing ρ, a', and c from (A14), (A16), and (A19), we obtain the first of our equations for α and β: Eq. (4.2); and we obtain the second, Eq. (4.3) by eliminating a between (A5) and (A6), using the values (A18) and (A12) of the auxiliary angles, and performing some algebraic manipulations.

Notice that, in the process of deriving our two equations (4.2) and (4.3), we multiplied them by $\sin\alpha\sin\beta\sin[(\alpha-\beta)/2]$ [Eq. (4.2)], and by $\sin\alpha\sin\beta$ [Eq. (4.3)]. This introduced the first four spurious solutions of Eq. (4.6a). The fifth spurious solution in (4.6a) is the self-inconsistent solution. Since v_2 and v_1 are both positive by definition, $\rho \equiv v_2/v_1$ must also be positive, so any solution for α and β which produces a negative ρ via Eq. (A14), or equivalently via (4.4a), must be spurious. This accounts for Eq. (4.6b). Finally, as was discussed following Eq. (A2), the collision geometry rules out as spurious any solutions with $\mathrm{sign}(\beta) \neq \mathrm{sign}(d)$, which accounts for Eq. (4.6c).

The last phase of our analysis is to explain why, to every nonspurious solution of Eqs. (4.2) and (4.3) for α and β, there exists a full solution of the billiard ball's equations of motion. The reason is that (i) the main and auxiliary equations (A1)—(A12) embody all the equations of motion (as well as a lot of geometrical constructions); and (ii) by regarding the auxiliary equations (A4)—(A12) and the third main equation (A3) as definitions of other variables in terms of α, β, B, R, v_1, θ, ϕ, and by inserting a nonspurious solution of (4.2) and (4.3) into these equations, we automatically produce a solution of the remaining two main equations (A2) and (A1).

APPENDIX B: SELF-CONSISTENT SOLUTIONS FOR $B \ll 1$

In this appendix we derive the properties of self-consistent solutions quoted in Sec. IV C, for a wormhole and ball with $B \ll 1$ and $R/B < \frac{1}{2}$. We restrict attention to dangerous initial trajectories in the range (4.7) [interior of the dangerous triangle depicted in Fig. 12], and restrict our search to self-consistent solutions with a single collision of the type shown in Fig. 17 and with $|\beta| \ll 1$ and $|\epsilon| \ll 1$, where $\epsilon \equiv \alpha - 2\phi$; cf. Eqs. (4.9).

We begin our derivation in Appendix B 1 by expanding the highly nonlinear, coupled equations (4.2), (4.3) in powers of β and ϵ to the leading orders that produce nonspurious solutions. Then in Appendix B 2 we derive explicit solutions to those approximate equations for the central region of the dangerous triangle, and in Appendix B 3 for the upper-edge region of the triangle.

1. Approximate equations

In this section we derive the approximate equations for β and ϵ by power-series expansions of Eqs. (4.2) and (4.3). To facilitate the expansion of Eq. (4.2), we first divide it by $\sin(\alpha/2)$ (a factor that appears in each term in the limit of vanishing β). When we then expand, the resulting equations are homogeneous in β and ϵ and at linear order admit only spurious solutions, so we move on to quadratic order. Up through quadratic order the expanded equations take the forms

$$M\epsilon + N\epsilon^2 + P_1\beta + Q_1\beta^2 + S_1\beta\epsilon = 0 , \tag{B1}$$

$$M\epsilon + N\epsilon^2 + P_2\beta + Q_2\beta^2 + S_2\beta\epsilon = 0 , \tag{B2}$$

for which the coefficients M and N of ϵ and ϵ^2 are identically the same in the two equations. The expressions for all the expansion coefficients are

$$M = \tfrac{1}{2}B\sin 2\phi\cos\theta , \tag{B3}$$

$$N = \tfrac{1}{2}B(\cos 2\phi\cos\theta + \tfrac{1}{4}\sin 2\phi\sin\theta) , \tag{B4}$$

$$\begin{aligned} P_1 &= -\sin(\phi-\theta) - 2(4\lambda_1+s-2)R\sin\phi \\ &\quad + B\left[\tfrac{3}{4}\sin(2\phi-\theta) - \tfrac{1}{4}\sin(2\phi+\theta) - \sin\theta\right] , \end{aligned} \tag{B5}$$

$$Q_1 = -\cos\phi\cos\theta - \tfrac{1}{2}\cot\phi\sin(\phi+\theta) - 2(2\lambda_1-1)R\cos\phi + B[\tfrac{1}{2}(9\cos^2\phi-1)\cos\theta + \tfrac{1}{4}\sin\theta\cot\phi(7\cos^2\phi-3)] , \quad \text{(B6)}$$

$$S_1 = -\cos 2\phi\cos\theta/\cos\phi + R[2(2\lambda_1-1)/\cos\phi + (4-8\lambda_1-s)\cos\phi] + B[\cos\theta(\tfrac{3}{2}\cos^2\phi-1) + \tfrac{1}{4}\sin 2\phi\sin\theta] , \quad \text{(B7)}$$

$$P_2 = -\sin(\phi-\theta) + 2sR\sin\phi + B(-2\sin\theta\cos^2\phi + \tfrac{1}{2}\sin 2\phi\cos\theta) , \quad \text{(B8)}$$

$$Q_2 = -sR\cos\phi + B(\tfrac{1}{2}\cos\theta - \tfrac{3}{8}\sin 2\phi\sin\theta) , \quad \text{(B9)}$$

$$S_2 = -\cos(\phi-\theta) + sR\cos\phi + B(\cos\theta\cos^2\phi + \tfrac{5}{4}\sin\theta\sin 2\phi) . \quad \text{(B10)}$$

Here the notation is that of Sec. IV and Appendix A, including the use of λ_1 as a surrogate for the ball's initial speed v_1; cf. Eqs. (4.10) and (4.8) which imply

$$v_1 = \frac{1}{\cos\phi}[(1-2B\cos\phi)\cos\theta + 2R(2\lambda_1-1)] . \quad \text{(B11)}$$

By subtracting Eq. (B2) from Eq. (B1) and dividing by β, we obtain the linear equation

$$Q\beta + S\varepsilon + P = 0 , \quad \text{(B12)}$$

where

$$Q = -\cos\phi\cos\theta - \tfrac{1}{2}\cot\phi\sin(\phi+\theta) - (4\lambda_1 - s - 2)R\cos\phi + B(-\cos\theta + \tfrac{9}{2}\cos^2\phi\cos\theta + \cos^2\phi\cot\phi\sin\theta) , \quad \text{(B13)}$$

$$S = \cos\theta/\cos\phi - \cos(\phi+\theta) + R[2(1-2\lambda_1)\cos 2\phi/\cos\phi - 2s\cos\phi] + B(-\cos\theta + \tfrac{1}{2}\cos\theta\cos^2\phi - \sin 2\phi\sin\theta) , \quad \text{(B14)}$$

$$P = -4R\sin\phi(2\lambda_1 + s - 1) . \quad \text{(B15)}$$

We shall use Eqs. (B2) and (B12) as our approximate, coupled equations for β and ε. Since one is quadratic and the other is linear, they can be combined to form a single quadratic equation for β or for ε, but the coefficients in that quadratic equation are so complicated that we shall not write it down explicitly except in special regimes where the coefficients simplify.

The coefficients in our quadratic and linear equations (B2) and (B12) change drastically (because $R \ll 1$ and $B \ll 1$) as one approaches the edges of the dangerous triangle (Fig. 12), $\phi-\theta \to 0$, $\phi+\theta \to B$, $\phi \to \pi/2$. Correspondingly, the structures of the solutions change drastically as one approaches the edges. In Appendix B 2 we shall consider the central region (extending out to the right edge), and in Appendix B 3, the upper-left-edge region. Near the lower left edge and the left corner, ε grows large, invalidating the power-series expansion that underlies our quadratic and linear equations (B2) and (B12), and thus the methods of this appendix are not usable there.

2. Solutions in the central region

We specialize, now, to the central region of the dangerous triangle, $\phi-\theta \gg B$, $\phi+\theta-B \gg R$; and we retain our previous assumptions, $B \ll 1$, $R/B < \frac{1}{2}$. In one of our manipulations we shall require an additional constraint: $\varepsilon \ll \phi-\theta$. Since $\phi-\theta \gg B$ and ε has already been assumed small, this additional constraint is not severe.

These constraints on the parameters imply that in (B2) the terms in ε^2, β^2, and $\beta\varepsilon$ can be neglected compared to the first-order terms. The result is the linear relation

$$\beta = \frac{\sin 2\phi\cos\theta}{2\sin(\phi-\theta)}B\varepsilon \ll \varepsilon . \quad \text{(B16)}$$

Inserting this relation into our linear equation (B12), we find that ε is (very nearly) independent of B:

$$\varepsilon = \frac{8\cos\phi}{\sin(\theta+\phi)}(\lambda_1-\sigma)R , \quad \text{(B17)}$$

with

$$\sigma \equiv \tfrac{1}{2}(1-s) = \begin{cases} 0 & \text{if } s=+1 , \\ 1 & \text{if } s=-1 . \end{cases} \quad \text{(B18)}$$

Inserting this back into Eq. (B16), we obtain

$$\beta = \frac{4\sin 2\phi\cos\phi\cos\theta}{\sin(\phi-\theta)\sin(\phi+\theta)}(\lambda_1-\sigma)BR = \frac{8\sin\phi}{\cos\theta(\tan^2\phi-\tan^2\theta)}(\lambda_1-\sigma)BR , \quad \text{(B19)}$$

and by inserting these relations into Eqs. (A13), (A14), and (4.11), we obtain the dimensionless parameter λ_2 that describes the speed v_2 of the ball between its encounters with the collision

$$\lambda_2 - \sigma = \left[1 + \frac{\cos^3\phi\cos^2\theta}{2\sin(\phi-\theta)\sin(\phi+\theta)}B\right](\lambda_1-\sigma) = \left(1 + \frac{2\cos\phi}{\tan^2\phi-\tan^2\theta}B\right)(\lambda_1-\sigma) . \quad \text{(B20)}$$

Equations (B17)–(B20) are the simple form of the solutions for self-consistent collisions of class I ($s=+1$, $\sigma=0$) and class II ($s=-1$, $\sigma=1$), which we quoted and discussed in Sec. IV B [Eqs. (4.14) and (4.15)].

3. Solutions in the upper-edge region

We turn, finally, to the upper-left-edge region of the dangerous triangle, $0 \le \phi-\theta \lesssim B$; and in order to obtain valid solutions with $|\beta| \ll 1$ and $|\varepsilon| \ll 1$, we bound ourselves away from the triangle's left corner—i.e., we assume that $\phi \gg B$. In our formulas we shall characterize the difference $\phi-\theta$ by a dimensionless parameter

$$\mu \equiv (\phi-\theta)/B . \quad \text{(B21)}$$

As in the preceding subsection, our constraints on ϕ and θ make the ε^2 and β^2 terms in Eq. (B2) negligible compared to the first-order terms; but now the $\beta\varepsilon$ term is not *a priori* negligible. As a result, Eq. (B2) takes the form

$$k_1\beta + k_2\varepsilon + k_3\beta\varepsilon = 0 , \tag{B22}$$

where

$$k_1 = -\mu B + 2sR\sin\phi - B\sin\phi\cos^2\phi , \tag{B23}$$

$$k_2 = B\sin\phi\cos^2\phi , \tag{B24}$$

$$k_3 = -1 . \tag{B25}$$

Our other, linear, equation for ε and β [Eq. (B12)] also simplifies; its coefficients become

$$Q = -2\cos^2\phi , \tag{B26}$$

$$S = 2\sin^2\phi , \tag{B27}$$

$$P = -8R\sin\phi(\lambda_1 - \sigma) . \tag{B28}$$

By combining our two equations and eliminating ε, we obtain the following quadratic equation for β:

$$\beta^2 + p\beta + q = 0 , \tag{B29}$$

with

$$p = 2\tan^2\phi[2(\lambda_1 - \sigma) - s\sin\phi]R - (\sin\phi\cos 2\phi - \mu\tan^2\phi)B , \tag{B30}$$

$$q = -4BR\sin^2\phi(\lambda_1 - \sigma) . \tag{B31}$$

In discussing the solutions of this quadratic equation we shall restrict attention to the region $0 < \lambda_1 < 1$ of dangerous initial trajectories.

By examining the signs of the coefficients in Eq. (B29), it is easy to see that when $s = +1$ (class-I collision) there always exist two real solutions for β, one positive and thus acceptable; the other negative and thus spurious (recall that $\beta > 0$ for class I and $\beta < 0$ for class II; cf. Fig. 3). On the other hand, when $s = -1$ there is always a range of ϕ where $p^2/4 - q < 0$ and there is no solution. For $R \ll 1$ and $\mu \ll 1$, this no-solution region is $\phi \sim \pi/4$.

Focus attention on the always existent class-I solution, $s = +1$ (and $\sigma = 0$). Since $q < 0$ in this case, the solution is

$$\beta = -p/2 + \sqrt{p^2/4 - q} . \tag{B32}$$

When one continuously varies ϕ in the range of our analysis, $\phi \gg B$, p passes through 0 at some point and changes sign. Since q is second order in the small radii B and R, while p is first order, there is a sharp change in the form of the solution (B32) at that point:

$$\beta = \begin{cases} -q/p & \text{if } p \gg |q| , \\ -p & \text{if } p \ll -|q| . \end{cases} \tag{B33}$$

When $R\tan^2\phi \ll B$ and $\mu\tan^2\phi \ll 1$, the change of sign for p occurs very close to $\pi/4$, and the solution (B33) on the two sides of $\pi/4$ is

$$\beta = \sin\phi\cos 2\phi B, \quad \varepsilon = \frac{\cos 2\phi\cos^2\phi}{\sin\phi}B \quad \text{if } \phi - \pi/4 \ll -R\lambda_1 , \tag{B34}$$

and

$$\beta = \varepsilon = -\frac{4\sin\phi}{\cos 2\phi}R\lambda_1 \quad \text{if } \phi - \pi/4 \gg +R\lambda_1 . \tag{B35}$$

Notice that in (B34) β and ϕ are independent of λ_1, while in (B35) they are proportional to it. These are the solutions quoted in Eqs. (4.14) and (4.15).

[1] M.S. Morris, K.S. Thorne, and U. Yurtsever, Phys. Rev. Lett. 61, 1446 (1988).
[2] V.P. Frolov and I.D. Novikov, Phys. Rev. D 42, 1057 (1990); see also I.D. Novikov, Zh. Eksp. Teor. Fiz. 95, 769 (1989) [Sov. Phys. JETP 68, 439 (1989)].
[3] S.-W. Kim and K.S. Thorne, Phys. Rev. D 43, 3929 (1991).
[4] V.P. Frolov, Phys. Rev. D 43, 3878 (1991); U. Yurtsever, Class. Quantum Grav. 8, 1127 (1991).
[5] G. Klinkhammer, Phys. Rev. D 43, 2542 (1991); U. Yurtsever, Class. Quantum Grav. Lett. 7, L251 (1990); R.M. Wald and U. Yurtsever, Phys. Rev. D 44, 403 (1991).
[6] J. Friedman, M.S. Morris, I.D. Novikov, F. Echeverria, G. Klinkhammer, K.S. Thorne, and U. Yurtsever, Phys. Rev. D 42, 1915 (1990); cited in text as "the consortium."
[7] J. Friedman and M.S. Morris, Phys. Rev. Lett. 66, 401 (1991); and (in preparation).
[8] U. Yurtsever, J. Math. Phys. 31, 3064 (1990).
[9] G. Klinkhammer and K.S. Thorne (in preparation); cited in text as paper II.
[10] I.D. Novikov and V. Petrova (research in progress).
[11] I.D. Novikov (unpublished).
[12] R.L. Forward conceived this example for use in his forthcoming science fiction novel, Timemaster.
[13] M. Morris and K.S. Thorne, Am. J. Phys., 56, 395 (1988).